Inaugural Dissertation

for

obtaining the doctoral degree

of the

Combined Faculty of Mathematics, Engineering, and Natural Sciences

of the

Ruprecht – Karls – University

Heidelberg

Presented by

Antoni Andreu M. Martija, MSc

born in Batangas City, Philippines

Oral examination: 26 October 2022

The Multifunctional Protein EMP3 Facilitates the Activity of Multiple Oncogenic Receptors in Cellular Models of Isocitrate Dehydrogenase-Wild-Type Glioblastoma

Referees:

Prof. Dr. Peter Angel

Dr. Francesca Ciccolini

Declaration

I hereby declare that the submitted dissertation entitled “The Multifunctional Protein EMP3 Facilitates the Activity of Multiple Oncogenic Receptors in Cellular Models of Isocitrate Dehydrogenase-Wild-Type Glioblastoma” is the product of my own work and that all assistance received in preparing this thesis and manuscript have been acknowledged. I have not applied to be examined at any other institution, nor have I submitted this dissertation to any other faculty. Furthermore, I took reasonable care to ensure that the work is original, and, to the best of my knowledge, does not breach copyright law, and has not been taken from other sources except where such work has been cited and acknowledged within the text.

_____ _____

Place, Date Antoni Andreu M. Martija

Summary

Epithelial membrane protein 3 (EMP3) is a small, *N*-glycosylated tetraspanin that is highly expressed in isocitrate dehydrogenase-wild-type glioblastoma (IDH-wt GBM), a highly aggressive brain tumor characterized by extreme intratumoral heterogeneity. Specifically, it is highly expressed in astrocytic- and mesenchymal-like cells that predominantly compose the receptor tyrosine kinase II/classical (RTK II/CL) and mesenchymal (MES) IDH-wt GBM bulk tumor subtypes, respectively. EMP3 has been implicated in various biological processes and is proposed to facilitate tumor development in IDH-wt GBM. However, its exact molecular functions, and how these relate to IDH-wt GBM molecular heterogeneity, remain unclear. By integrating protein-protein interaction screens with transcriptomics, phosphoproteomics, and functional characterization of CRISPR/Cas9-edited EMP3 knockout (EMP3 KO) cells, this study defined the receptor trafficking and membrane organizing functions of EMP3 in IDH-wt GBM cellular models that approximate the RTK II/CL and MES subtypes, respectively.

To obtain initial insights on the subcellular context in which EMP3 could operate in, interactome mapping using BioID2-based proximity labeling coupled to mass spectrometry (MS) analysis was performed using RTK II/CL-like U-118 and MES-like LN-18 GBM cells. This approach identified several GBM-associated transmembrane receptors and trafficking regulators as novel, putative EMP3 interactors. Validation by co-immunoprecipitation and proximity ligation assays confirmed the RTK II/CL driver EGFR, the MES receptors CD44 and MET, the retromer components (TBC1D5, SNX1, and SNX2), the clathrin-coated vesicle protein CLINT1, and the EARP member VPS53 as *bona fide* EMP3 interacting partners. Furthermore, the analysis also identified potential cell type-specific and glycosylation-dependent interactors of EMP3. These included proteins involved in mitochondrial processes and nascent protein synthesis and transport in U-118 cells, as well as a Rho GTPase signaling subnetwork and mesenchymal RTKs in LN-18 cells.

Functional characterization of DK-MG and U-118 EMP3 KOs identified a novel EMP3-dependent mechanism by which EGFR activity could be sustained in these RTK II/CL-like cells. Loss of EMP3 enhanced epidermal growth factor (EGF)-induced EGFR degradation, an effect that correlated with increased EGFR trafficking to $RAB7^{+}$ late endosomes. The degradation phenotype was rescued by overexpression of the novel EMP3 interactor and RAB7 GTPase-activating protein TBC1D5 in a manner that is dependent on TBC1D5's catalytic

activity. Transcriptomic analysis further revealed dysregulation of DNA replication, cell cycle, and EGFR tyrosine kinase inhibitor resistance upon EMP3 depletion in these cell lines. Phosphoproteomic analysis of DK-MG and U-118 EMP3 KOs also indicated inhibition of downstream EGFR effector AKT1, as well as distal inhibition of cyclin-dependent kinases, most significantly CDK2. These signaling defects translated into cellular phenotypes, as EMP3 KO cells exhibited reduced cellular proliferation, blunted mitogenic response to the EGFR ligand EGF, and increased sensitivity to targeted EGFR inhibition by osimertinib. The positive correlation between EMP3 and EGFR was further reflected in clinical data from The Cancer Genome Atlas (TCGA), which indicated higher total and phosphorylated EGFR levels in GBMs with high EMP3 expression. Taken together, the findings imply that EMP3 may help maintain EGFR signaling in RTK II/CL tumors.

On the other hand, characterization of LN-18 EMP3 KOs revealed EMP3's potential role in maintaining CD44 and MET activity in MES-like cells. Specifically, loss of EMP3 impaired the transcription of genes that are dependent on CD44 and the Rho GTPase signaling effector and CD44 downstream target IQGAP1. EMP3-dependent activation of CD44/IQGAP1 signaling was further hypothesized to be mediated by PAK1, an EMP3 interactor that is known to also interact with and activate IQGAP1. Consistent with impaired CD44/IQGAP1 signaling, EMP3 KOs displayed reduced mitogenic response to the CD44 ligand hyaluronic acid (HA). At the same time, loss of EMP3 also abrogated the complex formation between the standard CD44 isoform, CD44s, and MET. This coincided with reduced MET membrane presentation as revealed by MS-based cell surface proteome analysis. Reduced EMP3-dependent CD44s-MET complex formation is presumed to cause MET signaling defects, as evidenced by the reduced transcription of genes regulated by the downstream MET effector ERK and impaired mitogenic response of EMP3 KOs to the MET ligand hepatocyte growth factor (HGF). Collectively, the findings indicate the EMP3 may organize the cytosolic and transmembrane interactions of CD44 and MET, and by doing so facilitate HA- and HGF-induced signaling.

In conclusion, this study identifies EMP3 to be a multifunctional protein with context-dependent and cell type-specific functions in IDH-wt GBM. In RTK II/CL-like DK-MG and U-118 cells, EMP3 facilitates EGFR signaling by restricting receptor degradation, while in MES-like LN-18 cells, EMP3 organizes signal transduction complexes required for CD44 and MET signaling. This dual trafficking and membrane organizing function highlights how moonlighting proteins like EMP3 could further contribute to the underlying subcellular

functional diversity of tumor cells in IDH-wt GBMs. Additionally, it exemplifies how a non-oncogene dependency may ultimately contribute to the maintenance of oncogenic signaling and development of therapeutic resistance. Altogether, these findings clarify the role of EMP3 in IDH-wt GBMs and provide the foundation for future mechanistic and therapeutic investigations into this protein.

Zusammenfassung

Das Epitheliale Membranprotein 3 (EMP3) ist ein kleines, N-glykosyliertes Tetraspanin, welches in Isocitrat-Dehydrogenase-Wildtyp Glioblastom (IDH-wt GBM), einem hochaggressiven und durch extreme intratumorale Heterogenität gekennzeichneten Gehirntumor, hoch exprimiert ist. Insbesondere wird es in astrozytären und mesenchymalen Zellen stark exprimiert, die die Subtypen der Rezeptor-Tyrosinkinase II/klassischen (RTK II/CL) bzw. mesenchymalen (MES) IDH-wt-GBM-Tumormasse bilden. EMP3 wird mit verschiedenen biologischen Prozessen in Verbindung gebracht und es wird angenommen, dass es die Tumorentwicklung bei IDH-wt-GBM fördert. Die genauen molekularen Funktionen von EMP3 und sein Zusammenhang mit der molekularen Heterogenität von IDH-wt-GBM bleiben jedoch unklar. Durch die Integration von Protein-Protein-Interaktions-Screens mit Transkriptomik, Phosphoproteomik und funktioneller Charakterisierung von CRISPR/Cas9-editierten EMP3-Knockout-Zellen (EMP3 KO) wurden in dieser Studie die Rezeptor-Sortierungs- und Membranorganisationsfunktionen von EMP3 in IDH-wt-GBM-Zellmodellen definiert, die in den RTK II/CL- bzw. MES-Subtypen entsprechen verwendet werden.

Um erste Einblicke in den subzellulären Kontext zu erhalten, in dem EMP3 wirken könnte, wurde ein Interaktom-Mapping mit BioID2-basierter Proximity-Markierung in Verbindung mit Massenspektrometrie (MS)-Analyse unter Verwendung von RTK II/CL-ähnlichen U-118 und MES-ähnlichen LN-18 GBM-Zellen durchgeführt. Dieser Ansatz identifizierte mehrere GBM-assoziierte Transmembranrezeptoren und Sortierungs-Regulatoren als neue, mutmaßliche EMP3-Interaktoren. Die Validierung durch Co-Immunopräzipitation und Proximity-Ligation Assays bestätigt den RTK II/CL-Treiber EGFR, die MES-Rezeptoren CD44 und MET, die Retromer-Komponenten (TBC1D5, SNX1 und SNX2), das in Clathrin-Vesikeln zu findende Protein CLINT1 und das EARP-Mitglied VPS53 als echte EMP3-Interaktionspartner. Darüber hinaus identifizierte die Analyse auch potenzielle zelltypspezifische und glykosylierungsabhängige Interaktoren von EMP3. Dazu gehörten Proteine, die an mitochondrialen Prozessen und an der Synthese und dem Transport naszierender Proteine in U-118-Zellen beteiligt sind, sowie ein Rho-GTPase-Signal-Subnetzwerk und mesenchymale RTKs in LN-18 Zellen.

Die funktionelle Charakterisierung von DK-MG und U-118 EMP3 KOs identifizierte einen neuartigen EMP3-abhängigen Mechanismus, durch den die EGFR-Aktivität in diesen RTK II/CL-ähnlichen Zellen aufrechterhalten werden kann. Der Verlust von EMP3 verstärkte den durch den epidermalen Wachstumsfaktor (EGF) induzierten EGFR-Abbau, ein Effekt, der mit einem erhöhten EGFR-Transport zu späten $RAB7^{+}$-Endosomen korrelierte. Der Degradationsphänotyp wurde durch Überexpression des neuen EMP3-Interaktors und RAB7-GTPase-aktivierenden Proteins TBC1D5 gerettet. Diese Rettung ist nur mit katalytisch aktivem TBC1D5 möglich. Transkriptomische Analysen ergaben außerdem eine Dysregulation der DNA-Replikation, des Zellzyklus und der EGFR-Tyrosinkinase-Inhibitorresistenz bei Deletion von EMP3 in diesen Zelllinien. Phosphoproteomische Analysen von DK-MG und U-118 EMP3 KOs zeigten auch eine Hemmung des nachgeschalteten EGFR-Effektors AKT1 sowie eine distale Hemmung von Cyclin-abhängigen Kinasen, vor allem CDK2. Diese Signaldefekte zeigten sich auch in zellulären Phänotypen, wie einer verringerte zelluläre Proliferation, eine abgeschwächte mitogenen Reaktion auf den EGFR-Liganden EGF und eine erhöhte Empfindlichkeit gegenüber einer gezielten EGFR-Inhibition durch Osimertinib in EMP3 KO Zellen. Die positive Korrelation zwischen EMP3 und EGFR spiegelt sich auch in klinischen Daten aus dem The Cancer Genome Atlas (TCGA) wider, die einen höheren Gesamt- und Phospho-EGFR-Werte in GBMs mit hoher EMP3-Expression zeigen. Zusammengefasst deuten die Ergebnisse darauf hin, dass EMP3 zur Aufrechterhaltung der EGFR-Signalübertragung in RTK-II/CL-Tumoren beiträgt.

Andererseits zeigte die Charakterisierung von LN-18 EMP3 KOs die potenzielle Rolle von EMP3 bei der Aufrechterhaltung der CD44- und MET-Aktivität in MES-ähnlichen Zellen. Insbesondere beeinträchtigte der Verlust von EMP3 die Transkription von Genen, die von CD44 und dem Rho-GTPase-Signaleffektor und CD44-Downstream-Target IQGAP1 abhängig sind. Es wurde angenommen, dass die EMP3-abhängige Aktivierung der CD44/IQGAP1-Signalübertragung durch PAK1 vermittelt wird, einem EMP3-Interaktor, von dem bekannt ist, dass er auch mit IQGAP1 interagiert und es aktiviert. Im Einklang mit der gestörten CD44/IQGAP1-Signalübertragung zeigten EMP3 KOs eine reduzierte mitogene Reaktion auf den CD44-Liganden Hyaluronsäure (HA). Gleichzeitig wurde durch den Verlust von EMP3 auch die Komplexbildung zwischen der Standard-CD44-Isoform, CD44s, und MET unterbunden. Dies ging mit einer verminderten MET-Membranpräsentation einher, wie eine MS-basierte Zelloberflächen-Proteomanalyse ergab. Es wird vermutet, dass eine reduzierte EMP3-abhängige CD44s-MET-Komplexbildung zu Defekten bei der MET-Signalübertragung

führt, was durch die reduzierte Transkription von Genen, die durch den nachgeschalteten MET-Effektor ERK reguliert werden, und die beeinträchtigte mitogene Reaktion von EMP3 KOs auf den MET-Liganden Hepatozyten-Wachstumsfaktor (HGF) belegt wird. Insgesamt deuten die Ergebnisse darauf hin, dass EMP3 die zytosolischen und transmembranen Interaktionen von CD44 und MET organisieren und dadurch die HA- und HGF-induzierte Signalübertragung ermöglicht.

Zusammenfassend lässt sich sagen, dass diese Studie EMP3 als multifunktionales Protein mit kontextabhängigen und zelltypspezifischen Funktionen in IDH-wt-GBM identifiziert. In RTK II/CL-ähnlichen DK-MG- und U-118-Zellen fördert EMP3 die EGFR-Signalübertragung, indem es den Rezeptorabbau einschränkt, während EMP3 in MES-ähnlichen LN-18-Zellen Signaltransduktionskomplexe organisiert, die für die CD44- und MET-Signalübertragung erforderlich sind. Diese doppelte Funktion in Transport und der Membranorganisation macht deutlich, wie "moonlighting"-Proteine wie EMP3 zu der zugrunde liegenden subzellulären Funktionsvielfalt von Tumorzellen in IDH-wt-GBMs beitragen könnten. Darüber hinaus wird deutlich, wie eine nicht-onkogene Abhängigkeit letztlich zur Aufrechterhaltung der onkogenen Signalübertragung und zur Entwicklung von Therapieresistenz beitragen kann. Diese Ergebnisse tragen zu der Klärung der Rolle von EMP3 in IDH-wt-GBMs bei und bilden die Grundlage für künftige mechanistische und therapeutische Untersuchungen dieses Proteins.

List of Abbreviations

Abbreviation	Definition
AC-like	Astrocytic-like
ALDH1	Aldehyde dehydrogenase 1
AP-MS	Affinity purification-mass spectrometry
ATP	Adenosine triphosphate
ATRX	Transcriptional regulator ATRX
BBB	Blood-brain barrier
BCA	Bicinchoninic assay
CCV	Clathrin-coated vesicles
CD44	CD44 antigen
CDS	Coding sequences
CHOP	CpG hypomethylator phenotype
CL	Classical
CLINT1	Clathrin interactor 1
CNS	Central nervous system
CNV	Copy number variation
CPTAC	Clinical Proteomic Tumor Analysis Consortium
CT	Cellular tumor
DEGs	Differentially expressed genes
DMEM	Dulbecco's Modified Eagle Medium
DMSO	Dimethyl sulfoxide
DTT	Dithiothreitol
EARP	Endosome-associated recycling protein
ECD	Extracellular domain
ECM	Extracellular matrix
EGF	Epidermal growth factor
EGFR	Epidermal growth factor receptor
EMP3	Epithelial membrane protein 3
EMT	Epithelial-to-mesenchymal transition
ER	Endoplasmic reticulum; estrogen receptor (in Section 5.2.2 only)
ERK	Extracellular signal-regulated kinase
ERM	Ezrin, radixin, moesin
ESCC	Esophageal squamous cell carcinoma
FACS	Fluorescence-activated cell sorting
FAK	Focal adhesion kinase
FBS	Fetal Bovine Serum
FCs	Fold changes
FDR	False discovery rate
G-CIMP	glioma CpG island methylator phenotype
GBC	Gallbladder cancer
GBM	Glioblastoma
gDNA	Genomic DNA
GO	Gene Ontology
GPM	Glycolytic/plurimetabolic

gRNA	Guide RNA
GS	Glycine-serine
GSEA	Gene set enrichment analysis
GW	Gateway
HA	Hyaluronic acid
HCC	Hepatocellular carcinoma
HGF	Hepatocyte growth factor
HPA	Human Protein Atlas
IC_{50}	Half-maximal inhibitory concentration
ICD	Intracellular domain
IDH	Isocitrate dehydrogenase
IDH-mut	Isocitrate dehydrogenase-mutant
IDH-wt	Isocitrate dehydrogenase-wild type
IF	Immunofluorescence
IGF2R	Cation-independent mannose-6-phosphate receptor
IPA	Ingenuity Pathway Analysis
IRES	Internal ribosome entry site
IT	Infiltrating tumor
Ivy GAP	Ivy Glioblastoma Atlas Project
kDa	Kilodalton
KEA	Kinase enrichment analysis
KEGG	Kyoto Encyclopedia of Genes and Genomes
KO	Knockout
LB	Luria-Bertani
LE	Leading edge
LFQ	Label-free quantification
LGG	Lower grade glioma
LMD	Laser microdissection
LRRC8A	Volume-regulated anion channel subunit
LTR	Long terminal repeat
MAPK	Mitogen-activated protein kinase
MES-like	Mesenchymal-like
Mes/MES	Mesenchymal
MET	Hepatocyte growth factor receptor
MMP-9	Matrix metalloproteinase 9
MR	Master regulator
mRNA	Messenger RNA
MS	Mass spectrometry
MTC	Mitochondrial
MuLv	Murine leukemia virus
MVP	Microvascular proliferation
N47	Asparagine 47
NES	Normalized enrichment scores
NEU	Neuronal
NF1	Neurofibromin 1
NK	Natural killer
NPC	Neural progenitor cell

NPC-like	Neural progenitor cell-like
NSC	Neural stem cell
NSCLC	Non-small cell lung cancer
NTD	N-terminal domain
OPC	Oligodendrocyte progenitor cell
OPC-like	Oligodendrocyte progenitor cell-like
OS	Overall survival
OST	Oligosaccharyltransferase
OXPHOS	Oxidative phosphorylation
p-AKT	Phosphorylated AKT
p-EGFR	Phosphorylated EGFR
p-ERK	Phosphorylated ERK
PA	Pilocytic astrocytoma
PAN	Pseudopalisading cells around necrosis
PBS	Phosphate-buffered saline
PCA	Principal component analysis
PDX	Patient-derived xenograft
PI3K	Phosphoinositide 3-kinase
PLA	Proximity ligation assay
PN	Proneural
PNZ	Perinecrotic zone
POI	Protein of interest
PPI	Protein-protein interaction
PPR	Proliferative/progenitor
PRC2	Polycomb repressive complex 2
Prolif	Proliferative
PTEN	Phosphatase and tensin homolog
PTM	Post-translational modification
PX	Phox homology
RE	Restriction enzyme
RLU	Relative luminescence units
RNA-Seq	RNA sequencing
ROCK1	Rho-associated protein kinase 1
ROCK2	Rho-associated protein kinase 2
RoKAI	Robust Inference of Kinase Activity
RPPA	Reverse phase protein array
RTK	Receptor tyrosine kinase
scDNAme	Single-cell DNA methylation
SCRIB	Scribble homolog
scRNA-seq	Single-cell RNA-sequencing
SDC	Sodium deoxycholate
SDM-PCR	Site-directed mutagenesis by inverse PCR
SDS-PAGE	Sodium dodecyl sulfate-polyacrylamide gel electrophoresis
SGZ	Subgranular zone
shRNA	short hairpin RNA
SLC	Solute carrier transporter
SNARE	Soluble N-ethylmaleimide-sensitive factor attachment protein

snRNA-seq	Single-nucleus RNA-sequencing
SNX1	Sorting nexin-1
SNX2	Sorting nexin-2
SOC	Standard-of-care
SRP	Signal recognition particle
STS	Staurosporine
SV40	Simian virus 40
SVZ	Subventricular zone
TAMs	Tumor-associated macrophages
TBC1D5	TBC1 domain family member 5
TBC1D5 RQ	TBC1D5 R169A/Q204A mutant
TBC1D5 WT	Wild-type TBC1D5
TBE	Tris-borate-EDTA
TBS-T	Tris-buffered saline and Tween 20
TCGA	The Cancer Genome Atlas
TEAB	Triethylammonium bicarbonate
TERT	Telomerase reverse transcriptase
TGF-β	Transforming growth factor beta
TGN	Trans-Golgi network
TME	Tumor microenvironment
TP53	Tumor protein 53
TRAIL	Tumor necrosis factor-related apoptosis-inducing ligand
tSNE	t-distributed stochastic neighbor embedding
UMAP	Uniform Manifold Approximation and Projection
uPA	Urokinase-type plasminogen activator
VPS53	Vacuolar protein sorting-associated protein 53 homolog
WASH	Wiskott-Aldrich Syndrome protein and scar homologue
WES	Whole-exome sequencing
WHO	World Health Organization
Y2H	Yeast-two-hybrid
ZFYVE9	Zinc finger FYVE domain-containing protein 9

List of Figures

List of Supplementary Figures

List of Tables

Table of Contents

1 Introduction

1.1 IDH-wild-type glioblastoma

Glioblastoma (GBM) is a highly aggressive primary central nervous system (CNS) tumor that arises from neuroglial progenitor cells that have acquired cancerous properties through *de novo* chromosomal alterations and/or mutations in key growth-promoting signaling pathways (1–3). It is the most prevalent type of primary malignant brain tumor, with an annual incidence of approximately 3.21 per 100,000 individuals (4). In the 2021 World Health Organization (WHO) classification of CNS tumors, GBMs formally fall under isocitrate dehydrogenase (IDH)-wild-type (IDH-wt) glioblastomas. This diagnosis is applied to WHO grade 4 diffusely infiltrating astrocytic tumors with microvascular proliferation or necrosis or any of these genetic alterations: telomerase reverse transcriptase (*TERT*) promoter mutation, epidermal growth factor receptor (*EGFR*) gene amplification, or chromosome 7 amplification with loss of chromosome 10 (5). Despite having the same WHO grade, IDH-wt GBMs are molecularly distinct from high-grade IDH-mutant (IDH-mut) astrocytomas (Table 1); the latter group is uniquely defined by mutations in *IDH1/2*, tumor protein p53 (*TP53*), transcriptional regulator ATRX (*ATRX*), with or without homozygous deletion of *CDKN2A/B* (5). In addition to areas of pseudopalisading necrosis and aberrant angiogenesis, IDH-wt GBMs also characteristically exhibit high mitotic indices and nuclear atypia (3). These tumors have also been historically described as “multiforme”, owing to the high pleomorphism of tumor cells observed by early pathologists (6).

Table 1. Key differences between IDH-mutant and IDH-wild-type astrocytic gliomas

2021 WHO Classification	Astrocytoma, IDH-mutant	Glioblastoma, IDH-wild-type
IDH1/2 mutation	Present	Absent
Additional alterations	*TP53* *ATRX* +/- *CDKN2A/B* deletion	*EGFR* amplification Chr. 7 gain with Chr. 10 loss *TERT* promoter mutation
Subclasses	Astrocytoma or Astrocytoma, high-grade	RTK I, RTK II, RTK III, MES, MID, MYCN, G34
Necrosis and Microvascular proliferation	Presence indicates grade 4	Presence even without molecular alterations provides GBM diagnosis
Treatment after maximal surgical resection	Radiotherapy and/or TMZ	Radiotherapy and/or TMZ

IDH-wt GBM primarily affects the elderly, with patients having a median age of 65 at the time of diagnosis (4). GBMs are notorious for having very dismal prognosis and poor response to the standard of care (SOC), which currently consists of surgery and chemoradiotherapy (3,7,8). Several factors account for this, including the advanced age of most patients upon diagnosis, the impossibility of doing a complete surgical resection, the relative inaccessibility of the brain to most systematically administered drugs due to the blood-brain barrier (BBB), and the unique biological properties of the tumor itself (3,7,8). IDH-wt GBMs, as will be discussed in further detail below, exhibit high intratumoral heterogeneity (6,9,10). Due to the co-existence of multiple cellular states that are dependent on redundant growth-promoting pathways, targeted monotherapies often fail to kill all cells within a single tumor mass, and tumor recurrence inevitably occurs. Moreover, due to the highly immunosuppressive tumor microenvironment (TME) in GBM, it has been challenging to elicit potent immunological responses via novel immunotherapies in the clinics. Thus, the median survival time for patients treated with the SOC remains to be between 14-16 months (11,12), and the overall five-year survival rate remains low at 6.8% (4).

1.2 Cellular origin and developmental history of IDH-wt GBM

The hierarchical model for IDH-wt GBM evolution posits that these tumors arise from and are maintained by a pool of self-renewing and multipotent neural stem cells (NSC) or lineage-restricted progenitor cells that have acquired tumor-initiating capacity due to oncogenic mutations or chromosomal alterations (6). A defining feature of this model is the presumed existence of a cell-of-origin that is necessary and sufficient to give rise to GBMs. In the adult human brain, these cells are hypothesized to originate from either the subventricular zone (SVZ) of the lateral ventricles or the subgranular zone (SGZ) of the hippocampal dentate gyrus (13,14). Experimental models have demonstrated the possibility of generating GBMs from various lineages of tumor-initiating cells arising from the SVZs (Fig. 1) (13–17). Conditional deletion of the GBM-associated tumor suppressors neurofibromin 1 (*Nf1*), *Tp53,* and phosphatase and tensin homolog (*Pten*) in Nestin-positive NSCs located in the SVZ has been shown to be sufficient to generate GBMs in adult mutant mice (17). Similarly, a later study also demonstrated that GBM tumors can be generated *in vivo* by introducing *Tp53, Pten*, and *Egfr* mutations in murine SVZ NSCs (14). Interestingly, progenitor cells that sit below the level of NSCs in the differentiation hierarchy have also been shown to be capable of generating GBM *in vivo*. For example, targeted introduction of *Nf1, Tp53,* and/or *Pten* mutations in

bipotential progenitors—which comprise of neural progenitor cells (NPC) and oligodendrocyte progenitor cells (OPC)—also gave rise to GBM *in vivo* (15). Interestingly, the type of GBM differed based on the presence of the *Pten* mutation: triple-mutated progenitors gave rise to highly infiltrative tumors with astrocytic signatures (Type 1), while doubly-mutated progenitors gave rise to circumscribed tumors with oligodendrocytic features (Type 2) (15). Introduction of the same mutations in adult, lineage-restricted OPCs was also sufficient to generate Type 2-like tumors *in vivo* (15). However, the presence of the same mutations in Dlx-positive late-stage neuronal progenitors, Neurod1-positive immature neurons, and CamK2a-positive mature neurons failed to induce GBM formation *in vivo* (16). Collectively, these studies indicate that stem or progenitor cells are the likely cell-of-origin in GBM. Indeed, RNA velocity measurements measuring transcriptional dynamics in GBM samples indicate that rapidly cycling progenitor cells sit at the apex of the differentiation hierarchy and are likely the origin of all terminally differentiated cell types found in IDH-wt GBM (18).

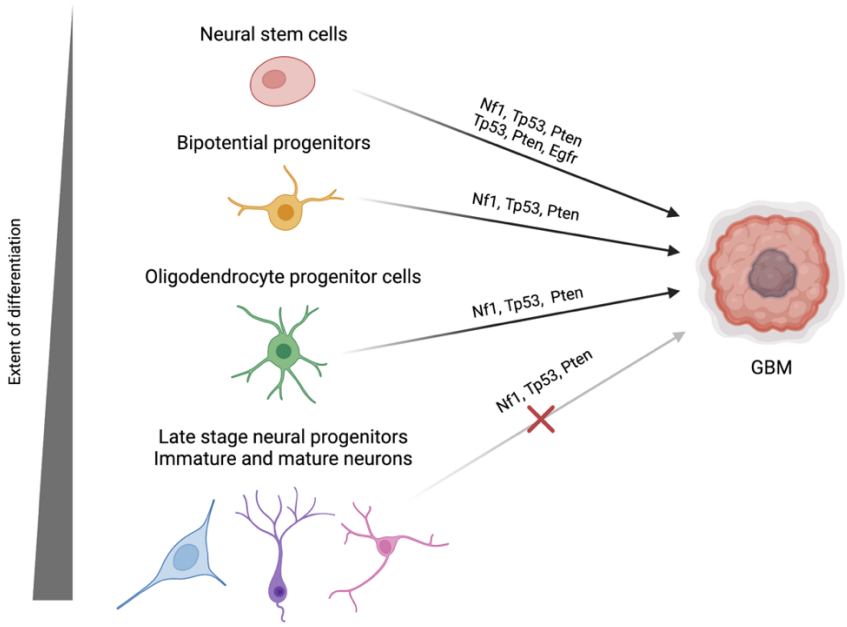

Figure 1. Summary of studies investigating the cell-of-origin of GBMs. Introduction of typical GBM mutations (e.g. *Nf1, Tp53, Pten, Egfr*) in various combinations into different progenitor/neuronal cell populations *in vivo* have shown that neural stem cells, bipotential progenitors, and oligodendrocyte progenitor cells—but not late-stage neuronal progenitors and neurons—can give rise to GBMs. Figure adapted from a review paper by Llaguno et al. (13) and was created using BioRender.com.

Recent studies, however, are also beginning to challenge the unidirectional mode of differentiation from a uniform population of stem or progenitor cells to more differentiated tumor cells. For one, GBM cells that are negative for stem cell markers have been shown to be capable of generating tumors mimicking actual GBMs (19–21). Multicolor fluorescence-

activated cell sorting (FACS) of distinct cell types from GBM spheroids followed by phenotypic profiling also show that all singly isolated subpopulations, regardless of their initial stem cell marker expression, can give rise to all other subpopulations present in the initial spheroid (22). Further mathematical modelling of the cell state transitions observed indicates that every initial cell subpopulation can directly transition towards other states, without going through intermediate cell states (22). Importantly, these transitions were determined to be reversible and responsive to environmental cues (22). Intriguingly, cells exhibiting higher plasticity led to faster generation of tumors *in vivo*, indicating that quick adaptive responses may be linked to tumorigenic potential (22). More sophisticated single-cell and lineage tracing experiments also demonstrate that GBM cells within a single tumor, which segregate across multiple transcriptomic states, can give rise to or interconvert into one another (Fig. 2) (10). Evolutionary analysis of these transcriptomic states indicate that no single state could be designated as a *bona fide* progenitor state (10). A significant proportion of the cells were also found to be in hybrid states, supporting the potential ability of GBM cells to undergo cell state transitions (10). Confirming this, implantation of barcoded tumor cells from a single cellular state yielded patient-derived xenografts (PDX) that eventually contained multiple cellular states (10). In summary, the emerging concept of plasticity maintains that stem/progenitor cells in GBM is not a singular clonal entity but is rather a reversible phenotypic state that can continuously emerge from non-hierarchical cell state transitions (6).

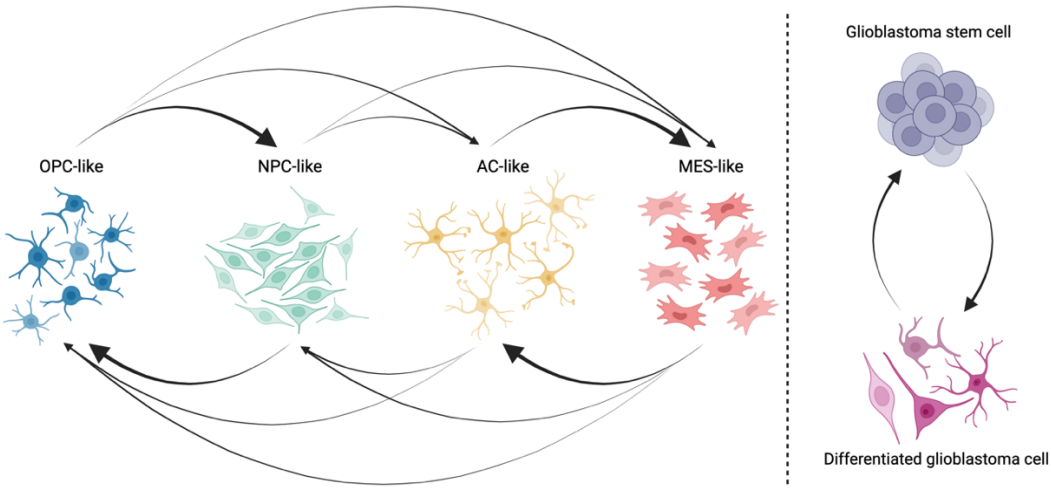

Figure 2. Cell state plasticity in GBM. GBM cells are proposed to exist within a spectrum of cellular states mimicking cells in the human brain (left). Tumor cells may assume any of these states in a reversible and interconvertible manner. GBM cells are also proposed to have the ability to shift from stem cell-like to differentiated-like states and vice versa (right). Figure adapted from a 2021 review by Yabo et al. (6). OPC – oligodendrocyte progenitor cell; NPC – neural progenitor cell; AC – astrocytic; MES – mesenchymal. Figure was created using BioRender.com.

Apart from the cell-of-origin and characteristic plasticity of GBM cells, another question that is of great interest to the field are the mutations that initiate GBM. Phylogenetic inference of the evolutionary trajectories of 21 IDH-wt GBM tumor samples has shown that copy number variations (CNVs) in chromosomes 7, 9, or 10 are the most likely tumor-initiating events (23). These CNVs correspond to the following gene dosage changes: amplification of *EGFR* in chromosome 7, loss of *CDKN2A/B* in chromosome 9, and loss of *PTEN* in chromosome 10 (23). In contrast, *TERT* promoter mutations, which are also very frequent in IDH-wt GBM and are a pre-requisite for rapid tumor growth, only arise later during tumor development (23). Coding mutations in *PTEN*, *TP53,* and *EGFR* were also observed to be frequent in primary tumors; however, these were found in a subset of samples only and were therefore unlikely to be the main tumor-initiating events (23). In contrast, deep whole-exome sequencing (WES) of matched tissues from IDH-wt GBM patients have shown that only *TERT* promoter mutations were consistently shared between tumor-free SVZ and matched tumor samples (14). Assuming that IDH-wt GBM arises from mutated NSCs in the SVZ, the proponents of the study concluded that *TERT* promoter mutations may be the earliest event in GBM pathogenesis (14). Regardless of these discrepancies, it is apparent that both chromosomal changes and *TERT* promoter mutations are very early events in GBM development. Indeed, these genetic alterations are now considered to be defining hallmarks of GBM. Other modes of -omics profiling, however, have also begun to shed light on other molecular features of IDH-wt GBM.

1.3 Molecular features of IDH-wt glioblastoma

1.3.1 Molecular classification of IDH-wt glioblastoma

GBMs have been historically classified into various subgroups based on genetic, epigenetic, transcriptomic, proteomic, and metabolomic features. The earliest profiling studies, which did not distinguish IDH-mut from IDH-wt tumors, were largely based on gene expression signatures (24,25). Applying clustering analysis on microarray data derived from a cohort of 76 tumor samples, Philipps et al. classified WHO grade 3 and grade 4 GBMs into three subtypes: proneural (PN), proliferative (Prolif), and mesenchymal (Mes) (24). PN tumors were enriched for grade 3 tumors and were associated with younger age and better prognosis (24). In contrast, Prolif and Mes GBMs were mostly grade 4 tumors and were associated with advanced age and poorer prognosis (24). In terms of gene expression, PN tumors highly expressed markers of developing neurons and were more similar to normal fetal and adult brain tissue, while Prolif and Mes tumors had high levels of neural stem cell markers (24).

Additionally, Mes tumors exhibited a gene signature indicative of multipotency, as it was comparable to gene expression programs found in various non-neuronal tissues including bone, synovium, smooth muscle, endothelial, and dendritic cells. Both Prolif and Mes tumors were also more enriched for *PTEN* loss and gain of *EGFR*, which are now understood to result from chromosomal alterations that are specific to IDH-wt tumors (5).

Similarly, a landmark study by the The Cancer Genome Atlas (TCGA) network has leveraged the transcriptomes of 206 patient samples to define four GBM subtypes: classical (CL), mesenchymal (MES), proneural (PN), and neural (25). The neural subtype was subsequently discarded in a later study, as it represented contamination of normal neural tissue in patient samples (26). Until now, the three remaining subtypes are widely used to describe the molecular features of bulk tumor samples (Fig. 3). The CL subtype represents tumors with chromosome 7 amplification, chromosome 10 loss, and high-level *EGFR* amplification. Focal homozygous deletion of *CDKN2A* was also observed to be frequent in this subtype, while mutations in other GBM-associated genes are conspicuously absent (25). On the other hand, MES GBMs often contain focal hemizygous deletions of the NF1 gene at chromosome 17 (25). There is also high expression of mesenchymal (*MET, CHI3L1, YKL40*, *CD44, MERTK*) and inflammatory markers (*TRADD, RELB, TNFRSF1A*) in MES tumors (25). Additionally, these tumors also harbor a more significant immune fraction relative to other subtypes, as indicated by increased expression of macrophage and microglial markers (26). Lastly, the PN subtype is marked by focal amplification of the platelet-derived growth factor receptor A (*PDGFRA*) locus, as well as high expression of oligodendrocytic and proneural genes (*NKX2-2, OLIG2, SOX* genes*, DCX, DLL3, ASCL1, TCF4*) (25). Because the original analysis also did not distinguish tumors based on IDH status, IDH-mutant tumors were also found to be overrepresented in this subtype (25).

GBM classification based on proteomic data have also grouped GBMs into subtypes that recapitulate previous transcriptomic groupings, despite known discordances between protein and messenger RNA (mRNA) expression levels (27,28). Performing targeted proteomic analysis of 27 glioma samples, Brennan et al. identified three proteomic classes of GBM (Fig. 3). These classes correlated well with known genomic alterations and were specifically defined by 1) EGFR activation, 2) PDGFR activation and 3) NF1 loss (27). The EGFR class, which was predictably associated with amplification and mutation of *EGFR*, displayed activation of the Notch pathway, as shown by high levels of Notch ligands, cleaved Notch receptor, and the

Notch target gene *HES1* (27). The PDGF class had high levels of PDGFB, phosphorylated PDGFRβ, and phosphorylated NFKB1 (27). There were also increased levels of PTEN and phosphorylation of MEK and extracellular signal-regulated kinase (ERK) in this class, indicating increased activation of the RAS pathway (27). Lastly, the NF1 class was defined by high expression of the four proteins (IRS1, IGFBP5, YKL40, and VEGF) and were enriched for tumors with chromosome 7 gain without focal amplification of either *EGFR* or hepatocyte growth factor receptor (*MET*) (27). This group also expectedly showed low levels of NF1, while also displaying lower levels of mitogen-activated protein kinase (MAPK) and phosphoinositide 3-kinase (PI3K) activation relative to the other two subclasses.

More recently, the Clinical Proteomic Tumor Analysis Consortium (CPTAC) performed proteogenomic profiling of 99 treatment-naive IDH-mut and IDH-wt GBMs based on CNVs, bulk RNA, protein, and phosphoprotein levels. Their clustering analysis yielded three groups of IDH-wt GBM tumors (Fig. 3), namely nmf1 (proneural-like), nmf2 (mesenchymal-like), and nmf3 (classical-like) GBMs (28). Integrated pathway analysis based on transcriptomic, proteomic, and phosphoproteomic data further revealed that the nmf1/proneural-like cluster highly expressed genes involved in neuronal processes like neurotransmitter transport and synaptic vesicle cycle (28). These tumors, along with the IDH-mut group, expectedly showed high levels of PDGFRA at the RNA, protein, and phosphoprotein levels (28). On the other hand, nmf2/mesenchymal-like tumors were enriched for *NF1* loss and exhibited high expression of genes involved in innate immune response, phagocytosis, and extracellular matrix (ECM) organization (28). These tumors also upregulated the mesenchymal markers *MET* and *CHI3L1*, as well as genes involved in hypoxic response, angiogenesis, macrophage polarization, and epithelial-to-mesenchymal transition (EMT) (28). Lastly, the nmf3/classical-like cluster highly expressed genes involved in mRNA splicing and mRNA metabolism and were enriched for *EGFR* amplification events (28).

Apart from transcriptomics and proteomics, DNA methylation has also been widely used and clinically applied as method to identify GBM subtypes (29,30). By profiling genome-wide DNA methylation patterns across 136 adult and pediatric cases of IDH-mut and IDH-wt GBMs, Sturm et al. defined six methylation subclasses: IDH, K27, G34, receptor tyrosine kinase (RTK) I (PDGFRA), RTK II (Classic), and Mesenchymal (MES) tumors (29). The IDH subclass was enriched for *IDH1* and *TP53* mutations and consistent with the glioma CpG island methylator phenotype (G-CIMP), exhibited global hypermethylation (29). Likewise, *TP53*

mutations were enriched in the K27 and G34 subclasses, which were named due to the characteristic K27 and G34 somatic mutations in *H3F3A* in these tumors (29). These two *H3F3A*-mutant subclasses did not harbor any *IDH1* mutations and were mostly found in pediatric and young adult patients, respectively (29). Since then, K27 subclass has been subsumed into a different tumor entity and is not currently included in the official WHO list of GBM subclasses (5,31). On the other hand, the G34 subclass—which is still a GBM subclass at present (5,31) —uniquely exhibited widespread hypomethylation in non-promoter regions, consistent with a CpG hypomethylator phenotype (CHOP) (29). The remaining IDH-wt subclasses partly recapitulated the TCGA subtypes, with RTK I tumors showing frequent *PDGFRA* amplification and enrichment for the TCGA PN signature; RTK II tumors exhibiting the TCGA CL signature along with the high frequency of "classical" chromosomal alterations in chromosomes 7 and 10 as well as homozygous deletion of *CDKN2A* and *EGFR* amplification; and MES tumors being enriched for the TCGA MES genes with fewer CNVs and point mutations relative to the other subtypes (29). Further epigenomic profiling have also identified master regulators critical for maintaining the identity of the IDH and the three major IDH-wt methylation subclasses (32) (Table 2). These classifications have been further refined and are now being integrated into routine molecular and histopathological diagnosis as per WHO recommendations (5,31).

Table 2. Subtype-specific master regulators of the major Sturm methylation subclasses

Methylation Subclass	Master Regulator
IDH	KLF13, MEF2D, MYCN, NR2E3, ONECUT1, PKNOX2, SOX14, TCF4, TCF7L2
RTK I	LHX2, NFIL3, SOX10, SOX4
RTK II	FOXO1, GLI2, HES1, HIF1A, NR3C1, SOX2, SOX9, TEAD1, TFCP2L1, ZBTB7C
MES	CEBPA, EGR2, FLI1, FOXD2, IRF2, IRF8, JUN, KLF3, KLF4, MAFB, MITF, NR4A2, RXRA, SREBF1, STAT3

Various other methylation-based classifiers have been further developed, albeit with relatively limited clinical utility. Using a cohort of 516 lower grade glioma (LGG) and GBM patients, the TCGA network have defined 7 methylation subgroups of GBM that broadly clustered into two macro-groups based on *IDH* status (33). The IDH-wt umbrella consisted of LGm4 (Classic-like), LGm5 (Mesenchymal-like), and LGm6 subgroups (33). The first two were expectedly enriched for RTK II/CL and MES tumors based on the TCGA and Sturm subtypes, respectively (33). Meanwhile, LGm6 included a bigger proportion of LGGs, had fewer alterations in chromosomes 7 and 10, and had relatively longer survival outcomes compared to

the LGm4 and LGm5 groups. Interestingly, these tumors also shared molecular features with pilocytic astrocytomas (PAs) (33). In fact, a PA-like subgroup exhibiting low mutational frequencies in typical GBM-altered genes and higher mutational burden in PA-associated genes was further described under LGm6 (33). However, a later analysis of the LGm6 group revealed that this classification might not be specific to tumors and might just reflect stromal contamination, as the LGm6 methylation signature correlated highly with non-malignant glial and immune cells gene signatures (34) Similarly, an independent genome-wide DNA methylation analysis performed on CPTAC samples identified six DNA methylation groups, aptly labeled dm1 to dm6 (28). The first three groups were enriched for the PN/nmf1, CL/nmf3, and MES/nmf2 subtypes, respectively (28). Interestingly, dm2 also displayed a G-CIMP phenotype secondary to increased expression of *de novo* DNA methylases, despite being IDH-wt (28). Methylation group dm4 showed co-enrichment of the newly defined nmf1 and nmf3 multi-omics subtypes, while dm5 equally consisted of nmf1 and nmf2 tumors (28). Lastly, methylation group dm6 exclusively consisted of G-CIMP IDH-mut tumors with increased expression of genes involved in chromatin organization (28).

Lastly, pathway-based bulk tumor classification of GBMs have also been established based on single-cell gene expression data (35). With this approach, four functionally and metabolically distinct GBM subgroups have been identified: glycolytic/plurimetabolic (GPM), mitochondrial (MTC), neuronal (NEU), proliferative/progenitor (PPR) (35). GPM tumors were defined by simultaneous activation of multiple metabolic processes, except for mitochondrial/oxidative phosphorylation (OXPHOS) activities (35). These tumors were also enriched for *MDM4* amplification and deletions or mutations in *NF1, PTEN,* and *RB1* (35). In contrast, MTC tumors relied selectively on mitochondrial/OXPHOS processes, as well as fatty acid oxidation (35). Supporting its unique reliance on mitochondrial processes, these tumors were also selectively vulnerable to OXPHOS inhibition and reactive oxygen species (ROS) (35). Genetically, MTC tumors exclusively displayed *NRAS* mutations, and more frequent amplifications of *CDK4, EGFR,* and *MDM2* (35). On the other hand, NEU tumors were uniquely defined by activation of various neuronal processes, including axon formation and synaptic transmission (35). These tumors were mostly associated with *ATRX* and *TET1* mutations (35). Lastly, PPR tumors showed activation of cell cycle progression, mitosis, DNA replication, and DNA damage repair pathways (35). These tumors also displayed frequent amplifications in *PDGFRA* and *EZH2* and had *EGFR* amplification and mutation events comparable to MTC tumors (35).

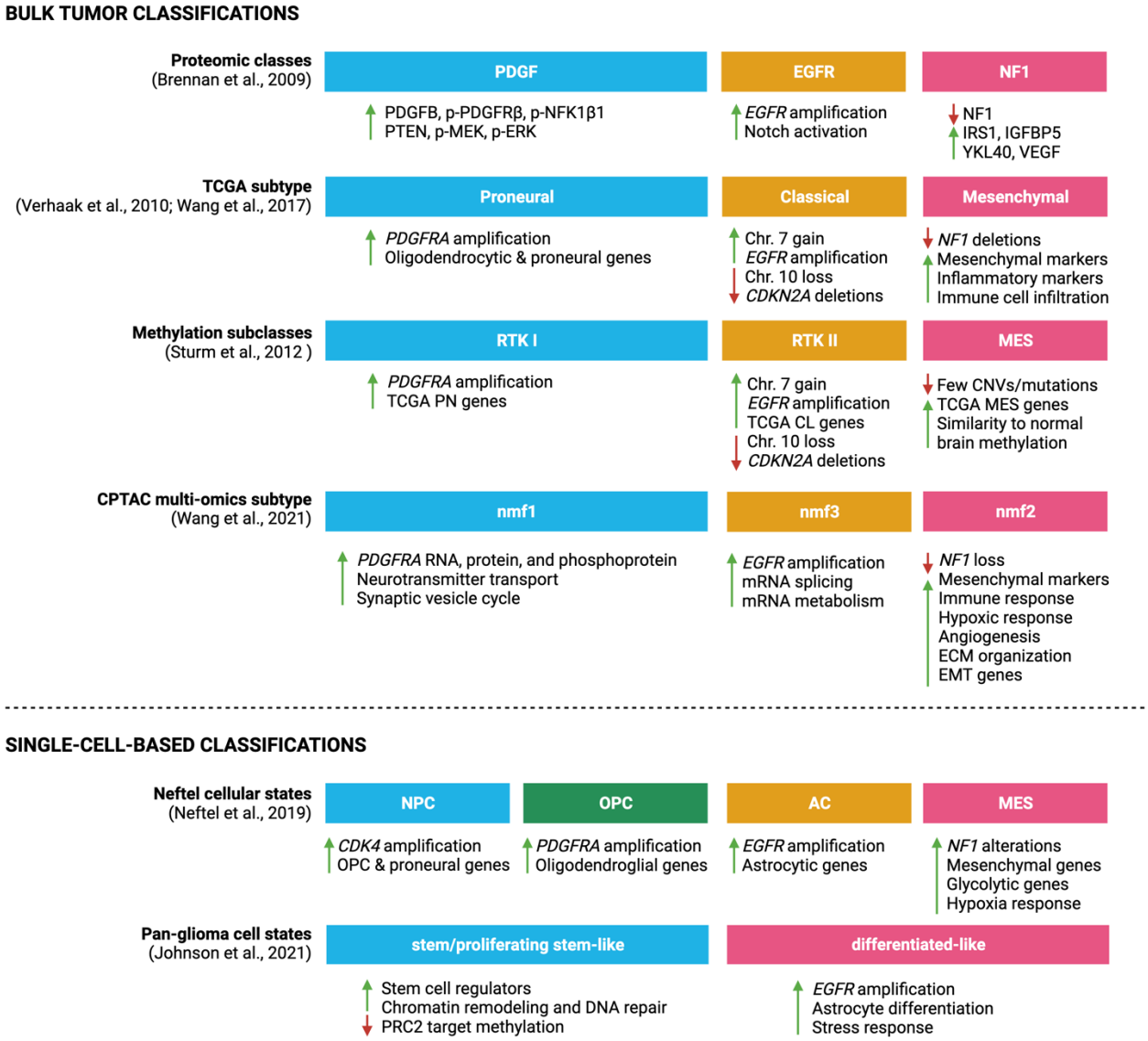

Figure 3. Summary of bulk tumor- and single-cell-based classification of IDH-wt GBMs. Main IDH-wt GBM subgroups based on proteomic, transcriptomic, DNA methylation, multi-omics profiling of bulk tumor samples along with typical molecular features (top) as well as major cellular states found in IDH-wt GBM samples (bottom) are shown. Groups are aligned according to reported enrichment or similarities in CNVs and marker expression. Alternative methylation-based classifications not widely used in the clinics were excluded from the figure. Pathway-based GBM groupings established by Garofano et al. (2021) were also excluded due to weak concordance with the depicted groups. Figure was created using BioRender.com.

1.3.2 Intratumoral heterogeneity in IDH-wt GBM

Early investigations on intra-patient genetic diversity in GBM relied on independent genetic profiling of tumor fragments from individual tumor samples. Such an approach has revealed the existence of unique oncogenic driver alterations and TCGA gene signatures from different fragments derived from the same tumor mass (36). Since then, various single-cell RNA sequencing (scRNA-seq) and single-cell DNA methylation (scDNAme) analyses have further revealed the extent of intratumoral heterogeneity in GBM (9,10,18,34,37). At the advent of this technology, Patel et al. profiled 430 $CD45^-$ (i.e., immune cell-depleted) single cells from five primary GBM samples and confirmed that each of the five tumors hosted a heterogenous combination of tumor cells whose gene expression profiles roughly corresponded to the TCGA subtypes (9). Heterogeneity was also observed at the level of RTK expression, as different cells differentially expressed various RTKs (9). Building on these findings, Neftel et al. profiled 6,864 tumor cells from an expanded cohort of 28 adult and pediatric GBM patients (10). Their analysis uncovered the co-existence of four main cellular states mimicking developmental cell types within individual tumors, with cell state frequencies roughly correlating with known genomic alterations: astrocytic-like (AC-like), mesenchymal-like (MES-like), oligodendrocyte progenitor cell-like (OPC-like), and neural progenitor cell-like (NPC-like) malignant cells (Fig. 2 and 3) (10). AC-like cells highly expressed astrocytic markers, overexpressed *EGFR*, and were enriched in tumors with the TCGA CL subtype (10). MES-like cells, which correlated with *NF1* alterations, were further divided into two subtypes: MES1-like cells expressing typical mesenchymal-related genes and MES2-like cells expressing genes involved in glycolysis and stress or hypoxia response (10). OPC-like cells expressed oligodendroglial markers and were associated with *PDGFRA* amplification (10). NPC-like cells, which were frequently *CDK4*-amplified, were further subdivided into NPC1-like and NPC2-like cells (10). These two types were distinguished by the expression of OPC-related and neuronal lineage-related genes, respectively (10). Both OPC- and NPC-like cells were associated with the TCGA PN subtype (10). Consistent with these findings, an independent comparative scRNA-seq analysis of adult GBM and normal human fetal brain cells has also shown that tumor cells resembling normal glial progenitor, astrocytic, mesenchymal, oligodendrocytic, and neuronal cells may co-exist within a single tumor (18).

Alternatively, scRNA-seq analysis has also classified IDH-wt and IDH-mut GBM tumor cells into three pan-glioma cell states: differentiated-like, stem-like, and proliferating stem-like cells (Fig. 3) (37). IDH-wt GBMs predominantly harbored differentiated-like cells and had a higher proliferating stem-like cell compartment than IDH-mut tumors (37). The differentiated-like cells in IDH-wt tumors roughly aligned with the AC- and MES-like cell states, while stem- and proliferating stem-like cells showed resemblance to the NPC- and OPC-like states (37). Expectedly, stem-like and proliferating stem-like cells were marked by activation of stem cell regulators (SOX2, SOX8, OLIG2), while differentiated-like cells exhibited activation of transcription factors involved in astrocyte differentiation (SOX9) and stress response (FOS, JUND) (37). Proliferating stem-like cells were further delineated from stem-like cells by activation of chromatin remodeling and DNA repair pathways (37). More recently, scDNAme analysis has also revealed that tumor cells from individual IDH-wt GBM samples may also span the bulk tumor TCGA LGm4-LGm5 methylation subtypes (34). LGm4 cells bore similarities to AC-like and MES-like cells and tended to be *EGFR*-amplified, while LGm5 cells exhibited Polycomb repressive complex 2 (PRC2) target hypomethylation and were more like NPC- and OPC-like cells (34). These PRC2 targets mostly included HOX and homeobox genes, as well as various transcription and growth factors that are important for stemness maintenance (34).

Apart from genetic alterations and transcriptomic features, the anatomic location of tumor tissues has also been found to be a major determinant of intratumoral heterogeneity in GBM. Tumor cells are known to reside in distinct histomorphological niches, and each of these niches has been shown to possess unique transcriptomic and proteomic signatures (38,39). The Ivy Glioblastoma Atlas Project (Ivy GAP), through RNA sequencing (RNA-Seq) of tumor blocks isolated by laser microdissection (LMD), has identified gene expression signatures that are differentially enriched in the following anatomic locations: leading edge (LE), infiltrating tumor (IT), cellular tumor (CT), pseudopalisading cells around necrosis (PAN), and microvascular proliferation (MVP) (38). Adding to this resource, a more recent proteomic analysis also showed differential protein expression that segregated across the anatomical niches initially defined by Ivy GAP (39). For example, LE sites, which consist of mostly non-malignant cells, were found to be enriched in genes and proteins involved in neuronal system processes (38,39). On the other hand, CT and PAN samples, which mostly consist of the tumor core, harbored most of the somatically mutated alleles and exhibited gene expression profiles consistent with tumor CNVs (38). Distinguishing the two areas by their gene expression

signatures, CT areas were enriched for gliogenesis and astrocyte/oligodendrocyte differentiation genes, while PAN areas highly expressed genes involved in stress and hypoxic response (38). The PAN gene expression signature was faithfully recapitulated at the protein level; on the other hand, proteins enriched in CT regions were mostly involved in growth and differentiation process (39). Expectedly, the CT and PAN regions also segregated along a protein-based hypoxia signature (39). Further proteomic analysis also revealed two distinct, mutually exclusive gene signatures—indicating either high KRAS or high MYC activity—that were evenly distributed across CT and PAN regions (39). High KRAS activity was associated with invasion, EMT processes, and the TCGA MES signature, while MYC-activated regions were linked to cell cycle progression and the TCGA PN signature (39). As another indicator of intratumoral heterogeneity, the authors further showed that individual tumor samples can contain cells with both KRAS and MYC signatures (39). Meanwhile, IT areas exhibited a gene expression profile that fell between the CT-to-LE spectrum (38). Consistent with this, IT areas expressed both stem cell-related and neuron-related proteins (39). Lastly, MVP areas, which were made up of tumor and non-malignant cells, expressed genes and proteins involved in immune and wound response, ECM organization, and expectedly, angiogenesis (38,39).

In summary, comprehensive molecular profiling of IDH-wt GBMs has provided critical insights into somatic alterations and oncogenic pathways that contribute to its development. These studies have unraveled how CNVs and mutations in certain oncogenes and tumor suppressors converge into dysregulation of key growth-promoting pathways, including RTK/RAS/PI3K, TP53, and retinoblastoma signaling (2). However, despite having vast knowledge of these genetic alterations, the field has not made significant advances in the development of effective therapies against GBM. Currently, there is emerging interest in potential actionable targets beyond somatically altered genes. These non-oncogene dependencies—which include non-somatically altered tumor-promoting proteins, cancer-associated protein-protein interaction (PPI) networks, metabolic vulnerabilities, cell state transitions and associated master regulators, and an immunosuppressive TME—greatly expand the list of potential targets and are thought to be the next frontier in cancer therapeutics (40). Functional investigations are now needed to decipher which of these non-oncogene dependencies can confer tumor-specific advantages and thus be promising targets in the context of GBM. Among these emerging targets is epithelial membrane protein 3 (EMP3), an enigmatic membrane protein that is proposed to play a tumor-promoting function in GBM.

1.4 Epithelial Membrane Protein 3

1.4.1 Protein structure and localization

The gene for Epithelial Membrane Protein 3 (*EMP3*), located in the human chromosome 19q13.3, encodes a small, ~18 kilodalton (kDa), tetraspan membrane protein composed of 163 amino acids (41,42). Structurally, the EMP3 protein shares significant homology with other members of the peripheral myelin 22-kDa (PMP22) family, including EMP1, EMP2, and PMP22 (43,44). In particular, the second and fourth membrane-spanning domains of these tetraspanins are highly conserved within this family (43,44). Apart from having four membrane-spanning domains, EMP3 also contains two extracellular domains (ECDs), a short intracellular loop, and cytoplasmic N- and C-terminal tails (Fig. 4A). The large (41 aa) and small (18 aa) ECDs are located between the first two and the last two transmembrane segments, respectively. The former is experimentally confirmed to be *N*-glycosylated at asparagine 47 (N47) (45). Multiple glycan modifications putatively exist at this position, as suggested by the presence of multiple bands migrating between 20-30 kDa in Western blotting experiments (45). On the other hand, the short intracellular loop in between its second and third transmembrane regions is predicted to contain a phosphorylatable threonine residue at position 90; however, this remains to be experimentally validated (44).

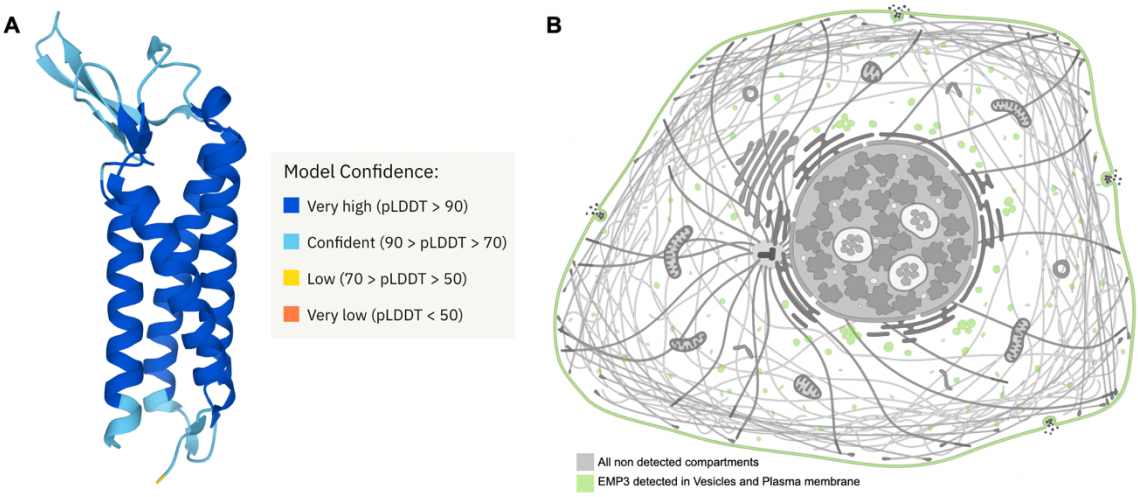

Figure 4. EMP3 structure, localization and expression pattern. A) Predicted protein structure of human EMP3 from the AlphaFold Protein Structure Database (https://alphafold.ebi.ac.uk/, Accessed 27 February 2022). Residues are color-coded according to confidence levels. B) Subcellular localization of EMP3 according to the Human Protein Atlas. Image obtained from the Human Protein Atlas using human EMP3 as the query protein (https://www.proteinatlas.org/, Accessed 10 June 2022).

Immunostaining experiments by Human Protein Atlas (HPA, http://www.proteinatlas.org) showed that EMP3 localizes within the plasma membrane and within cytoplasmic vesicles (Fig. 4B) (46). Consistent with the latter, a yeast-two-hybrid (Y2H) screen has identified EMP3's interaction with several proteins that regulate endosomal trafficking (e.g., FLOT1, HTATIP2, RAB10, VAMP3) (45). In addition, the same study featured an immunofluorescence experiment showing partial co-localization between EMP3 and the Golgi marker RCAS1 (45). Apart from these, detailed information about EMP3's subcellular location remains lacking, and the exact identity of EMP3-positive vesicles remains to be clarified.

1.4.2 Physiological expression and function of EMP3

EMP3 is widely expressed across different tissues and is notably enriched in a subset of cell types, including blood cells, various types of epithelial and mesenchymal cells, smooth muscle cells and skeletal myocytes, as well as secretory cells with an endocrine or glandular function (Fig. 5A) (47). Single-cell expression data from the HPA suggest that among these cells, EMP3 levels are highest in immune cells (48). These include natural killer (NK) cells, dendritic cells, B cells, T cells, granulocytes, monocytes, and macrophages. The latter group consists of specialized macrophages found in various organs, including Langerhans cells in the skin, Kupffer cells in the liver, and Hofbauer cells in the placenta (Fig. 5B). While EMP3's function within immune cells remains largely unexplored, one study has shown how Emp3 in mouse-derived macrophages can modulate the activation of $Cd8^+$ T cytotoxic T cells (49). Emp3-overexpressing macrophages inhibited $Cd8^+$ T cell induction and proliferation via increased Tnf-α production by macrophages and reduced expression of Il-2rα by T cells. Conversely, Emp3 knockdown in macrophages led to increased T cell activation.

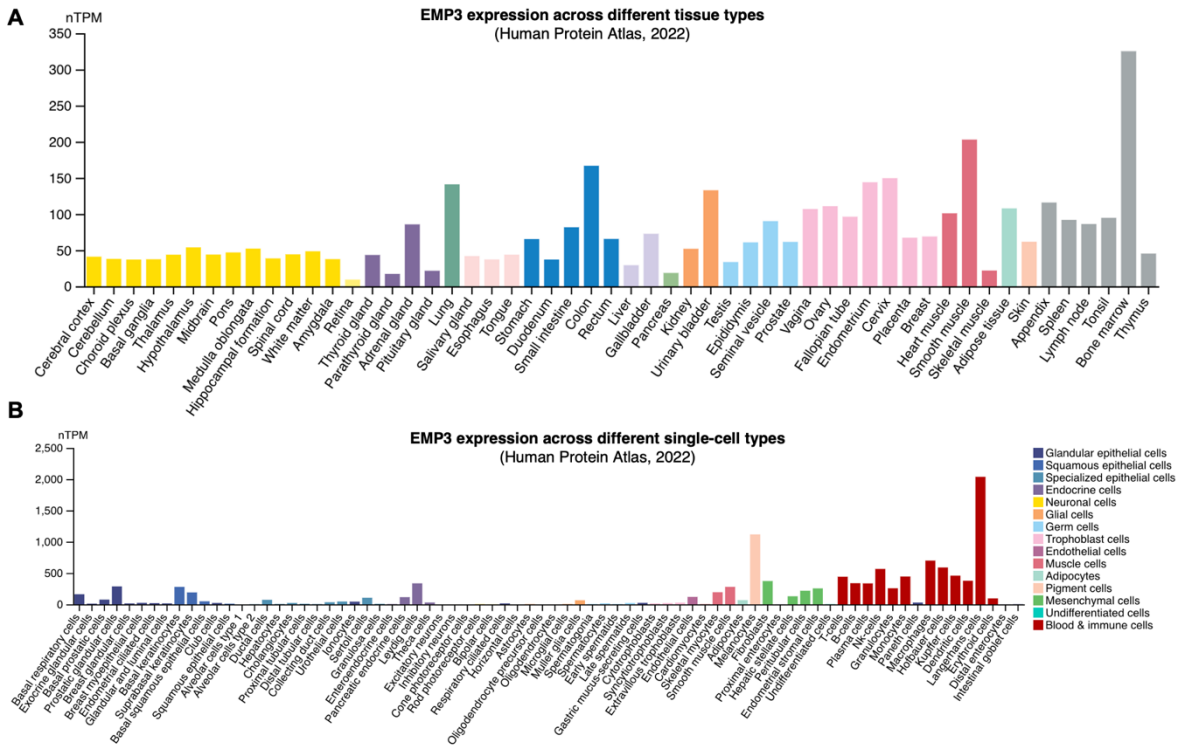

Figure 5. EMP3 expression across different tissue and single-cell types according to the Human Protein Atlas. The bar graph shows the mean EMP3 expression (nTPM) in each A) tissue or B) single-cell type as defined by the HPA. Bars are color-coded according to tissue belonging to the same organs or cell type groups that share functional features.

Apart from immune cells, EMP3 is also noted to be expressed in erythroid cells. In fact, the *EMP3* gene has been discovered to encode the MAM blood group antigen in erythrocytes (50). Functionally, EMP3 has been shown to regulate erythropoiesis by influencing the levels and distribution of the CD44 antigen (CD44), a known EMP3-interactor, in these cells (50). Erythroid progenitors derived from MAM-negative individuals were more proliferative, a phenotype that was associated with broader CD44 distribution and increased CD44 expression in the cleavage furrow of dividing cells (50). At later stages of erythrocyte differentiation, however, a reduction in overall CD44 levels was observed in MAM-negative erythrocytes (50). This suggests that EMP3 may serve to stabilize CD44 in mature red blood cells through a currently unknown mechanism.

In contrast, EMP3 expression is relatively low across different adult brain regions. Data from the HPA suggest that only a few cell types—most notably astrocytes and microglia—express EMP3 in the adult human brain (Fig. 6A) (48). This was supported by an independent single-nucleus RNA sequencing (snRNA-seq) dataset of the adult cortex, which showed detectable EMP3 expression only in astrocytes, microglia, and endothelial cells (51). Interestingly, in developing human brain organoids, EMP3 was found to be high in cycling progenitor cells,

radial glia, as well as in mesenchymal-like cells (Fig. 6B) (51). Pseudotime-ordering of EMP3 expression levels in these organoids further showed that EMP3 expression peaks upon the emergence of NPC states and substantially declines as differentiated neuronal lineages appear (Fig. 6C) (51). In line with the HPA and Kanton datasets, an independent scRNA-seq profiling and pseudotime analysis of 23-day-old to 6-month-old human brain organoids indicated that EMP3 levels peaks in both early progenitor cell populations (e.g. radial glia) and in terminally differentiated astroglial lineages (Fig. 6D) (52). Mimicking this temporal trajectory, Emp3 levels were also found to be differentially expressed during sciatic nerve development in mice (53). In this instance, *Emp3* mRNA expression was observed to peak between postnatal days 0-21 but became almost undetectable in the adult sciatic nerve (53). Interestingly, Emp3 expression was also observed to increase rapidly and steadily during sciatic nerve regeneration after crush injury (53). Increased Emp3 immunoreactivity was noted particularly in areas with proliferating Schwann cells, suggesting that it may play a role in remyelination (53). Taken together, these findings indicate that while EMP3 is absent in most cell types of the adult nervous system, its expression may be developmentally regulated and may be relevant at the early stages of nervous system development. Upon maturation, EMP3 expression persists but only within astrocytic and microglial cell types. Nerve injury-induced re-expression of EMP3 in mature glial lineages, in turn, may serve to achieve EMP3's presumed neurogenic function.

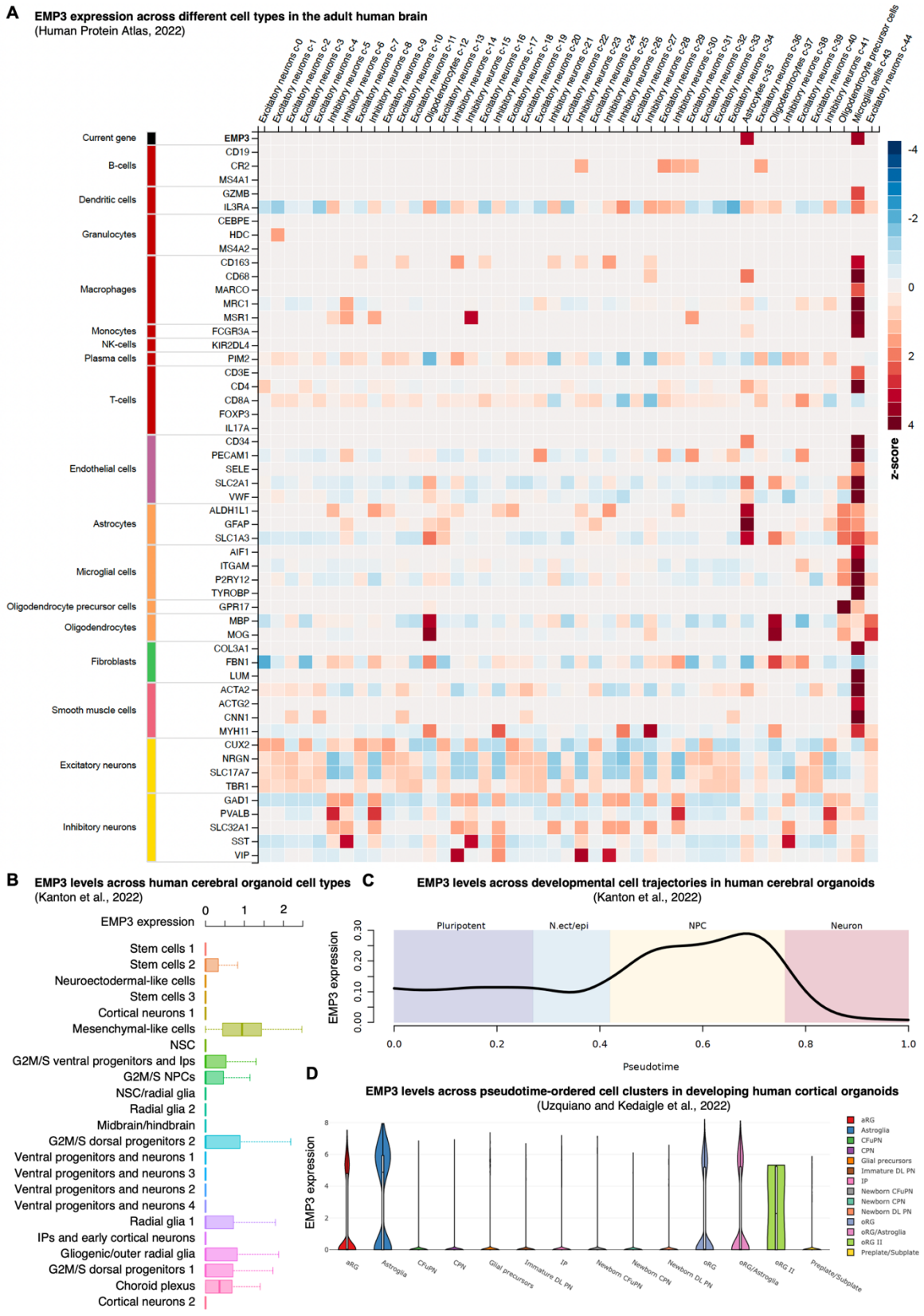

Figure 6. EMP3 expression in the normal human brain and in developing brain organoids. A) EMP3 mRNA expression across different single-cell types in the adult human protein. B) EMP3 levels across human cerebral organoid cell types. C) EMP3 levels across developmental trajectories in human cerebral organoids. D) EMP3 levels across pseudotime-ordered cell clusters in developing human cortical organoids. Figures were obtained from publicly available dataset portals (48,51,52)

Regardless of the highly specific role that EMP3 may play in T cell induction (49), erythropoiesis (50), and nerve regeneration (54), EMP3 seems to be generally dispensable for normal physiology. This is supported by the existence of individuals with inactivating mutations in EMP3 (50). These individuals did not have obvious medical conditions, except for documented cases of hemolytic disease of the newborn in EMP3-negative mothers (50). These patients also failed to exhibit erythrocytosis, despite having $CD34^+$ progenitor cells that displayed increased erythropoiesis *ex vivo* (50). Likewise, an Emp3 knockout mouse generated by the German Mouse Clinic has been documented to have no adverse phenotypes, except for minor alterations in frequencies of certain leukocyte populations.

1.4.3 Tumor-suppressive and oncogenic functions of EMP3

EMP3 has been implicated in various cancer types, either as a tumor suppressor or an oncogene. In oligodendroglioma and neuroblastoma, the EMP3 promoter was observed to be frequently hypermethylated (55). This hypermethylation was associated with poorer survival, leading to the hypothesis that EMP3 may be a tumor suppressor in these entities (55). Supporting this, EMP3 overexpression in EMP3-hypermethylated neuroblastoma cell lines led to restricted *in vitro* colony formation and tumor growth *in vivo* (55). Similarly, EMP3 expression was noted to be repressed in non-small cell lung cancer (NSCLC) (56), esophageal squamous cell carcinoma (ESCC) (57), and gallbladder cancer (GBC) (58). In all three entities, EMP3 expression also positively correlated with poorer survival. Furthermore, EMP3 overexpression inhibited the growth of ESCC and GBC cells *in vitro* (57,58). Additionally, the *in vitro* phenotype of GBC cells correlated with inactivated MAPK/ERK signaling and translated to reduced tumor burden *in vivo* (58). Meanwhile, contrasting results have been reported in breast cancer. While one study noted a positive correlation between EMP3 expression and several indicators of disease severity (e.g., histological grade, lymph node metastasis, and ERBB2 expression) (59), another study showed an inverse relationship between EMP3 expression and breast cancer patient survival (60). The latter further demonstrated that EMP3 negatively regulates the cell cycle S-phase, impairs DNA damage repair, inhibits AKT/mTOR signaling, and limits the stem cell-like phenotypes *in vitro* (60).

On the other hand, EMP3's oncogenic function has been mainly attributed to its ability to promote RTK signaling. In chondrosarcoma cells, short hairpin RNA (shRNA)-mediated knockdown of EMP3 led to reductions in phosphorylated EGFR (p-EGFR), phosphorylated AKT (p-AKT), and phosphorylated ERK (p-ERK) (45). Impaired RTK signaling correlated

with cancer hallmarks, as EMP3 knockdown cells were less proliferative, had reduced wound healing capacity, and were more sensitive to apoptosis induced by staurosporine (STS) and tumor necrosis factor-related apoptosis-inducing ligand (TRAIL) (45). Reduced p-ERK and p-AKT levels, which were attributed to downregulation of the PI3K regulatory subunit p85, were also documented upon shRNA-mediated knockdown of EMP3 in hepatocellular carcinoma (HCC) cells (61). Likewise, these cells exhibited reduced proliferation rates and attenuated tumor growth *in vivo* (61). Increased levels of the RTK ERRB2, the PI3K catalytic subunit p110α, and p-AKT were also noted upon EMP3 overexpression in human bladder cancer cells (62). Conversely, knockdown of EMP3 reversed these effects (62). Supporting results obtained with chondrosarcoma and HCC cells, EMP3 activation in bladder cancer cells also promoted cell proliferation, as quantified by phenotypic assays and Ki-67 expression (62).

Apart from RTK-dependent mitogenic signaling, EMP3 has also been implicated in the regulation of ECM receptors and degraders. In the same study involving human bladder cancer cells, EMP3 overexpression also upregulated the expression of several integrins at the transcript level (62). Enhanced integrin expression correlated with upregulation of focal adhesion kinase (FAK) and phosphorylated SRC (62). Consistent with activated FAK signaling, the study also noted upregulation of the FAK targets Rho-associated protein kinase 1 (ROCK1) and 2 (ROCK2) upon EMP3 overexpression (62). Expectedly, the opposite effect was noted upon EMP3 knockdown (62). Ultimately, EMP3-mediated activation of FAK/ROCK signaling correlated with increased cellular migration *in vitro* (62). Similarly, reduced cellular motility and invasiveness were observed upon EMP3 knockdown in HCC cells (61). In contrast to bladder cancer cells, this phenotype was attributed to concomitant reductions of key ECM degraders, including matrix metalloproteinase 9 (MMP-9) and urokinase-type plasminogen activator (uPA) (61).

Detailed mechanistic insights about EMP3-dependent regulation of receptor signaling remain limited. Since there are no experimentally confirmed catalytic domains within the protein, it is presumed that EMP3 exerts these effects either structurally (i.e., by organizing receptor microdomains within the membrane) or by regulating receptor trafficking mechanisms (42,45). While it is unknown whether EMP3 physically interacts with RTKs and/or integrins to support their signaling, one study has noted EMP3's physical association with the EGFR regulators FLOT1 and HTATIP2 (45). FLOT1 facilitates RTK signaling by inducing EGFR and ERBB2 clustering within lipid rafts (63); on the other hand, HTATIP2 promotes EGFR degradation

and attenuates endosomal RTK signaling via increased acidification of endosomes containing EGFR cargoes (64). Thus, it is presumed that EMP3 cooperates with or inhibits these proteins to indirectly affect EGFR signaling. More studies, however, are clearly needed to finely dissect EMP3's effect on EGFR and other receptors.

1.4.4. EMP3 in IDH-wt GBM

While lowly expressed in the adult human brain, EMP3 is frequently upregulated in the setting of IDH-wt GBM (10,25,26,38,42,65,66). Analysis of bulk RNA-seq data from the TCGA GBM dataset shows that EMP3 is highly expressed across the most common Sturm methylation subclasses compared to normal brain tissue (Fig. 7A). Comparing the three subclasses, EMP3 levels appear to be higher in MES and RTK II/CL GBMs compared to RTK I/PN GBMs (25,26,67). Segregating GBM tissues based on Ivy GAP anatomic features, EMP3 levels appear to be relatively higher in the perinecrotic zone (PNZ) of the tumor core, as well as in tumor-rich CT and PAN regions (Fig. 7B) (38). On the other hand, Ivy GAP regions harboring non-malignant cells (e.g., LE and MVP regions) show relatively low expression of EMP3 (38). These observations indicate that malignant cells mostly account for high EMP3 expression observed in bulk tumor samples. Supporting this, scRNA-seq of IDH-wt GBMs indicated that malignant cells comprise most of the EMP3-overexpressing cells (Fig. 7C) (10). Additionally, tumor-infiltrating macrophages and T cells were also found to express high levels of EMP3 (10,68), a potentially physiologically relevant observation that is in line with the documented expression of EMP3 in immune cells (47–49). Further mapping of single-cell EMP3 expression onto the four main Neftel GBM cellular states showed exclusive overexpression of EMP3 in AC-like and MES-like cells (Fig. 7D) (10). This corresponds with the TCGA bulk tumor analysis, given that these two cell states roughly correspond to the MES and RTK II/CL subtypes (10). In parallel, an independent scRNA-seq dataset also showed that IDH-wt GBM tumor cells exhibiting the highest levels of EMP3 greatly resemble radial glial cells (Fig. 7E) (69). This observation is consistent with known physiological expression patterns of EMP3 in the normal human brain and in developing brain organoids (48,51,52); furthermore, it hints at how GBM cells may recapitulate neurodevelopmental trajectories based on gene expression similarities. Given its apparent progenitor cell type- and stage-specific expression in developing brain organoids, it is likely that EMP3 plays a role in proliferative cell populations during neurodevelopment.

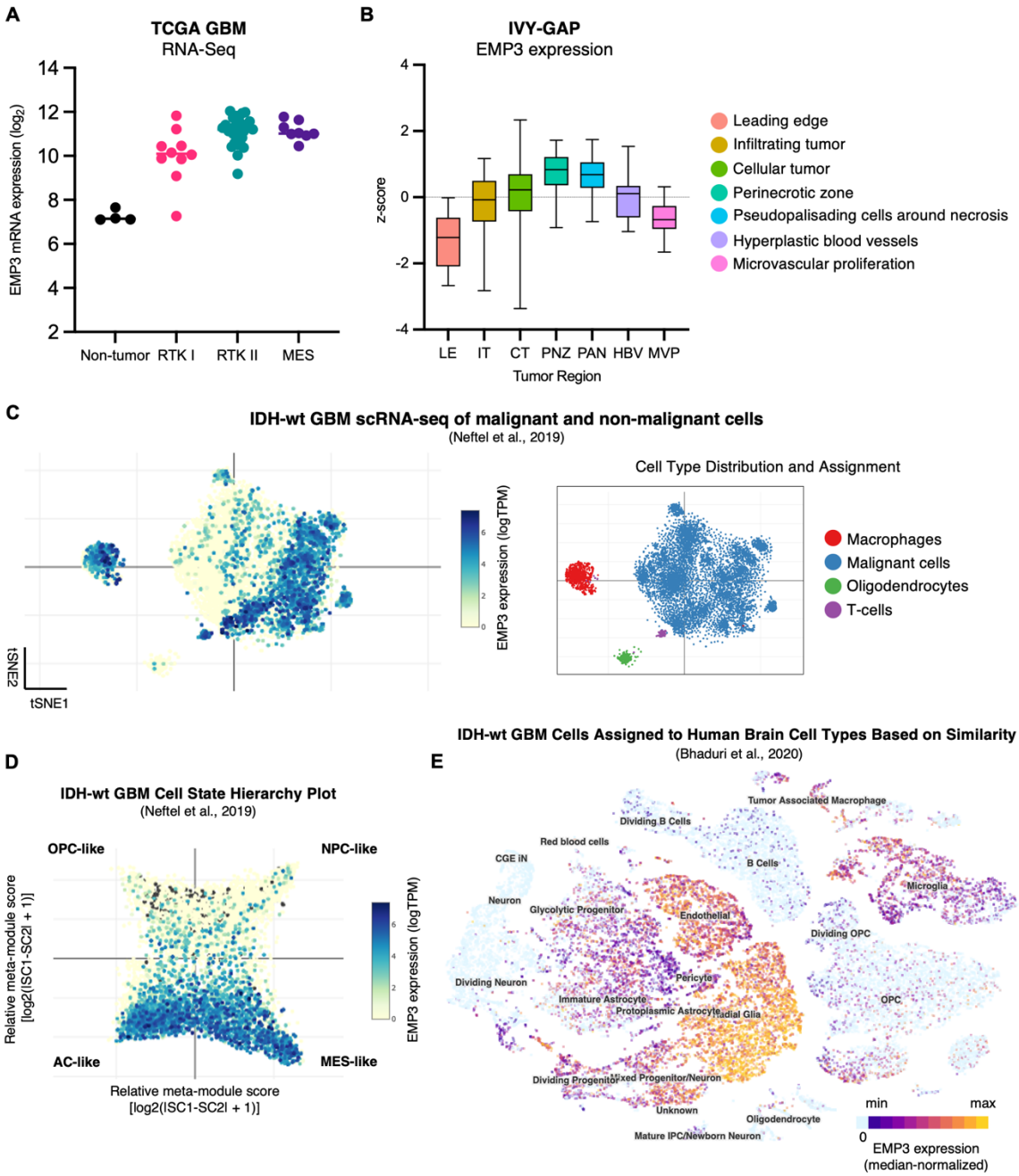

Figure 7. EMP3 expression in IDH-wt GBM. A) EMP3 mRNA expression levels in TCGA GBM samples as measured by bulk tumor RNA-seq (25,67). B) EMP3 expression z-scores across Ivy GAP anatomic regions (38). C) t-distributed stochastic neighbor embedding (tSNE) plot indicating the expression pattern of EMP3 in the major cell types isolated from IDH-wt GBM samples (10). D) Cell state hierarchy plot showing EMP3 expression levels across single cells distributed across the four GBM cellular states (10). E) Uniform Manifold Approximation and Projection (UMAP) plot showing median-normalized EMP3 levels in GBM cells classified according to similarity to human brain cell types (69). Figures were generated based on publicly available datasets or obtained from publicly accessible visualization portals.

Apart from being a characteristic feature of IDH-wt GBMs, EMP3 expression has also been used to prognosticate patient survival. High EMP3 expression has been correlated with shorter overall survival (OS) of GBM patients from the TCGA cohort (65,66). Moreover, *EMP3* is frequently included in gene lists that are predictive of patient survival. These include a four-gene panel (*NMB, RTN1, GPC5, EMP3*) wherein high EMP3 levels positively correlated with

poorer OS (70), a three-gene panel (*PPIC, EMP3, and CHI3L1*) associated with short-term survival (71), and a 60-gene panel enriched with clinically unfavorable mesenchymal biomarkers (72) The latter study, which showed drastic reduction of EMP3 expression in long-term survivors (72), also aligns with a parallel study showing high co-expression of EMP3 with other mesenchymal genes in short-term survivors (73). Thus, EMP3 appears to be part of a mesenchymal transcriptional program that imparts poorer prognosis in GBM patients. Indeed, EMP3 is exclusively part of the Verhaak MES gene signature (25,26), although it is also highly expressed in RTK II/CL tumors.

Despite these clinical associations, only a few studies have provided functional insights into the oncogenic role of EMP3 in IDH-wt GBM. One study, which focused on the cell-autonomous effects of EMP3 in IDH-wt GBM cells marked by high levels of the mesenchymal marker CD44, demonstrated how EMP3 activates transforming growth factor beta (TGF-β) signaling (66). Upon TGF-β induction, EMP3 physically interacts with and activates the TGF-β receptor TGFBR2 (66). On the other hand, EMP3 depletion reduced TGF-β-dependent SMAD 2/3 phosphorylation, transcription of TGF-β target genes, and cellular proliferation *in vitro* (66). Impaired TGF-β signaling, as shown by reduced SMAD 2/3 activation, was also apparent in intracranially implanted xenografts harboring the EMP3 shRNA (66). Moreover, the EMP3-depleted xenografts grew slower compared to controls, providing a correlation between the observed biochemical effects and actual tumor behavior (66). Consistent with this, and in contrast to an earlier study performed on NSCLC cells (56), EMP3-dependent activation of TGF-β/SMAD signaling has also been recently demonstrated in NSCLC overexpressing the cancer stem cell marker aldehyde dehydrogenase 1 (ALDH1) (74).

In addition, EMP3 was also shown to regulate the immune microenvironment of IDH-wt GBM tumors. CRISPR/Cas9-mediated knockout of EMP3 in GL261 xenografts led to reduced tumor burden and prolonged survival in mice (75). Contributory to this was the reduced GBM infiltration of tumor-associated macrophages (TAMs) with the immunosuppressive M2 phenotype (75). Furthermore, the proponents demonstrated that EMP3 KO increased $CD4^+$ and $CD8^+$ T cell infiltration into tumors in a CXCR3-dependent manner, thereby synergistically improving the effects of anti-PD1 therapy *in vivo* (75). Collectively, the two abovementioned studies suggest that EMP3 not only promotes intrinsic oncogenic processes within GBM cells, but also actively shapes the tumor microenvironment to further facilitate tumor development.

1.5 Objectives of the study

Despite recent findings, a comprehensive understanding of EMP3's function in the context of IDH-wt GBM remains elusive. Of particular interest is the possible role of EMP3 in the regulation of oncogenic membrane receptors in GBM, given the central involvement of these receptors in most IDH-wt tumors (42). EMP3 has been documented to be critical for the activity of these oncogenic receptors in several non-glioma models (42), suggesting that it may very well be a non-oncogene dependence in IDH-wt GBM. PPI studies using non-GBM models have further identified potential mechanisms by which EMP3 could regulate oncogenic receptor signaling (45); however, whether these findings are applicable to GBM or whether EMP3 operates within a unique GBM- or GBM subtype-specific interaction network remains to be elucidated. Integrating interactome analysis with the molecular and phenotypic evaluation of various loss-of-function models in different GBM cell types is expected to provide a broader and deeper picture of EMP3's role in GBM development. Moreover, such an approach is expected to explain how EMP3 could contribute to therapeutic resistance in GBM, thereby clarifying EMP3's potential as viable pharmaceutical target in IDH-wt GBM.

Given these, the study set out to fulfill the following specific objectives:

1) Define EMP3's interaction network within the context of GBM;
2) Investigate how EMP3 can regulate the activity of GBM-associated oncogenic receptors across different cellular backgrounds;
3) Assess the therapeutic potential of EMP3 inhibition through phenotypic characterization of *in vitro* knockdown models.

2 Materials

2.1 Materials

2.1.1 Cell Culture

Table 3. IDH-wt GBM cell lines used in this study

Cell Line	Origin	Source
DK-MG	GBM derived from the right parietal lobe of a 67-year old female patient	DSMZ
LN-18	GBM derived from the right temporal lobe of a 65-year old male patient	ATCC
U-118	GBM derived from a 50-year old male with grade 4 malignant glioma	ATCC

Table 4. Cell culture media and supplements

Media or Supplement	Supplier
Antibiotic-antimycotic	Gibco™
Biotin	Sigma-Aldrich
Blasticidin S hydrochloride	US Biological Life Sciences
Cycloheximide (100 mg/mL)	Sigma-Aldrich
Dulbecco's Modified Eagle Medium with high glucose, GlutaMax™ and pyruvate	Gibco™
Dulbecco's Phosphate-Buffered Saline	Gibco™
Fetal Bovine Serum	Gibco™
Human epidermal growth factor	Peprotech
Human hepatocyte growth factor	Peprotech
Hyaluronic acid sodium salt (500-750 kDa)	Sigma-Aldrich
Opti-MEM™ Reduced Serum Medium	Gibco™
Osimertinib (AZD9291)	MedChemExpress
Puromycin dihydrochloride	MP Biomedical
Synth-a-Freeze™ Cryopreservation Medium	Gibco™
Trypan blue	Sigma-Aldrich
Trypsin (2.5%), no phenol red	Gibco™
X-tremeGENE™ 9 DNA transfection reagent	Roche

2.1.2 Molecular Biology

Table 5. Gateway™-compatible entry clones and destination vectors used in this study

Plasmid	Description	Application
EMP3 +/- STOP in pDONR221	Entry clone containing the coding sequence of wild-type EMP3	LR cloning of BioID2, FLAG IP, and rescue plasmids
EMP3 N47A +/- STOP in pDONR221	Entry clone containing the coding sequence of EMP3 N47A mutant	
pMXs-GW-Myc-Linker-BioID2	Destination vector for Gateway™ LR cloning of BioID2 expression constructs	LR cloning of BioID2 plasmids
TagRFP -STOP in pDONR201	Entry clone containing the coding sequence of TagRFP	
GAP-TagRFP -STOP in pDONR201	Entry clone containing the coding sequence of membrane-localizing TagRFP	
pMXs-GW-FLAG-IRES-PuroR	Destination vector for Gateway™ LR cloning of FLAG pull-down constructs	LR cloning of FLAG pull-down plasmids
CD44s +/- STOP in pDONR201	Entry clone containing the coding sequence of the full-length CD44 standard isoform (CD44s)	
CD44s Δ2-222 -STOP in pDONR201	Entry clone containing the CD44s coding sequence without the N-terminal ECD	
CD44s Δ2-268 -STOP in pDONR201	Entry clone containing the CD44s coding sequence without the ECD and stem domain	
CD44s ICD -STOP in pDONR201	Entry clone containing the coding sequence of the intracellular domain of CD44s	
pMXs-GW-IRES-BsdR	Destination vector for Gateway™ LR cloning of rescue constructs	LR cloning of rescue plasmids
pMXs-GW-FLAG-IRES-BsdR	Destination vector for Gateway™ LR cloning of FLAG-tagged rescue constructs	
TBC1D5 -STOP in pDONR223	Entry clone containing the coding sequence of wild-type TBC1D5	
TBC1D5 R169A/Q204A in pDONR223	Entry clone containing the coding sequence of TBC1D5 R169A/Q204A mutant	

Table 6. Gateway™-compatible expression constructs used in this study

Plasmid	Description	Application
EMP3 -STOP in pMXs-GW-Myc-Linker-BioID2	Expresses the EMP3-BioID2 fusion protein	BioID2
EMP3 N47A -STOP in pMXs-GW-Myc-Linker-BioID2	Expresses the EMP3 N47A-BioID2 fusion protein	
TagRFP -STOP in pMXs-GW-Myc-Linker-BioID2	Expresses the TagRFP-BioID2 fusion protein	
GAP-TagRFP -STOP in pMXs-GW-Myc-Linker-BioID2	Expresses the GAP-TagRFP-BioID2 fusion protein	
EMP3 -STOP in pDEST26 FLAG-C	Expresses the EMP3-FLAG fusion protein	AP-MS
EMP3 N47A -STOP in pDEST26 FLAG-C	Expresses the EMP3-FLAG fusion protein	
TagRFP -STOP in pDEST26 FLAG-C	Expresses the EMP3-FLAG fusion protein	
CD44s -STOP in pMXs-GW-FLAG-IRES-PuroR	Expresses the CD44s-FLAG fusion protein	FLAG pull-downs
CD44s ΔNTD -STOP in pMXs-GW-FLAG-IRES-PuroR	Expresses the CD44s- FLAG fusion protein without CD44s amino acids 2-222	
CD44s ΔNTD-stem -STOP in pMXs-GW-FLAG-IRES-PuroR	Expresses the CD44s-FLAG fusion protein without CD44s amino acids 2-268	
CD44s ICD -STOP in pMXs-GW-FLAG-IRES-PuroR	Expresses the CD44s intracellular domain-FLAG fusion protein	
EMP3 -STOP in pMXs-GW-FLAG-IRES-PuroR	Expresses the EMP3-FLAG fusion protein	
EMP3 N47A -STOP in pMXs-GW-FLAG-IRES-PuroR	Expresses the EMP3 N47A-FLAG fusion protein	
EMP3- STOP in pMXs-GW-IRES-BsdR	Expresses untagged EMP3 WT	Rescue experiments
TBC1D5 -STOP in pMXs-GW-FLAG-IRES-BsdR	Expresses wild-type TBC1D5	Rescue experiments
TBC1D5 R169A/Q204A in pMXs-GW-FLAG-IRES-BsdR	Expresses the TBC1D5 R169A/Q204A mutant	Rescue experiments

Table 7. Primers used for assembly of BioID2 destination vector

PCR Product	Forward Primer	Reverse Primer
pMXs-Gateway backbone	CTACGGCTACACTAGAAGAACAGTATTTGGTATC	CCCGTCAACCACTTTGTACAAGAAAGCTG
Myc-Linker	TGTACAAAGTGGTTGACGGGGAACAAAAACTCATCTCAGAAGAGGATCTCGACGGTGGAGGCGGGTCTGGA	GGTTCTTGAAACCGGTCGATCCACCGCC
Linker-BioID2	ATCGACCGGTTTCAAGAACCTGATCTGG	AATTTACGTAGCGGCCGCGGTTAGCTTCTTCTCAGGCTG
IRES-PuroR	CCGCGGCCGCTACGTAAATT	TTCTTCTAGTGTAGCCGTAGTTAGGCCACC

Table 8. Primers used for site-directed mutagenesis

PCR Product	Forward Primer	Reverse Primer
GAP-TagRFP	CTGTGCTGTATGAGAAGAAC CAAACAGAGCGAGCTGATTA AGGAGAACATGC	GTTCTTCTCATACAGCACAG CATGGTGGAGCCTGCTTTTTT GT
TBC1D5 R169A	GTCAAAGCAACGTTTCCTGA AATGCAGTTTTTCCA	GGAAACGTTGCTTTGACATC TTGTTCAATCATTGATCGAA GT
TBC1D5 Q204A	TTATAAAGCGGGCATGCACG AACTGTTAGC	TGCATGCCCGCTTTATAAAG CAACTGCTCGTTTTCTCTGG

Table 9. Primers used for BP cloning of CD44s truncation mutants without stop codon

CD44s	Forward Primer	Reverse Primer
Full-length	CAAAAAAGCAGGCTCCACCAT GGACAAGTTTTGGTGGC	CAAGAAAGCTGGGTTCACCC CAATCTTCATGTCC
ΔNTD	CAAAAAAGCAGGCTCCACCAT GAGAGACCAAGACACATTCCA	
ΔNTD-stem	CAAAAAAGCAGGCTCCACCAT GTGGCTGATCATCTTGGC	
ICD	CAAAAAAGCAGGCTCCACCAT GAACAGTCGAAGAAGGTGT	

Table 10. Primary antibodies

Target Protein	Host	Isotype	Supplier	Application	Dilution
β-actin	Rabbit	IgG	CST	WB	1:1000
CD44	Mouse	IgG2a	CST	WB IF	1:1000 1:400
CLINT1	Rabbit	Polyclonal IgG	Thermo Fisher	IF/PLA	1:50
EGFR	Rabbit	IgG	CST	WB PLA	1:1000 1:50
EMP3	Mouse		DKFZ Antibody Core Facility	WB IF/PLA	Undiluted Undiluted
FLAG	Mouse	IgG1	Sigma-Aldrich	WB	1:1000
MET		IgG	CST	IF	1:400
Myc	Rabbit	IgG	CST	WB IF	1:1000 1:200
p-EGFR (Y1068)	Mouse	IgG1	Thermo Fisher	PLA	1:100
p-EGFR (Y1068)	Rabbit	IgG	CST	WB	1:1000
RAB7	Rabbit	IgG	CST	PLA	1:100
SNX1	Rabbit	IgG	Thermo Fisher	PLA	1:100
SNX2	Rabbit	Polyclonal IgG	Thermo Fisher	PLA	1:100
SOX2	Rabbit	IgG	CST	PLA	1:400
TBC1D5	Rabbit	Polyclonal IgG	Abcam	PLA	1:200
VPS53	Rabbit	Polyclonal IgG	Thermo Fisher	PLA	1:50

Table 11. Secondary antibodies

Target	Host	Supplier	Application	Dilution
Streptavidin-horseradish peroxidase (HRP)	N/A	CST	WB	1:2000
Anti-rabbit IgG, HRP-linked	Goat	CST	WB	1:4000
Anti-mouse IgG, HRP-linked	Horse	CST	WB	1:4000
Anti-rabbit IgG, F(ab')$_2$ Fragment AlexaFluor 488 Conjugate	Goat	CST	IF	1:1000
Anti-mouse IgG, F(ab')$_2$ Fragment, AlexaFluor 594 Conjugate	Goat	CST	IF	1:1000

Table 12. Commercial assays and kits

Assays and Kits	Supplier
Caspase-Glo® 3/7 Assay System	Promega
CellTiter-Glo® Luminescent Cell Viability Assay	Promega
NaveniFlex MR	Navinci
NucleoSpin Gel and PCR Clean-Up	Macherey-Nagel
Nucleospin Plasmid	Macherey-Nagel
Nucleospin RNA	Macherey-Nagel
Nucleospin Tissue	Macherey-Nagel
pGEM®-T Easy Vector Systems kit	Promega
Pierce™ BCA Protein Assay Kit	Thermo Scientific™
Pierce™ Cell Surface Biotinylation and Isolation Kit	Thermo Scientific™
WesternBright Sirius Chemiluminescent Detection Kit	Advansta

Table 13. Affinity resins

Resin	Supplier
Pierce™ Anti-FLAG (DYKDDDDK) Affinity Resin	Thermo Scientific™
Pierce™ High Capacity Streptavidin Agarose Resin	Thermo Scientific™

Table 14. Bacterial strains

Bacteria	Supplier
NEB® 5-alpha competent *Escherichia coli* (*E. coli*)	New England Biolabs
One Shot™ TOP10 chemically competent *E. coli*	Invitrogen™
One Shot™ *ccd* B Survival™ 2 T1 R competent *E. coli*	Invitrogen™

Table 15. Enzymes and enzymatic master mixes

Enzyme/Master Mix	Supplier
Anza™ Bsp1407I	Invitrogen™
Anza™ EcoRI	Invitrogen™
Gateway™ BP Clonase™ II Enzyme Mix	Invitrogen™
Gateway™ LR Clonase™ II Enzyme Mix	Invitrogen™
NEBuilder® HiFi DNA Assembly Kit	New England Biolabs
PNGase F	New England Biolabs
Q5® High-Fidelity 2X Master Mix	New England Biolabs

Table 16. Other chemicals and reagents

Chemical/Reagent	Supplier
2-Mercaptoethanol	Sigma-Aldrich
Agar	AppliChem
Agarose	Sigma-Aldrich
Ampicillin sodium salt	Serva
Boric acid	Sigma-Aldrich
Chloramphenicol	Sigma-Aldrich
Coomassie Brilliant Blue G250	Sigma-Aldrich
Dimethylsulfoxide	Carl Roth
Dithiothreitol	Thermo Scientific™
Eppendorf tubes (1.5/2 mL)	Eppendorf
Ethanol, absolute (99.8%)	VWR International
Ethidium bromide (10 mg/mL)	Carl Roth
Ethylenediaminetetraacetic acid disodium salt dihydrate (EDTA)	Sigma-Aldrich
FastRuler DNA Ladder (Low, Middle, and High Range)	Thermo Scientific™
Formaldehyde solution, 35%	Carl Roth
Halt™ Protease and Phosphatase Inhibitor cocktail	Thermo Scientific™
Hydrochloric acid, 37% (HCl)	VWR International
IGEPAL CA-630 (Nonidet P-40, NP-40)	AppliChem
IPTG	Sigma-Aldrich
Isopropanol	Sigma-Aldrich
Kanamycin sulfate	Sigma-Aldrich
MassRuler DNA Loading Dye (6X)	Thermo Scientific™
Methanol (99.8%)	Honeywell International
Milk powder	Carl Roth
MOPS SDS Running Buffer (20X)	Invitrogen™
NuPAGE Antioxidant (10X)	Invitrogen™
NuPAGE LDS Sample Buffer (4X)	Invitrogen™
NuPAGE Sample Reducing Agent (10X)	Invitrogen™
NuPAGE Transfer Buffer (20X)	Invitrogen™
Polysorbate 20 (Tween 20)	MP Biomedicals
Ponceau S solution	AppliChem
ProSieve™ QuadColor™ Protein Marker	Biozym
Saponin	Sigma-Aldrich
Select yeast extract	Sigma-Aldrich
SOC outgrowth medium	New England Biolabs
Sodium chloride (NaCl)	Sigma-Aldrich
Sodium hydroxide	Sigma-Aldrich
Sodium deoxycholate	Sigma-Aldrich
Sodium dodecyl sulfate	Sigma-Aldrich
Triethylammonium bicarbonate	Thermo Scientific™
Tris-buffered saline (TBS, 20X)	AppliChem
Triton X-100	Sigma-Aldrich
Trizma base	Sigma-Aldrich
Tryptone	Carl Roth
Vectashield® HardSet™ with DAPI	Vector Laboratories
X-Gal	Sigma-Aldrich

Table 17. Consumables used

Consumables	Supplier
Cell culture dish, 35-mm	Thermo Scientific™
Cell culture dish, 10-cm	Greiner Bio-One
Cell culture flask, tissue culture-treated (T25/T75)	Greiner Bio-One
Cell culture plates, 6-well	Greiner Bio-One
Cell culture plates, 24-well	Greiner Bio-One
Cell culture plates, 96-well, white, flat-bottom	Corning
Cell scraper	Starlab
Coverslip, 24 x 50 mm	Th. Geyer
Cryogenic vial	Simport
Eppendorf tubes, 1.5 mL	Eppendorf
Eppendorf tubes, 2.0 mL	Eppendorf
Eppendorf tubes, 5.0 mL	Eppendorf
Luna cell counting slide	Logos Biosystems
Millicell EZ slide, 4-well glass chamber	Merck Millipore
Millicell EZ slide, 8-well glass chamber	Merck Millipore
Nitrocellulose membrane filter paper sandwich (0.45 µM)	Thermo Scientific™
NuPAGE™ 4-12 % Bis-Tris Mini-Protein gels	Invitrogen™
Parafilm Laboratory Film	Bemis
PCR reaction tube (0.2 mL)	Biozym
Petri dish, 10-cm	Starlab
Pierce™ snap-cap spin columns	Thermo Scientific™
Pipette filter tips (10/20 µL, 20 µL, 100 µL, 200 µL, 1000 µL)	Starlab
Polypropylene tubes, 14 mL, round bottom	Corning
Polypropylene tubes, 15 mL, conical bottom	Greiner Bio-One
Polypropylene tubes, 50 mL, conical bottom	Greiner Bio-One
Serological pipette (2 mL, 5 mL, 10 mL, 25 mL, 50 mL)	Greiner Bio-One

Table 18. Equipment used

Equipment	Supplier
Azure c400 gel and Western blot imaging system	Azure
CellGard Class II biological safety cabinet	NuAire
Eppendorf™ centrifuge (5415R/5424/5242R)	Eppendorf
FLUOstar Omega microplate reader	BMG Labtech
GH303 gel electrophoresis tank	Biostep
Heracell™ 240i CO_2 incubator	Thermo Scientific™
Leica TCS SP5 II confocal microscope	Leica Microsystems
Luna automated cell counter	Logos Biosystems
Microwave, 900 & Grill	Severin
Mini Fuge PLUS	Starlab
MR Hei-Standard magnetic stirrer	Heidolph Instruments
Multi-channel pipettes, ErgoOne (100/300 µL)	Starlab
NanoDrop-1000 spectrophotometer	Peqlab Biotechnology
Nikon Eclipse TS100 inverted routine microscope	Nikon
NuWind multi-application centrifuge	NuAire
RCT Basic magnetic stirrer	IKA-Werke
RS-TR 5 tube roller	Phoenix Instrument
RS-VF10 vortex	Phoenix Instrument

PCR thermocyclers (TAdvanced, TPersonal, TProfessional)	Biometra
PipetBoy pipette controller	Integra Biosciences
Pipettes, Eppendorf Research® Plus (2.5/10/20/100/200 µL)	Eppendorf
Power supply, MP-300V	Major Science
Power supply, PowerPac Basic	Bio-Rad
SONOPULS ultrasonic homogenizer	Bandelin
ThermoMixer compact heating block	Eppendorf™
ThermoMixer F1.5 heating block	Eppendorf™
Vortex-Genie 2 vortex mixer	Scientific Industries, Inc.
XCell SureLock™ Mini-Cell	Invitrogen™
XCell™ Blot Module	Invitrogen™

Table 19. Software and programs used

Software/Program	Source
BioRender	BioRender.com
Cytoscape version 3.9.1	Cytoscape
ImageJ 1.53c	US NIH
GlioVis version 0.20	GlioVis (67)
GraphPad Prism 9.3.1	GraphPad
GSEA version 4.2.3	Broad Institute (76,77)
Ingenuity Pathway Analysis version 22.0	Qiagen (78)
Kinase Enrichment Analysis version 3	https://maayanlab.cloud/kea3/ (79)
Leica Application Suite Advanced Fluorescence version 2.7.3.9723	Leica Microsystems
MARS Data Analysis version 3.32	BMG Labtech
Omega version 5.11 R4	BMG Labtech
Perseus version 1.6.14.0	MaxQuant (80)
ProHits-viz	Gingras Lab (81)
R version 4.1.1	R Foundation
R Studio version 2022.02.3+492	RStudio
Robust Inference of Kinase Activity version 2.1.3	https://rokai.io/ (82)
SnapGene version 5.2.1	Insightful Science
Transcriptome Analysis Console version 4.0.2.15	Thermo Scientific™

3 Methods

3.1 Cell Culture

3.1.1 Cell culture maintenance, seeding, and cryopreservation

DK-MG, LN-18, and U-118 cells were maintained in Dulbecco's Modified Eagle Medium (DMEM) with high glucose, GlutaMAX™ and pyruvate (Gibco™) supplemented with 10% Fetal Bovine Serum (FBS; Gibco™) and 1% antibiotic-antimycotic (Gibco™) at 37°C, 5% CO_2. Stably transfected cells were selected and maintained in the same medium further supplemented with 1 µg/mL puromycin (MP Biomedical) or 4 µg/mL blasticidin (US Biological Life Sciences) depending on the antibiotic resistance cassette present in the transfected plasmid.

Cell passaging was performed once cells were 80-90% confluent. To do so, cells were washed with 1X Dulbecco's Phosphate-Buffered Saline (PBS) solution (Gibco™) and trypsinized with the appropriate volume of 1X trypsin (i.e., 1 mL per 25 cm^2) until completely detached. Trypsin was then deactivated by the addition of complete medium. Excess volume was discarded to achieve the desired splitting ratio, and each flask was filled up to the original volume (i.e., 5 mL for 25 cm^2,10 mL for 75 cm^2 flasks) with the appropriate culture medium.

To seed cells, cells were split as previously described. Afterwards, cell pellets were collected by centrifugation at 500 x g for 3 minutes and resuspended in 1 mL of complete maintenance medium. Cell counting was performed by the Luna automated cell counter (Logos Biosystems) on a Luna cell counting slide (Logos Biosystems) containing a 10 µL volume from a 1:2 dilution of the cell resuspension in Trypan blue dye (Sigma Aldrich). Based on the resulting cell count, cells were seeded at the desired densities and into the appropriate culture vessels or well plates.

To cryopreserve cell line stocks, cells were pelleted as described above and resuspended in 500 µL of Synth-a-Freeze™ cryopreservation medium (Gibco™) followed by controlled-rate freezing at -80°C and lastly, storage in liquid nitrogen.

3.1.2 Stable plasmid transfection

Transfection of GBM cells with plasmids was performed using X-tremeGENE™ 9 DNA transfection reagent (Roche). For each transfection, 2 x 10^5 cells were seeded in 2 mL of DMEM maintenance medium in one well of a 6-well plate (Greiner). Once the cells reached 70-80% confluency, cells were treated with the transfection mix containing 2000 ng of plasmid DNA and 6 µL of the transfection reagent in 200 µL of Opti-MEM™ Reduced Serum Medium (Gibco™), previously pre-incubated at room temperature for 15 minutes. Transfected cells were incubated for approximately 72 hours to allow sufficient plasmid expression. Stably transfected cells were selected by continuous treatment of the cells with the appropriate antibiotic-containing medium. Selected cells were then characterized by Western blotting, expanded in cell culture flasks, and cryopreserved as described above.

3.2 Cloning

3.2.1 NEB assembly of BioID2 plasmids

To generate a Gateway™-compatible BioID2 destination vector, the following overlapping DNA fragments were amplified by PCR and assembled using the NEBuilder® HiFi DNA Assembly kit (New England Biolabs):

Table 20. DNA fragments for the generation of the Gateway™-compatible BioID2 destination vector

DNA fragment	Purpose	Template
pMXs-Gateway backbone	Contains the attR1 and attR2 sites that allows subcloning of the bait coding sequence from an entry clone by Gateway™ LR cloning	pMXs-GW-IRES-PuroR (DKFZ Clone Repository)
Myc-Linker	C-terminal Myc tag allows detection of BioID2 fusion proteins; glycine-serine (GS) linker permits proper folding of the BioID2 tag and extension of the biotinylation range	BioID2 plasmid provided by Dr. David Reuss
Linker-BioID2	Fragment contains the C-terminal part of the GS linker that has the same purpose as above; BioID2 tag facilitates biotinylation of proximal proteins	BioID2 plasmid provided by Dr. David Reuss
IRES-PuroR	Internal ribosome entry site (IRES) sequence allows cap-independent translation of the downstream puromycin resistance marker	pMXs-GW-IRES-PuroR (DKFZ Clone Repository)

To perform the assembly, 0.125 pmol of each DNA fragment amplified by PCR were mixed with an equivalent volume of NEBuilder® HiFi DNA Assembly 2X Master Mix and incubated at 50°C for 1 hour. To digest possible contaminating PCR plasmid templates, the reaction was further treated with Anza™ DpnI restriction enzyme (Invitrogen™) for 30 minutes prior to heat-inactivation at 80°C. The reaction was then transformed into One Shot™ *ccd* B Survival™ 2 T1 R competent *E. coli* cells and plasmids were extracted as described below.

3.2.2 Site-directed mutagenesis

To generate mutant constructs, site-directed mutagenesis by inverse PCR (SDM-PCR) was performed. Briefly, overlapping mutagenic primers were designed and used in standard PCR reactions to inversely amplify the plasmid to be mutated. Cycling parameters used for PCR are indicated in the table below. After plasmid amplification, template plasmids were subsequently digested out by standard DpnI digest as described above, and the template-free PCR reactions were then transformed into chemically competent TOP10 *E. coli* cells. Proper mutagenesis was confirmed by sequencing after standard plasmid extraction.

Table 21. Cycling parameters for inverse PCR-based site-directed mutagenesis

Step	Temperature	Time	Cycles
Initial denaturation	98°C	30 sec	-
Denaturation	98°C	10 sec	30X
Annealing	Primer-dependent*	30 sec	
Extension	72°C	Product size-dependent**	
Final Extension	72°C	2 min	-

Notes:
**Annealing temperatures predicted by SnapGene version 5.2.1 were used*
***Extension times were selected to approximate 30 seconds for every 1000 bp of the product*

3.2.3 Gateway cloning

Gateway™ cloning was routinely performed to clone coding sequences into the desired Gateway™ destination vector. Briefly, entry clones were first generated via Gateway™ BP reactions by mixing 150 ng of the PCR-amplified coding sequence (following cycling parameters defined above) with 150 ng of pDONR201 and 2 µL of Gateway™ BP clonase™ II enzyme mix (Invitrogen™). After overnight incubation at room temperature, the reaction was deactivated by the addition of 1 µL Proteinase K (20 mg/mL) and incubated at 37°C for 10 minutes. Subsequently, the BP reaction was transformed into chemically competent TOP10 or DH5α *E. coli* and plasmid DNA extraction was performed as described below.

To generate the desired mammalian expression vectors, 150 ng of the entry clone and 150 ng of the destination vector were mixed with 2 µL of Gateway™ LR clonase™ II enzyme mix (Invitrogen™). Overnight incubation, Proteinase K treatment, transformation, and plasmid extraction were then performed as described above.

3.2.4 Transformation

To propagate existing plasmids or cloning reactions generated by NEB assembly, SDM-PCR, or Gateway™ cloning, standard heat-stock transformation of the appropriate strain of chemically competent *E. coli* was performed. Briefly, *E. coli* were thawed on ice for 10 minutes followed by the addition of 1-5 µL of plasmid DNA for each transformation reaction. After incubation on ice for 20 minutes, transformation was performed by incubating the bacteria at 42°C for 1 minute and then on ice for another minute. Afterwards, 250 µL of SOC outgrowth medium was added, and the bacteria was then incubated at 37°C for 45 minutes to 1 hour while shaking at 250 rpm. Plating was then performed on Luria-Bertani (LB) agar plates (1% tryptone, 0.5% yeast extract, 1% NaCl, 1.5% agar) containing the appropriate antibiotic(s). After overnight (i.e., 16-18 hr) incubation at 37°C, single colonies growing on the plates were picked and inoculated into 5 mL of LB medium (1% tryptone, 0.5% yeast extract, 1% NaCl) containing the appropriate antibiotic(s). Starter cultures were prepared in 14 mL round-bottom polypropylene tubes (Corning) then grown overnight and plasmid DNA extraction was performed the next day.

Table 22. Summary of transformation parameters

Cloning Reaction	End Product	Backbone	Strain	Antibiotic
Re-transformation	N/A	Plasmid-dependent		
SDM-PCR	Mutated constructs	pDONR201	TOP10	50 µg/mL kanamycin
BP reaction	Entry clone	pDONR201	TOP10	50 µg/mL kanamycin
LR reaction	Expression clone	pMXs	NEB 5α	100 µg/mL ampicillin
NEB assembly	Destination vectors	pMXs	*ccd* B Survival	34 µg/mL chloramphenicol + 100 µg/mL ampicillin

3.2.5 Plasmid DNA extraction

Plasmids were extracted from bacterial starter cultures using the NucleoSpin™ Plasmid kit (Macherey-Nagel) following the manufacturer's protocol. Briefly, bacteria were pelleted by centrifugation at 11,000 x g for 30 seconds, followed by resuspension in 250 µL of A1 resuspension buffer (Macherey-Nagel) supplemented with 400 µg/mL RNAse. Bacterial cells were then lysed by the addition of an equivalent volume of A2 lysis buffer (Macherey-Nagel) followed by incubation at room temperature for 5 minutes. Lysis was stopped with the addition of 300 µL of A3 neutralization buffer (Macherey-Nagel), and the solution was centrifuged at 11,000 x g for 5 minutes twice. The supernatant was then loaded into the columns provided in the kit, washed once with 500 µL of AW wash buffer (Macherey-Nagel) followed by 600 µL of A4 wash buffer (Macherey-Nagel). Columns were then dried by centrifugation at 11,000 x g for 2 minutes. Afterwards, 50 µL of elution buffer were added into the columns, which were then incubated at 70°C for 2 minutes. Elution was performed by centrifugation at 11,000 x g for 1 minute. Plasmid concentrations were then measured via Nanodrop, and plasmids were stored at -20°C for long-term storage.

3.2.6 Restriction enzyme analysis

To test whether the correct plasmids were successfully generated after every plasmid extraction procedure, plasmids were subjected to restriction enzyme (RE) digests. For Gateway™-compatible plasmids, RE digests were performed by mixing 200 ng of plasmid DNA with 1 µL Anza™ Bsp1407I (Invitrogen™) in a 10 µL reaction volume containing 1X Anza™ Buffer (Invitrogen™). Alternatively, Anza™ EcoRI (Invitrogen™) was used when digesting TA-cloned inserts in pGEM®-T Easy (Promega) backbones. Test digests were then incubated at 37°C for 30 minutes, then loaded into a 1% agarose gel composed of 1X Tris-borate-EDTA (TBE) buffer (89 mM Tris base, 89 mM boric acid, 2 mM EDTA) and pre-stained with ethidium bromide. Gels were then run at a constant voltage of 125 V for 40 minutes and imaged using the Azure c400 Gel Imaging System (Azure Biosystems). Properly digested plasmids resulting from BP, SDM-PCR, or NEBuilder® cloning reactions were then further sent for Sanger sequencing at Genewiz GmbH (Leipzig, Germany) for sequence verification.

3.3 Validation of CRISPR/Cas9-EMP3 knockout GBM cells

CRISPR/Cas9-edited EMP3 knockout (KO) DK-MG, LN-18, and U-118 cells and their corresponding controls were obtained from Dr. Arne Christians (Hannover Medical School, Hannover, Germany). To verify proper CRISPR/Cas9-mediated deletion of EMP3, Sanger sequencing of the targeted genomic region was performed. Briefly, genomic DNA (gDNA) was extracted from the cell lines using the Nucleospin Tissue kit (Macherey-Nagel). The targeted region was then PCR-amplified using the gDNA as template and the following primers: 5'-TTAGCTCTACCTCCGATGCC-3', 5'-CGCCCACTCCAACTTTGTT-3'. The resulting PCR products were TA-cloned using the pGEM®-T Easy Vector Systems kit (Promega) following the manufacturer's protocol. Following standard transformation and blue/white selection using LB plates supplemented with 0.5 mM IPTG and 80 µg/mL X-Gal, plasmids were further propagated and extracted as described above. After performing RE digests as described above, plasmids were then sent to Eurofins Genomics (Ebersberg, Germany) for sequencing. Results were analyzed in SnapGene version 5.2.1. To validate EMP3 KO at the protein level, lysates were collected from the cell lines and Western blotting was performed as described below.

3.4 Western blotting

3.4.1 Lysate collection and BCA assay

Total cell lysates were collected by scraping cells previously washed in 1X PBS with ice-cold NP-40 lysis buffer (50 mM Tris-HCl, pH 7.8, 150 mM NaCl, 1 mM EDTA, and 0.2% NP-40) supplemented with 1X Halt™ Protease and Phosphatase Inhibitor cocktail (Thermo Scientific™). Lysates were then snap-frozen in liquid nitrogen and thawed thrice, followed by centrifugation at 20,000 x g for 5 minutes. The clarified supernatants were then collected, and protein concentrations were measured using the Pierce™ bicinchoninic assay (BCA) kit (Thermo Scientific™) following the manufacturer's instructions. Absorbance at 562 nm were then measured using the FLUOstar Omega microplate reader (BMG Labtech) and the Omega version 5.11 R4 software (BMG Labtech). Actual protein concentrations were calculated by a four-parameter fit algorithm from the MARS data analysis software version 3.32 (BMG Labtech).

3.4.2 SDS-PAGE, immunoblotting, and imaging

To prepare samples for sodium dodecyl sulfate-polyacrylamide gel electrophoresis (SDS-PAGE), equivalent amounts of lysates within the range of 10-20 µg were mixed in 20 µL volumes containing 1X NuPAGE™ LDS Sample Buffer (Invitrogen™) and 1X NuPAGE™ Sample Reducing Agent (Invitrogen™). Lysates were subsequently heated at 95°C for 5 minutes, cooled to 4°C for 1 minute, and finally loaded into each well of a NuPAGE™ 4-12% Bis-Tris gel (Invitrogen™) in 1X NuPAGE™ MOPS SDS running buffer (Invitrogen™). Protein separation by size was then achieved by running the gels at a constant voltage of 200 V for 1 hour.

After SDS-PAGE, proteins were transferred onto a Pierce™ 0.45 µm nitrocellulose membrane (Thermo Scientific™) using the XCell II™ Blot Module (Invitrogen™) at 30 V, 170 mA constant, for 90 minutes. Successful transfer was monitored by incubating the membrane in Ponceau stain (Applichem) followed by destaining with demineralized H_2O. Membranes were then washed with 1X TBS-T (1X Tris-buffered saline, 0.05% Tween 20, pH 7.6) and blocked for 1 hour with 5% milk in 1X TBS-T. Membranes were then incubated with primary antibodies at the appropriate dilutions in blocking buffer overnight. The next day, membranes were washed thrice with 1X TBS-T for 5 minutes per wash (i.e., TBS-T wash) and incubated with the appropriate secondary antibodies in blocking buffer for 1 hour. After another round of TBS-T wash, membranes were developed using the WesternBright Sirius Chemiluminescent Detection Kit (Advansta) and imaged using the chemiluminescence module of the Azure c400 Gel Imaging System (Azure Biosystems).

Band intensities were quantified using ImageJ 1.53c. Briefly, band intensities of proteins of interest were measured and normalized to the corresponding β-actin band intensities. Normalized band intensities were then recalibrated using the experimental control as reference. Values were then log_2-transformed, and statistical analysis was performed using GraphPad Prism 9.3.1.

3.4.3 Measurement of EGFR degradation and activation kinetics

To measure EGFR degradation and activation kinetics by Western blotting, GBM cells were first seeded into five 35-mm cell culture dishes (Thermo Scientific™) at a density of 2.0×10^5 cells in 2 mL of DMEM maintenance medium per dish. Cells were then incubated overnight at 37°C, 5% CO_2. Afterwards, cells were serum-starved by replacing spent media with 2 mL of

DMEM with 1% antibiotic-antimycotic but without 10% FBS. Serum-starved cells were incubated overnight at 37°C, 5% CO_2. The next day, cells were pre-treated with 100 µg/mL of cycloheximide for 1 hour to prevent nascent protein synthesis. Afterwards, cells were treated with 100 ng/mL epidermal growth factor (EGF) and incubated until lysate collection was performed at the desired time points (i.e., from 30 to 120 min after EGF treatment, with 30-minute intervals). Untreated cells were used as control and designated as time point t = 0. Lysates were stored in -80°C until Western blot was performed following the procedures outlined above.

3.5 Immunofluorescence

GBM cells were seeded at a density of 1 x 10^4 cells/mL of DMEM maintenance media in 4- or 8-well chamber slides (Merck Millipore) and incubated at 37°C, 5% CO_2 for 72 hours or until a confluency of ~80% was reached. To perform immunostaining, cells were first washed once with 1X PBS and then fixed with 4% formaldehyde in 1X PBS at room temperature for 15 minutes. Each well was then washed with 1X PBS for 5 minutes thrice, and fixed cells were blocked with 0.1% saponin, 5% FBS in 1X PBS under gentle shaking at room temperature for 1 hour. Cells were then incubated with the primary antibodies at the appropriate dilutions in blocking buffer at 4°C overnight. The next day, the primary antibody solution was discarded, and cells were washed again thrice in 1X PBS. Afterwards, primary antibody-stained cells were incubated at room temperature in the dark with the appropriate secondary antibodies diluted in blocking buffer. After three washes with 1X PBS, slides were dried and mounted using Vectashield® HardSet™ with DAPI (Vector Laboratories). Images were then captured at 63X magnification and 16-bit resolution using the Leica Application Suite Advanced Fluorescence software (version 2.7.3.9723) and the appropriate laser lines and filters.

3.6 BioID2-based proximity labeling

3.6.1 Induction of biotinylation and streptavidin-pull down

A total of 1 x 10^6 LN-18 or U-118 cells stably transfected with BioID2 bait constructs were seeded in triplicates in 10-cm dishes (Greiner) containing 10 mL of DMEM maintenance medium supplemented with 1 µg/mL puromycin. Cells were incubated for 48-72 hours until ~80% confluency was reached. To induce biotinylation, spent media was discarded and replaced with 10 mL of the same media additionally supplemented with 50 µM biotin. After

incubation at 37°C for 18 hours, cells were lysed and protein concentrations measured following the standard lysate collection protocol described in section 3.4.

To verify BioID2-induced biotinylation, streptavidin-HRP blots were performed on the collected input lysates. For streptavidin-HRP blots, 20 µg input material were loaded and run in SDS-PAGE gels and subsequently blotted onto nitrocellulose membranes following the standard Western blot protocol described above. After blocking, membranes were incubated with a 1:2000 dilution streptavidin-HRP (Cell Signaling Technology®) in 5% milk in TBS-T under gentle shaking at room temperature for 1 hour. Membranes were then developed using the WesternBright Sirius Chemiluminescent Detection Kit (Advansta) and imaged using the chemiluminescence module of the Azure c400 Gel Imaging System (Azure Biosystems).

To purify biotinylated proteins, streptavidin pull-downs were performed. Briefly, 1 mL Pierce™ snap-cap spin columns (Thermo Scientific™) containing a polyethylene filter with 30 µM-wide pores were washed with 200 µL of 1X PBS and subsequently packed with 100 µL of Pierce™ High Capacity Streptavidin Agarose Resin slurry (Thermo Scientific™), which is equivalent to 50 µL of the agarose resin. The loaded columns were then centrifuged at 500 x g for 1 minute to remove the storage solution. After washing with 250 µL of 1X PBS thrice, a total of 1 mg of each lysate at 2 mg/mL concentrations were loaded into each column. Columns were then incubated at room temperature for 30 minutes with end-over-end mixing. To remove unbound proteins, the columns were then centrifuged at 500 x g for 1 minute and washed with 250 µL of 1X PBS for four times. Biotinylated proteins were then eluted at 95°C for 5 minutes with Pierce™ Lane Marker Non-Reducing Sample Buffer (Thermo Scientific™) diluted to 2X concentration (i.e., 0.12 M Tris-HCl, 2% SDS, 20% glycerol, 2X lane marker tracking dye, pH 6.8) and additionally supplemented with 2 mM biotin. Eluates were collected by centrifugation at 1000 x g for 1 minute.

To confirm successful purification, Coomassie staining was performed on the eluates. Briefly, 20 µL of the lysates were loaded into SDS-PAGE gels, and protein separation was performed using standard SDS-PAGE settings. Afterwards, gels were washed thrice in distilled H_2O and incubated overnight in Coomassie Brilliant Blue G250 staining solution (Sigma-Aldrich). After three washes in distilled H_2O, gels were imaged using the visible light module of the Azure c400 Gel Imaging System (Azure Biosystems). Upon confirmation of successful purification, eluates were submitted and subjected to label-free quantitative mass spectrometry (MS) analysis by the MS-based Protein Analysis Unit of the DKFZ (Heidelberg, Germany).

3.6.2 Statistical analysis and network visualization of BioID2 MS data

MaxQuant output files provided by the MS-based Protein Analysis Unit were further statistically analyzed using Perseus (version 1.6.14.0). Briefly, potential contaminants and proteins that were not quantified in at least one experimental replicate of one condition were filtered out of the matrix. The remaining label-free quantification (LFQ) intensities were then $\log_2$-transformed and a two-sample, two-sided Welch's t-test was performed for each pairwise comparison between an EMP3 bait (WT or N47A) and a spatial reference control (TagRFP or GAP-TagRFP). Proteins that were significantly enriched in the EMP3 WT and N47A pull-downs relative to the controls were then identified by filtering for 1) proteins with a difference in $\log_2$(LFQ) between bait and control ≥ 1 and p-value ≤ 0.05, as well as 2) proteins that were uniquely interacting with either EMP3 bait (i.e., LFQ ≥ 0 for all replicates of the EMP3 bait of interest and LFQ = 0 for all replicates of the spatial reference control). To visualize results in volcano plots, the R package EnhancedVolcano was used.

To map the resulting proteins into a PPI network, protein lists were submitted to STRING (version 11.5). The resulting networks were exported in Cytoscape (version 3.9.1), where additional filtering for high-confidence edges corresponding to STRING scores > 0.700 and nodes with degrees ≥ 3 was performed. Enrichment analysis was performed using the enrichment analysis plug-in available in the stringAPP (version 1.7.1). Nodes were colored and clustered according to the functional groups or signaling pathways defined by Gene Ontology (GO), Kyoto Encyclopedia of Genes and Genomes (KEGG), Reactome, and WikiPathways terms. Furthermore, plasma membrane localization scores based on the COMPARTMENTS database were continuously mapped onto the node edges. Additional visualization of enrichment results in the form of dot plots was also performed using ProHits-viz (81).

3.7 Phosphoproteomics analysis

3.7.1 Lysate preparation for phosphopeptide enrichment

A total of 1 x 10^6 control or EMP3 KO GBM cells were seeded in triplicates in 10 mL of DMEM maintenance medium and further incubated at 37°C, 5% CO_2 for 72 hours. Total cell lysates for phosphopeptide enrichment were then prepared by lysing the cells in 100 mM triethylammonium bicarbonate (TEAB) lysis buffer with 1% SDS, 1% sodium deoxycholate (SDC), and protease and phosphatase inhibitors. Lysates were heated at 95°C for 5 minutes to

further deactivate proteases and phosphatases. Afterwards, sonication was performed for 5 cycles (35% power for 20 seconds per cycle) using the SONOPULS ultrasonic homogenizer (Bandelin) and lysates were centrifuged at 20,000 x g at 4°C for 10 minutes. The resulting supernatants were then submitted to the MS-based Protein Analysis Unit (Heidelberg, Germany) for phosphopeptide enrichment and MS analysis.

3.7.2 Statistical and kinase enrichment analysis of MS data

MaxQuant output files provided by the MS-based Protein Analysis Unit were further statistically analyzed using Perseus (version 1.6.14.0). First, LFQ intensities were log_2-transformed. Potential contaminants, along with phosphosites containing invalid values in more than 2 replicates for each condition (i.e., control or EMP3 KO) and phosphosites with localization probabilities < 0.75 were filtered out. Imputation for missing values was then performed for each replicate using values from a normal distribution (width = 0.3, down shift = 1.8). Within each cell line, log_2(LFQ) values of control and EMP3 KO cells were statistically compared using a two-sample, two-sided Welch's t-test. Phosphosites with absolute log_2-fold changes (FCs) ≥ 1 and false discovery rate (FDR)-adjusted p-values ≤ 0.05 were deemed to be differentially phosphorylated between EMP3 KOs and controls.

Phosphorylation analysis was then performed in Ingenuity Pathway Analysis (IPA) version 22.0 (Qiagen), using the list of differentially phosphorylated proteins and their corresponding phosphosite log_2-FCs as input. Default IPA parameters were used for the analysis, with the exception of the Species parameter which was restricted to "Human" only. In parallel, the same analysis was performed using proteins with commonly regulated phosphosites between DK-MG and U-118 EMP3 KO cells as input. For kinase enrichment analysis (KEA), upstream kinases regulating proteins with common dephosphorylation sites were identified by inputting the said protein list into KEA version 3 (https://maayanlab.cloud/kea3/, accessed 02 July 2022) (79). For Robust Inference of Kinase Activity (82), kinase activities of upstream kinases putatively regulating commonly regulated phosphosites in DK-MG and U-118 EMP3 KOs were predicted by RoKAI version 2.1.3 (https://rokai.io/, accessed 02 July 2022) using UniProt IDs, phosphosites, and their corresponding log_2-FCs as input. For visualization of results, the R packages ggplot2 and EnhancedVolcano were used.

3.8 Gene expression profiling

3.8.1 RNA extraction and identification of differentially expressed genes

GBM cells were seeded in triplicates at a density of 2 x 10^5 cells per well in 2 mL of DMEM maintenance medium and incubated at 37°C, 5% CO_2 for 72 hours. Total RNA were extracted from the cells using the Nucleospin RNA kit (Macherey-Nagel) following the manufacturer's instructions. Samples were sent to the Microarray Unit of the DKFZ Genomics and Proteomics Core Facility (GPCF; Heidelberg, Germany) for microarray analysis using the Human Clariom S assay (Applied Biosystems).

To identify differentially expressed genes (DEGs) between two groups (e.g. control vs. EMP3 KO), raw .CEL files were imported into the Transcriptome Analysis Console software version 4.0.2.15 (Thermo Fisher Scientific). DEGs lists were then prepared by filtering for genes with an absolute $\log_2$-fold change ≥ 2 and FDR-adjusted p-value ≤ 0.05.

3.8.2 Ingenuity Pathway Analysis (IPA)

To identify master regulators (MRs) that can account for the identified DEGs, upstream pathway analysis was performed using IPA version 22.0 (IPA, Qiagen). For each comparison (e.g. control vs. EMP3 KO), core analysis was performed using the DEGs as input. Default IPA settings were retained, except the Species parameter (i.e., restricted to "Human" only).

3.8.3 Gene Set Enrichment Analysis (GSEA)

To identify which gene sets are enriched in control or EMP3 KO cells, DEGs and their $\log_2$-transformed expression levels were imported into the GSEA version 4.2.3 (Broad Institute). Normalized enrichment scores (NES) and FDR-adjusted p-values were calculated for C2 gene sets (c2.all.v7.5.1.symbols.gmt [Curated]) that contained 15-500 of the DEGs.

3.9 Cell surface proteome analysis

3.9.1 Biotinylation and isolation of cell surface proteins

A total of 1 x 10^6 LN-18 control or EMP3 KO cells were seeded in 10-cm dishes (Greiner) containing 10 mL of DMEM maintenance medium and incubated at 37°C, 5% CO_2 for 72 hours. Afterwards, spent media was discarded and cells were washed with 5 mL of 1X PBS. Biotin labeling of cell surface proteins was then performed by incubating the cells with 5 mL

of 1X (i.e., 250 µg/mL in 1X PBS) EZ-Link™ Sulfo-NHS-SS-Biotin (Thermo Scientific™) for 10 minutes at room temperature. The labeling solution was then removed and cells were washed thrice with ice-cold TBS. Cell lysis was then performed with 500 µL NP-40 lysis buffer as described above.

To purify biotin-labeled proteins, NeutrAvidin pull-downs were performed using the Pierce™ Cell Surface Biotinylation and Isolation Kit. Briefly, spin columns were loaded with 100 µL of the NeutrAvidin agarose slurry (equivalent to 50 µL resin) and centrifuged at 1000 x g for 1 minute to discard the storage solution. Afterwards, 1 mg of each lysate at 2 mg/mL concentrations were loaded onto the resin and the columns were incubated at room temperature for 30 minutes with end-over-end mixing. Unbound proteins were then removed by centrifugation at 1000 x g for 1 minute, and the columns were subsequently washed with 200 µL of wash buffer four times. Elution was performed by incubating the columns with 100 µL of the elution buffer supplemented with 10 mM dithiothreitol (DTT) at room temperature for 30 minutes with end-over-end mixing. Eluates were collected by centrifugation at 1000 x g for 2 minutes and submitted to the MS-based Protein Analysis Unit (Heidelberg, Germany).

3.9.2 Statistical analysis of cell surface proteome data

MaxQuant output files provided by the MS-based Protein Analysis Unit were statistically analyzed using Perseus (version 1.6.14.0). LFQ intensities were $\log_2$-transformed. Potential contaminants and proteins with invalid values in more than 2 replicates for each condition were filtered out. Missing values within each replicate were imputed using values from a normal distribution (width = 0.3, down shift = 1.8). Statistical analysis was then performed using a two-sample, two-sided Welch's t-test. Proteins with absolute $\log_2$-FCs ≥ 0.50 and p-values ≤ 0.05 were deemed to be differentially phosphorylated between EMP3 KOs and controls. Non-membrane proteins (i.e., plasma membrane COMPARTMENTS score < 4) were considered as non-specific and were further filtered out. To visualize results in volcano plots, the R package EnhancedVolcano was used.

3.10 FLAG co-immunoprecipitations

3.10.1 FLAG pull-downs

A total of 1 x 10^6 LN-18 or U-118 cells stably transfected with FLAG-tagged bait constructs were seeded in 10-cm dishes (Greiner) containing 10 mL of DMEM maintenance medium.

Cells were incubated at 37°C, 5% CO_2 for 48-72 hours until ~80% confluency is reached. Afterwards, spent media was discarded and cells were washed with 1X PBS and further lysed with 500 µL NP-40 lysis buffer as described above. To immunoprecipitate FLAG-tagged proteins, 1 mg of each lysate (at 2 mg/mL concentration) was loaded into a spin column containing 25 µL of the Pierce™ FLAG Affinity Resin (Thermo Scientific™). Columns were then subjected to end-over-end mixing for 30 minutes at room temperature. Afterwards, the columns were washed thrice with 250 µL with 1X PBS followed by one washing step with 250 µL purified water. Proteins were then eluted by heating the columns with 100 µL 2X non-reducing lane marker sample buffer (0.12 M Tris-HCl, 2% SDS, 20% glycerol, 2X lane marker tracking dye, pH 6.8) at 95°C for 5 minutes followed by centrifugation at 1,000 x g for 1 minute. To detect FLAG-tagged proteins and co-purifying proteins, eluates were subjected to standard Western blotting procedures.

3.10.2 Affinity purification-mass spectrometry (AP-MS) analysis

A total of 1 x 10^6 LN-18 cells stably transfected with FLAG-tagged EMP3, EMP3 N47A, and TagRFP were seeded in 10-cm dishes (Greiner) containing 10 mL of DMEM maintenance medium. Cells were incubated at 37°C, 5% CO_2 for 72 hours. FLAG pull-down was performed as described above. Eluates were then submitted to the MS-based Protein Analysis Unit (Heidelberg, Germany). MaxQuant output files provided by the core facility were further filtered using Perseus (version 1.6.14.0). Briefly, potential contaminants were filtered out, and only proteins with valid values in all conditions of each pairwise comparison (e.g., EMP3 WT vs. TagRFP, EMP3 N47A vs. TagRFP) were retained. LFQ values were $\log_2$-transformed, and proteins with $\log_2\text{-FC} \geq 1$ were identified and plotted on a condition-condition scatter plot using ProHits-viz (81)

3.11 Proximity ligation assay (PLA)

PLAs were performed using the NaveniFlexMR PLA kit (Navinci). First, GBM cells were seeded in 8-well chamber slides (Merck Millipore) at a density of 1 x 10^4 cells in 250 µL DMEM maintenance media per well and incubated at 37°C, 5% CO_2 for 72 hours. To perform PLA, cells were then fixed with 4% formaldehyde at room temperature with gentle shaking for 15 minutes. Cells were then washed with PBS for 5 minutes thrice; afterwards, permeabilization with 0.1% Triton-X in PBS was performed for 10 mins. After another round of PBS washes, cells were incubated in blocking buffer at 37°C for 1 hour. Cells were then

incubated with the appropriate primary antibodies overnight at 4°C. On the second day, cells were washed thrice with 1X TBS-T for 5 minutes, and then incubated with anti-mouse and anti-rabbit Navenibodies (Navinci) at 37°C for 1 hour. Afterwards, a series of three enzymatic reactions were carried out by incubating the cells in the appropriate enzyme-buffer mix at 37°C for the following durations: Reaction A, 1 hour; Reaction B, 30 mins; Reaction C, 90 mins (in the dark). After the last reaction, cells were washed in 1X TBS for 10 minutes twice, then washed with 0.1X TBS for 15 minutes. After discarding the TBS buffer, slides were dried, mounted with VectaShield® HardSet™ with DAPI (Vector Laboratories), and covered with coverslips. Images were captured at 63X magnification and 16-bit resolution using the Leica Application Suite Advanced Fluorescence software (version 2.7.3.9723) and the appropriate laser lines and filters. To quantify PLA signals, an in-house ImageJ script provided by the DKFZ Light Microscopy Facility was used. Briefly, the number of punctate PLA signals per field were measured and normalized to the nuclei count for that field. A total of ten randomly imaged fields were quantified per sample, and results across three independent trials were averaged, statistically analyzed, and visualized using GraphPad Prism version 9.3.1.

3.12 CellTiter-Glo® assay

For the measurement of proliferation rates of control and EMP3 KO cells, 2 x 10^3 cells were seeded in 100 µL of DMEM maintenance medium into each well of a white, flat-bottom 96-well plate (Corning). Five identical plates were prepared, each corresponding to a CellTiter-Glo® measurement starting from Day 0 to Day 4 after seeding. Cells were then incubated at 37°C, 5% CO_2 until the day of measurement. To measure response to osimertinib treatment, cells were likewise seeded at the same seeding density and into the same 96-well plates. After a one-day incubation at 37°C, 5% CO_2, cells were treated with varying concentrations of osimertinib (i.e., two-fold serial dilutions starting from 10 µM to 1.25 µM plus 0 µM or dimethyl sulfoxide (DMSO) only as the negative control) and further incubated for 24 hours. To perform the CellTiter-Glo® assay, 100 µL of Cell-Titer-Glo® 3D (Promega) were added into each well. Plates then were subjected to shaking at 300 rpm for 2 minutes; afterwards, luminescence signals corresponding to adenosine triphosphate (ATP) levels were measured using the FLUOstar Omega microplate reader (BMG Labtech) and Omega version 5.11 R4 (BMG Labtech). Relative luminescence units (RLU) were determined after normalization to control cells, and results were plotted and statistically analyzed in GraphPad Prism version 9.3.1.

To measure proliferation rates in response to EGFR, CD44, and MET ligands, a total of 1 x 10^4 control or EMP3 KO cells were first seeded in 500 µL of DMEM maintenance medium into each well of a 24-well plate (Greiner). After a one-day incubation at 37°C, 5% CO_2, cells were serum-starved by replacing the spent media with DMEM with 1% antibiotic-antimycotic but without 10% FBS. Cells were incubated at 37°C, 5% CO_2 for another day. Afterwards, serum-starved cells were treated with 100 ng/mL EGF (Peprotech), 100 µg/mL hyaluronic acid (HA; MW: 500-750 kDa; Sigma-Aldrich), or 100 ng/mL hepatocyte growth factor (HGF) daily for three consecutive days. Cells were incubated for another day after the last day of ligand treatment. CellTiter-Glo® assays were then performed as previously described, keeping the 1:1 volume/volume ratio between the wells and the CellTiter-Glo® reagent.

3.13 Caspase-Glo® 3/7 assay

To measure caspase 3/7 levels in response to osimertinib treatment, a total of 1 x 10^4 control or EMP3 KO cells were first seeded in 100 µL of DMEM maintenance medium into each well of a white, flat-bottom 96-well plate (Corning). After a one-day incubation at 37°C, 5% CO_2, cells were treated with 0 (i.e., DMSO only) or 2.5 µM osimertinib and incubated for another 24 hours. Caspase 3/7 levels were measured using the Caspase-Glo® 3/7 Assay System (Promega). To do so, 100 µL of the Caspase 3/7 reagent were added into each well. Plates were then subjected to shaking at 500 rpm for 30 seconds, followed by a 30-minute incubation at room temperature. Luminescence signals corresponding to caspase 3/7 levels were then measured using the FLUOstar Omega microplate reader (BMG Labtech) and Omega version 5.11 R4 (BMG Labtech). RLUs corresponding to fold-changes in caspase 3/7 activity were measured after normalization to untreated cells, and results were plotted and statistically analyzed in GraphPad Prism version 9.3.1.

3.14 Statistical analysis

Statistical analyses of all MS data were performed in Perseus version 1.6.14.0. For each pairwise comparison, a two-sample, two-sided Welch's t-test was applied. All other statistical analyses were performed in GraphPad Prism version 9.3.1. Unpaired t-test was applied when the comparison was made between two groups with equal variances. Welch's t-test was applied if the comparison was made between two groups with unequal variances. Welch's ANOVA with Dunnett's T3 multiple comparisons test was applied when comparing more than two groups with unequal variances.

3.15 Data wrangling and visualization in R

Data wrangling and visualization were additionally performed using R version 4.1.1 and R Studio version 2022.02.3+492. The following R packages were used: dplyr, EnhancedVolcano, ggplot2, ggVennDiagram, RcolorBrewer, and tidyverse. R scripts were custom-made for each application.

4 Results

4.1 Establishment of a BioID2-based proximity labeling method

To comprehensively define EMP3's interactome in an unbiased manner, this study applied BioID2-based proximity labeling on two glioblastoma cell lines, LN-18 and U-118. This method relies on the ability of a promiscuous biotin ligase derived from *Aquifex aeolicus* to biotinylate neighboring proteins (i.e., within ~10 nm radial distance) (83). When fused to a protein of interest (POI), BioID2 can in principle biotinylate other proteins that interact with or reside in proximity to the POI. Biotinylated proteins can then be purified by classical streptavidin pull-downs and quantitatively identified with mass spectrometry (MS) analysis (Fig. 8A). Because the labeling times for BioID2 range from 16-24 hours, the method can potentially generate a historical record of all PPIs of the bait protein. Moreover, the method is well-suited for detecting weak or transient PPIs, which is particularly relevant for proteins like EMP3, a putative moonlighting protein that likely functions within or shuttles between multiple subcellular contexts.

To establish the method, a Gateway destination vector encoding a C-terminal Myc-Linker-BioID2 fusion tag followed by a puromycin resistance cassette under a control of an IRES (internal ribosome entry site) element was first generated by DNA assembly (Fig. 8B). The Myc tag was included as a detectable epitope for the purposes of validating bait expression and localization via immunoblotting and immunofluorescence. Meanwhile, the 25-nm glycine-serine (GS) linker was incorporated to increase the flexibility and biotinylation range of the BioID2 tag. Subsequently, the coding sequences of the wild-type and N47A mutant versions of EMP3 were subcloned into the resulting destination vector. As spatial reference controls, TagRFP and a GAP-TagRFP (i.e., TagRFP containing an N-terminal membrane-localizing tag derived from neuromodulin or GAP43) were subcloned into the same destination vector. These two spatial reference controls were included to account for both membrane and cytosolic interactors of EMP3, given that EMP3 is known to shuttle between the two subcellular locations (Fig. 8C). After successful cloning, the bait constructs were introduced into LN-18 and U-118 cells by lipofection, and stably transfected cell lines were selected by and expanded under continuous puromycin treatment.

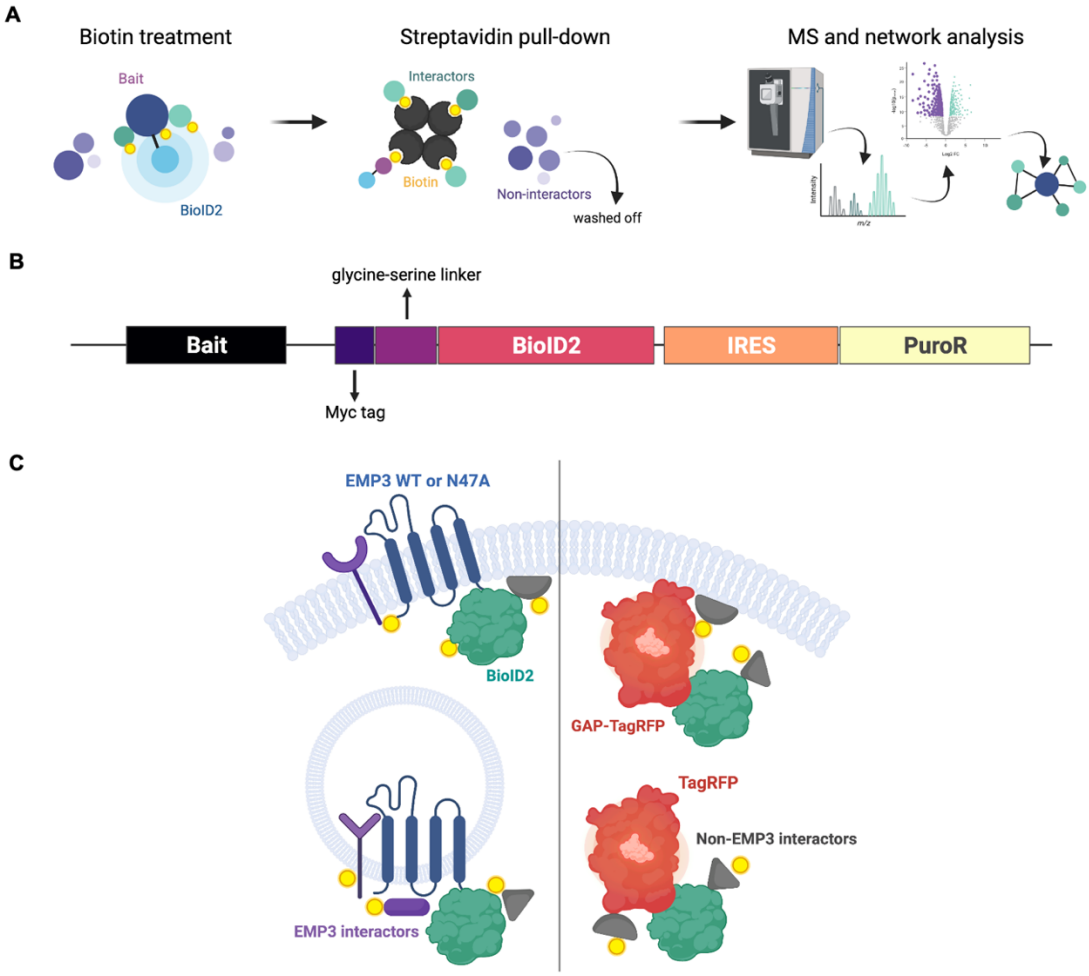

Figure 8. Experimental design of the BioID2-based proximity labeling experiment. A) BioID2 experimental workflow. BioID2 baits are expressed in living cells, which are then treated with biotin to induce biotinylation of proteins within close proximity (~10 nm) of the fusion protein. Biotinylated proteins are then purified by streptavidin pull-downs and subsequently quantified and analyzed by MS analysis. B) Generic partial plasmid map of fusion constructs generated in this study. C) Experimental design of the BioID2 experiment. EMP3 WT and N47A-Myc-Linker-BioID2 proteins were used as baits, while TagRFP and GAP-TagRFP were used as spatial reference controls. Figure was created using BioRender.com.

A reliable BioID2 screen requires the proper expression and subcellular targeting of the fusion proteins. To confirm proper fusion protein expression, immunoblotting for the Myc tag was performed using total cell lysates extracted from LN-18 and U-118 cells stably transfected with the BioID2 constructs. Prior to Western blotting, EMP3 WT lysates were pre-treated with PNGase F to remove glycosylation marks and facilitate chemiluminescent detection. Total cell lysates from untransfected LN-18 and U-118 cells were used as negative controls. Results showed proper expression of the Myc tag in stably transfected cells but not in untransfected controls (Fig. 9). Moreover, no apparent fusion protein cleavage was detected, indicating that the fusion proteins are intact within the GBM cells. Meanwhile, immunostaining results show that the Myc signal produced by the wild-type and mutant versions of the EMP3 bait both localized in the membrane and within certain cytosolic compartments, consistent with the

localization annotations of EMP3 in the HPA (Fig. 10). The Myc signal also largely overlapped with EMP3 immunostaining. No protein cleavage was detected in the blots, suggesting that the few areas without co-localizing Myc and EMP3 signals can be attributed to the presence of endogenous EMP3. Expectedly, the TagRFP fusion protein exhibited diffuse cytosolic staining, while the GAP-TagRFP fusion protein was restricted to the cell surface.

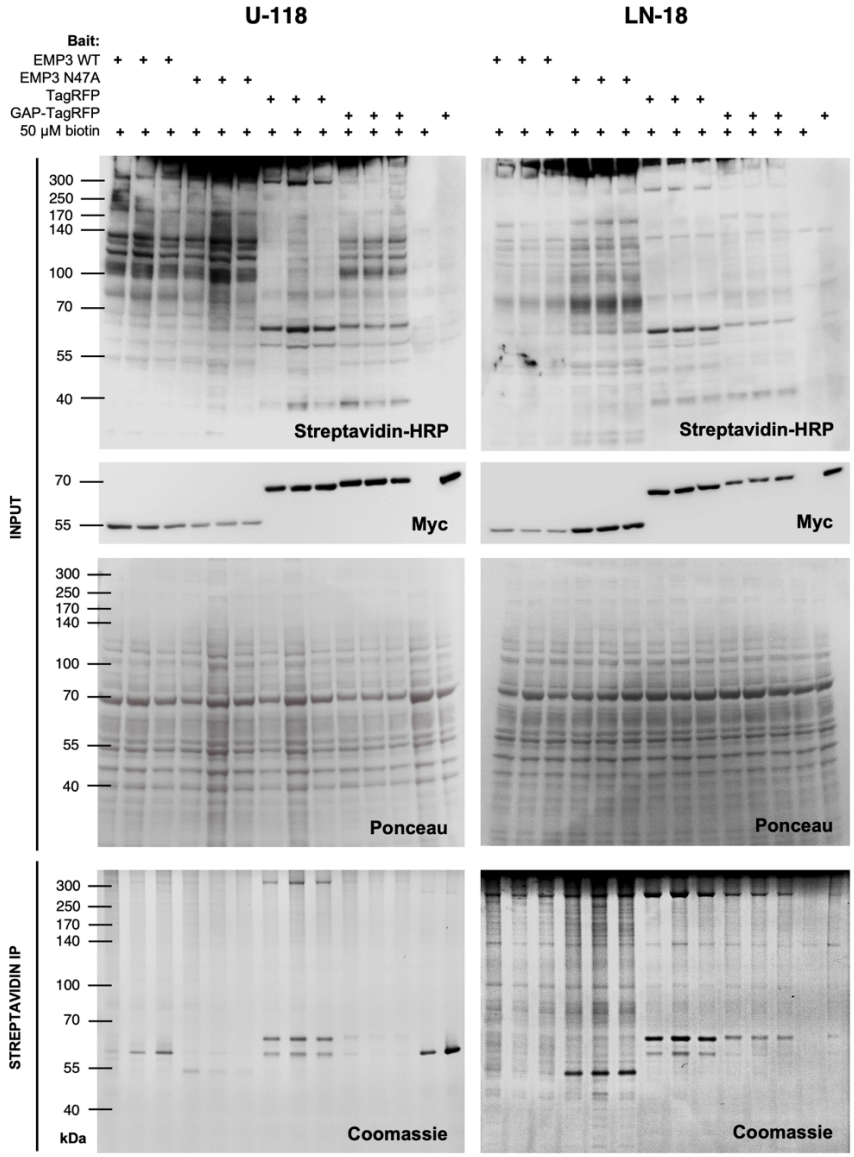

Figure 9. Validation of the expression, biotinylation activity, and purification of BioID2 fusion proteins. Western blotting for the Myc tag confirmed proper fusion protein expression in stably transfected cells. Furthermore, streptavidin-HRP blots verified intact biotin ligase activity of the fusion proteins. Ponceau staining confirmed equal loading of input proteins in all lanes. Lastly, Coomassie staining of streptavidin pull-down eluates indicated proper purification of biotinylated proteins.

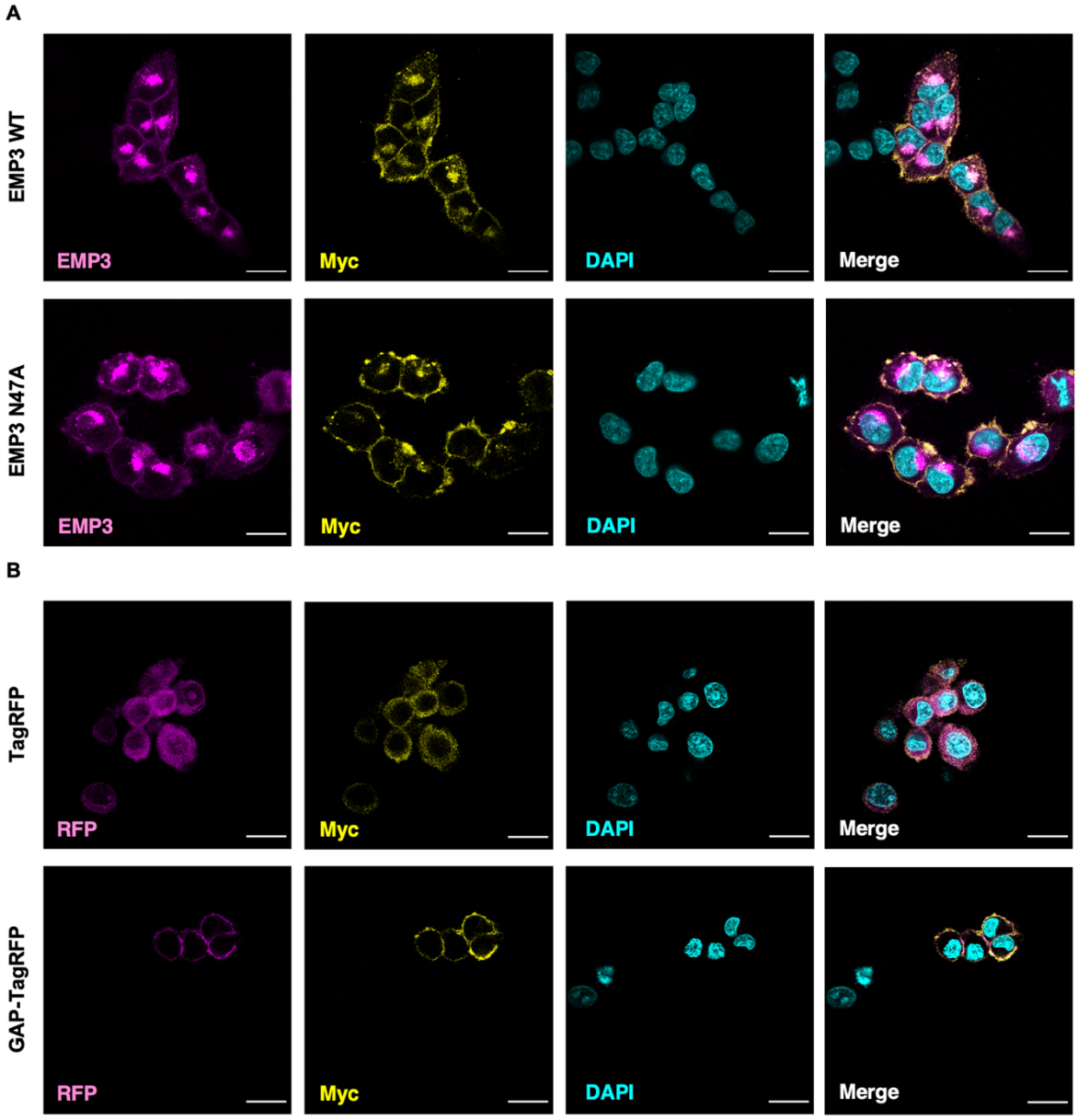

Figure 10. Confirmation of BioID2 fusion protein localization by immunostaining. LN-18 cells stably transfected with the BioID2 constructs were subjected to immunofluorescence staining to confirm proper localization of the bait proteins. EMP3 bait proteins were stained using EMP3 158/2 and Myc tag antibodies, while spatial reference controls were stained with Myc tag antibodies alone. In addition, TagRFP fluorescence was detected upon excitation of TagRFP/GAP-TagRFP cells with the 561 nm laser. Nuclei were stained with DAPI. U-118 immunostaining was also performed as reported in a manuscript draft that will be separately submitted for publication. Scale bar = 20 µm.

To prepare samples for mass spectrometry analysis, stably transfected LN-18 and U-118 cells were treated with 50 µM of biotin for 18 hours, and the resulting lysates were subsequently subjected to streptavidin pull-downs (Fig. 8A). Streptavidin-HRP blots confirmed the presence of biotinylated proteins in lysates collected from stably transfected and biotin-treated cells but not in untransfected nor in biotin-depleted negative controls (Fig. 9). In addition, streptavidin pull-downs of the transfected and biotin-treated cells exhibited increased band intensities relative to the negative controls upon Coomassie staining (Fig. 9). Subsequently, the pull-

downs were subjected to MS analysis through the MS-based Protein Analysis Unit, and the identified proteins further analyzed by network mapping and enrichment analysis.

4.2 BioID2-based proximity labeling reveals the spatial context of EMP3

4.2.1 The core EMP3 interactome consists of GBM-associated membrane receptors and various protein trafficking regulators

To identify EMP3-interacting proteins from the resulting BioID2 data, statistical analysis was independently performed for each bait (i.e., EMP3 WT and N47A) and using each spatial reference control. EMP3 WT or N47A-proximal proteins were defined as 1) proteins that were significantly enriched in the EMP3 WT or N47A pull-downs (i.e., $\log_2$-FC ≥ 1 and Welch's t-test p-value ≤ 0.05) relative to either spatial reference control (Fig. 11 and 12) and 2) proteins that were uniquely identified in EMP3 WT or N47A pull-downs but were absent (i.e., LFQ intensity = 0) in all three replicates of either control. Previously identified EMP3 interacting partners were identified using this approach (e.g. CD44, FLOT1, VAMP3, ATP5B, CD47 etc.), thus validating the chosen strategy. Notably, majority of the identified hits were not previously known to be associated with EMP3 according to the STRING and BioGRID PPI databases; thus, this study substantially expands the list of potentially *bona fide* EMP3 interactors, specifically in the context of GBM.

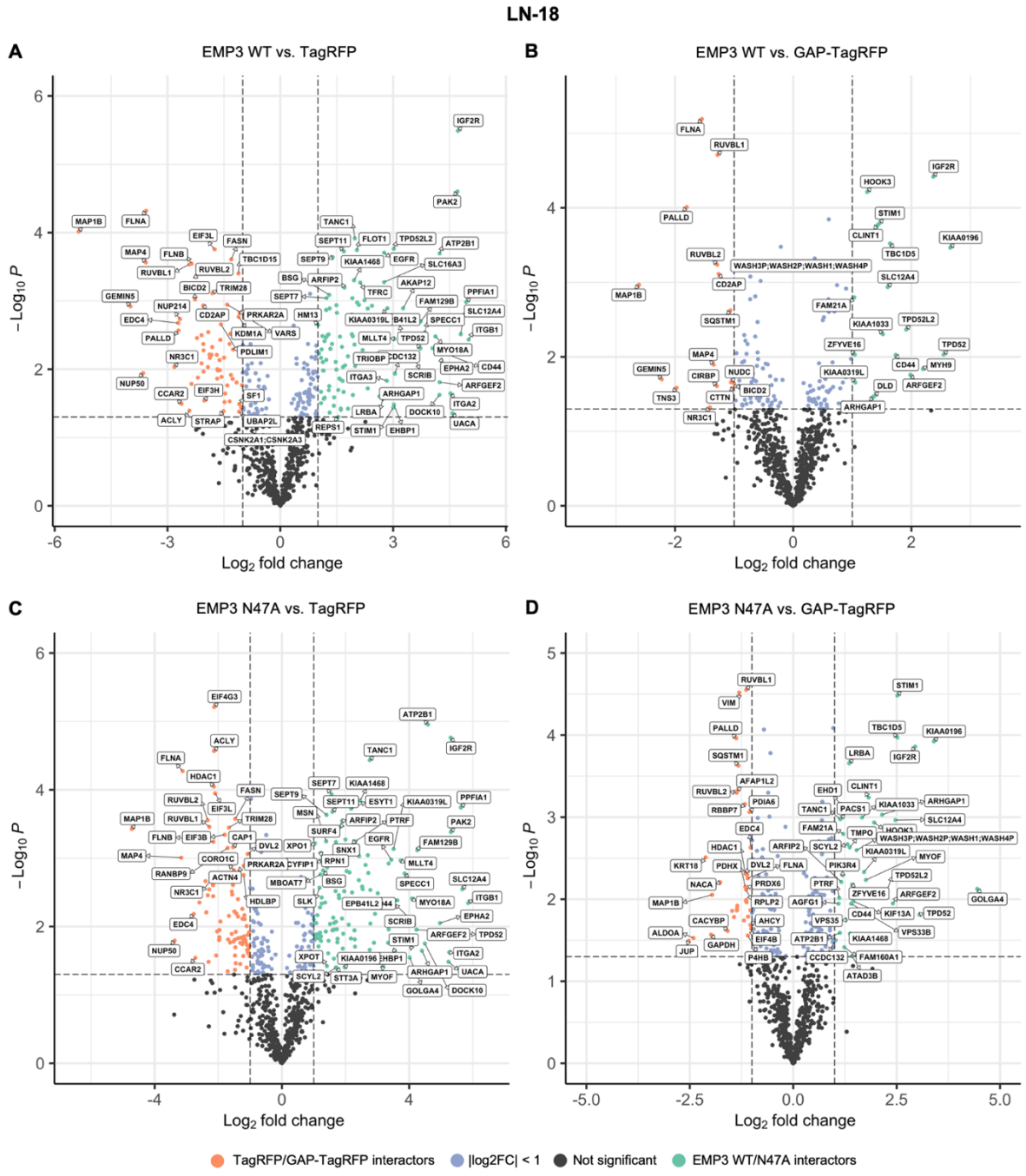

Figure 11. Volcano plots showing enrichment of EMP3-proximal proteins in LN-18 cells. Log_2-FCs and p-values of proteins identified by MS analysis are plotted on the x- and y-axis, respectively. A log_2-FC cut-off ≥ 1 and p-value cut-off ≤ 0.05 were used to identify EMP3-proximal proteins. Proteins preferentially enriched in EMP3 WT (A and B) or N47A (B and D) relative to TagRFP or GAP-TagRFP pull-downs are shown in green. Proteins proximal to the spatial reference interactors are depicted in red, while proteins that did not satisfy the log_2-FC or p-value cut-offs are shown in purple and black, respectively.

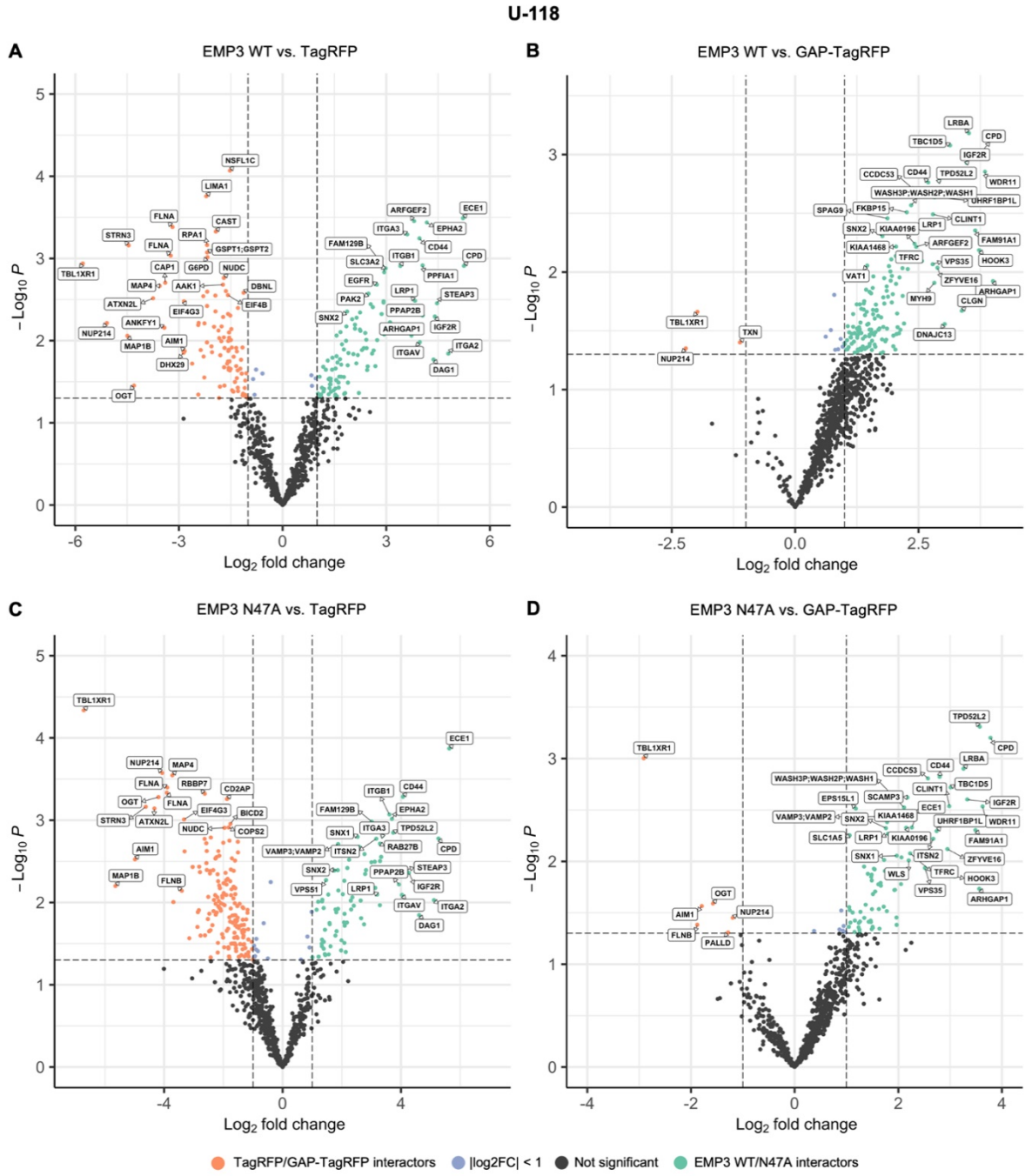

Figure 12. Volcano plots showing enrichment of EMP3-proximal proteins in U-118 cells. Log_2-FCs and p-values of proteins identified by MS analysis are plotted on the x- and y-axis, respectively. A log_2-FC cut-off ≥ 1 and p-value cut-off ≤ 0.05 were used to identify EMP3-proximal proteins. Proteins preferentially enriched in EMP3 WT (A and B) or N47A (B and D) relative to TagRFP or GAP-TagRFP pull-downs are shown in green. Proteins proximal to the spatial reference interactors are depicted in red, while proteins that did not satisfy the log_2-FC or p-value cut-offs are shown in purple and black, respectively.

Interestingly, each pairwise comparison yielded a unique set of interactors that reflects the enrichment bias resulting from the localization of the spatial reference control used. For example, proteins enriched in EMP3 WT relative to TagRFP tend to be enriched for plasma membrane proteins (Fig. 13). Conversely, most organellar proteins tend to be overrepresented

in the EMP3 WT vs. GAP-TagRFP comparison, although the results were slightly different for each cell line. Proteins localizing in the cytosol, Golgi, endoplasmic reticulum (ER), lysosomes, and mitochondria were enriched in U-118 EMP3 WT/GAP-TagRFP (Fig. 13 A), while endosomal, Golgi, and nuclear proteins were enriched when making the equivalent comparison in LN-18 (Fig. 13 B). Given that EMP3 shuttles between the plasma membrane and cytoplasmic membrane-bound compartments, it is likely that these spatially distinct set of proteins simply correspond to the membrane and cytosolic interactors of EMP3. Thus, the union of EMP3 WT/TagRFP and EMP3 WT/GAP-TagRFP hits were taken to comprise the full interactome in each cell line.

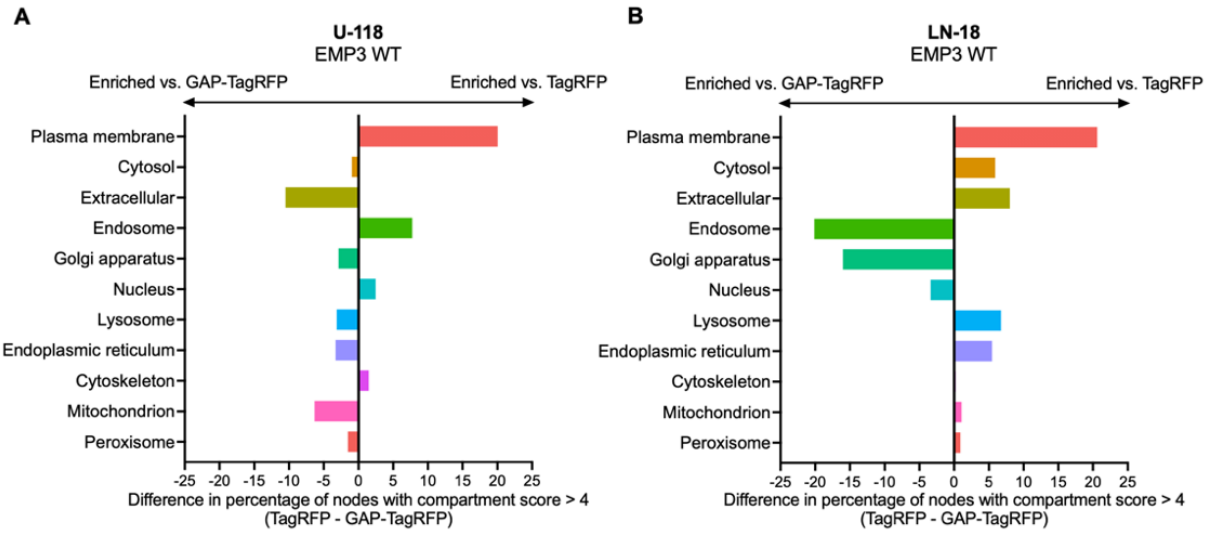

Figure 13. Enrichment of EMP3-proximal proteins in various cellular compartments. Bar graphs show the difference in the percentage of nodes with compartment score > 4 in each cellular compartment when using TagRFP or GAP-TagRFP as the spatial reference control in U-118 (A) and LN-18 (B) cells.

MS analysis identified a total of 232 and 336 EMP3 WT-proximal proteins using both spatial reference controls in LN-18 and U-118 GBM cells, respectively (Fig. 14). To gain further biological insight on EMP3's interaction network, network mapping and enrichment analysis were performed in STRING (version 11.5) and Cytoscape (version 3.9.1), using the 103 EMP3 WT-proximal proteins common to both LN-18 and U-118 cells as input. Designated as the core EMP3 interactome, this network revealed enrichment of GBM-associated transmembrane proteins (e.g., EGFR, CD44, integrins, solute carrier transporters or SLCs) as well as various trafficking regulators (Fig. 14). The latter includes proteins associated with clathrin-coated vesicles (CCVs), as well as components of the retromer, endosome-associated recycling protein (EARP), Wiskott-Aldrich Syndrome protein and scar homologue (WASH), and soluble

N-ethylmaleimide-sensitive factor attachment protein (SNARE) complexes. Functionally, the EMP3-proximal membrane proteins identified are involved in a variety of oncogenic pathways relevant to GBM, including RTK signaling, Hippo-Merlin signaling, and integrin signaling. Meanwhile, the trafficking regulators identified are mostly involved in trans-Golgi network (TGN)-to-endosome retrograde trafficking, suggesting that EMP3 may be involved in this process.

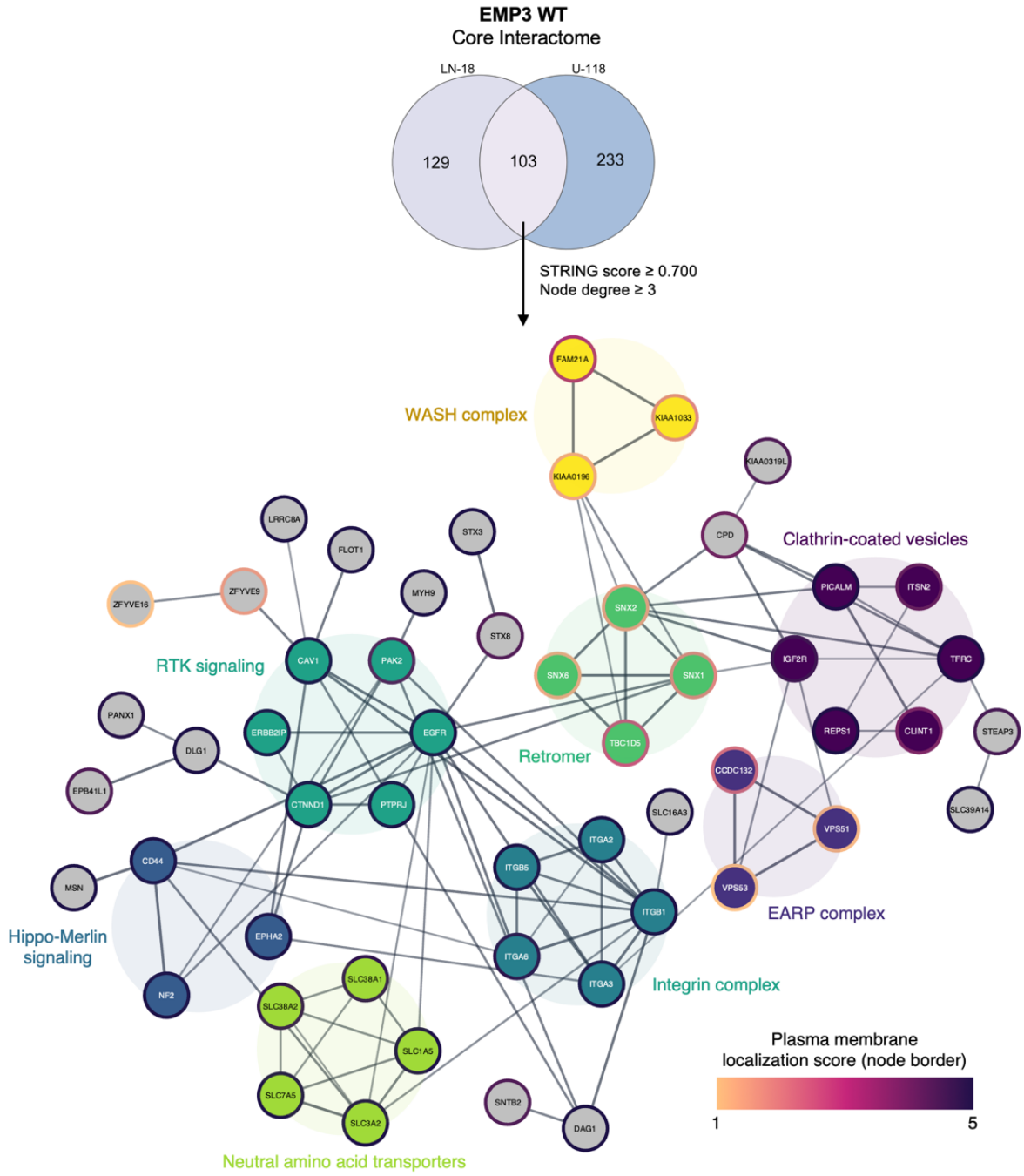

Figure 14. The core interactome of EMP3. The STRING interaction network depicts EMP3 WT-proximal proteins that are common between LN-18 and U-118 cells. Only edges with STRING scores ≥ 0.700 and nodes with degrees ≥ 3 were included in the network. Nodes are colored and clustered according to the functional groups identified by STRING enrichment analysis. Node borders indicate plasma membrane localization scores.

Among the core set of EMP3-interacting proteins, only 9 hits were consistently identified in both LN-18 and U-118 cells regardless of the spatial reference control used. Out of these 9 proteins, only 5 were retained after filtering for high-confidence (STRING score ≥ 0.700) and well-connected nodes (i.e., degree ≥ 3) in Cytoscape. These proteins, which may represent high-confidence hits that constantly interact with both membrane-bound and cytosolic EMP3 regardless of the cellular context, include the following: 1) CD44, an extracellular surface marker found in mesenchymal glioblastomas; 2) zinc finger FYVE domain-containing protein 9 (ZFYVE9), which recruits SMAD2 and SMAD3 proteins to the TGF-β receptors; 3) TBC1 domain family member 5 (TBC1D5), a GTPase-activating protein that inactivates the late endosomal marker RAB7A; 4) cation-independent mannose-6-phosphate receptor (IGF2R), which transports lysosomal enzyme precursors from the TGN to lysosomes, and 5) clathrin interactor 1 (CLINT1), a regulator of TGN-to-endosome transport.

4.2.2 Confirmatory PPI assays validate several BioID2 hits as EMP3 interactors

To orthogonally validate the BioID2 screen, confirmatory PPI assays were performed. First, EMP3's interaction with the GBM driver EGFR and representative trafficking regulators were confirmed by proximity ligation assay (PLA). PLA is an antibody-based method that allows *in situ* PPI detection via fluorophore-conjugated oligonucleotide probes. Using this method, EMP3's interaction with EGFR and the trafficking regulators TBC1D5 and CLINT1 were validated (Fig. 15). Additionally, the EARP member vacuolar protein sorting-associated protein 53 homolog (VPS53) and the retromer components sorting nexin-1 (SNX1) and sorting nexin-2 (SNX2) were also confirmed as EMP3 interactors by PLA.

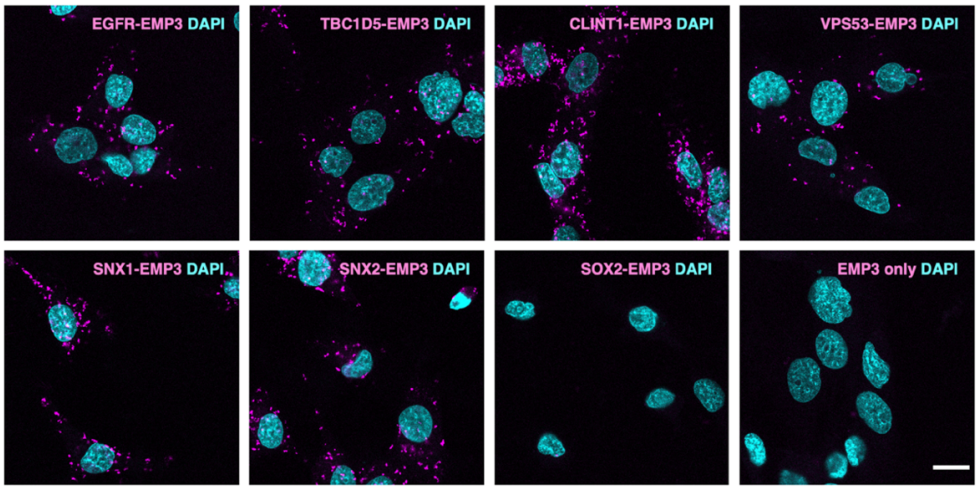

Figure 15. Proximity ligation assays confirm novel EMP3 interactors identified by BioID2. PLA signals (pink) indicate proximity (~40-nm distance) between EMP3 and the tested proteins. SOX2 was used as negative control. Nuclei were stained with DAPI (cyan). Scale bar = 20 µm.

Additionally, an affinity purification-mass spectrometry (AP-MS) screen was carried out in LN-18 cells, with the goal of identifying proteins that maintain a stable and direct interaction with EMP3 even after cell lysis. Briefly, EMP3 WT and N47A proteins fused to a FLAG tag at the C-terminal end were stably expressed in LN-18 cells and further purified along with stably interacting proteins using a FLAG antibody resin. MS analysis of the eluates revealed CD44 to be the only common hit between the EMP3 WT and N47A AP-MS and the LN-18 BioID2 screens (Fig. 16). Thus, virtually all BioID2 hits, except CD44, can only interact with EMP3 *in situ* (i.e., in the context of an intact subcellular environment).

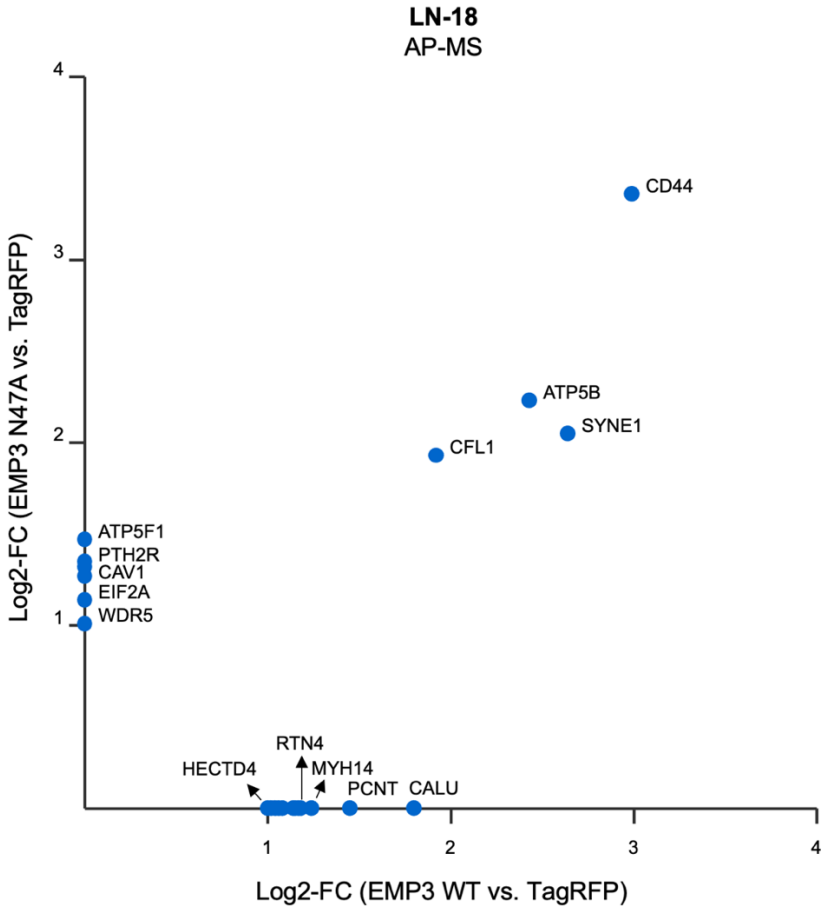

Figure 16. AP-MS screen of EMP3 WT and N47A interactors in LN-18 cells. Scatter plot showing proteins that selectively co-immunoprecipitated with EMP3 WT-FLAG and/or EMP3 N47A-FLAG proteins versus the TagRFP-FLAG control. Axes correspond to $\log_2$-FCs.

Further supporting the results of the AP-MS screen, FLAG pull-down experiments performed using LN-18 and U-118 cells stably transfected with FLAG-tagged EMP3 constructs showed co-immunoprecipitation of EMP3 and the ~80 kDa band corresponding to CD44s, the standard isoform of CD44 (Fig. 17 A-B). In agreement with the BioID2 and AP-MS data, EMP3 N47A also co-immunoprecipitated with CD44s, indicating that EMP3 glycosylation is not necessary for this interaction. Reciprocal pull-downs using FLAG-tagged CD44s also showed co-

immunoprecipitation with EMP3 (Fig. 17 C-D). Because this isoform does not contain any of the domains coded by alternatively spliced CD44 variant exons, it can be concluded that the canonical CD44 structural domains are sufficient for mediating CD44's interaction with EMP3.

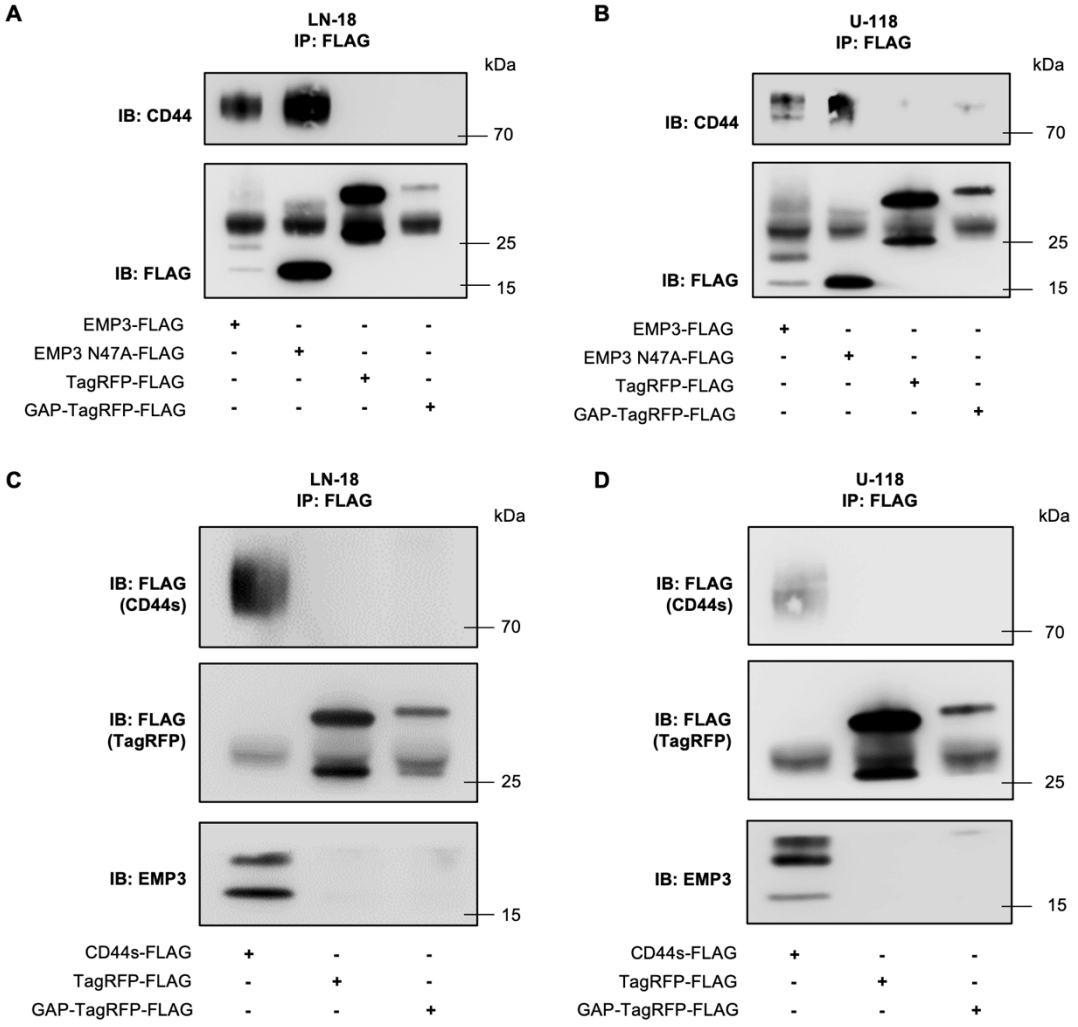

Figure 17. FLAG pull-downs confirm EMP3's interaction with the standard CD44 isoform, CD44s. FLAG-tagged EMP3 WT and N47A expressed in LN-18 (A) and U-118 (B) cells co-immunoprecipitated with the ~80 kDa band corresponding to the CD44s isoform. Reciprocal CD44s-FLAG pull-downs in LN-18 (C) and U-118 (D) cells further confirm the interaction with EMP3. Each figure represents n=2 independent pull-downs; thus, the interaction was confirmed across 8 independent and orthogonal experiments.

4.2.3 BioID2 identifies cell line-specific and glycosylation-dependent EMP3 interactors

Further comparative analysis of the BioID2 hits also identified context-dependent interactors of EMP3. Comparison of the total set of EMP3 WT and N47A interactors between the two cell lines revealed 263 and 180 unique interactors in LN-18 and U-118, respectively (Fig. 18). Reactome pathway-based enrichment analysis of the filtered nodes highlighted LN-18-specific overrepresentation of proteins involved in Rho GTPase (e.g., ROCK1, ROCK2, ARHGEF12) and MAPK signaling (e.g., MET, PDGFRB). Additionally, proteins involved in cell-to-cell

communication (e.g., MLLT4, INADL, PVRL2) and GLUT4 translocation to the membrane (e.g., exocyst complex components and STX4) interacted with EMP3 in LN-18 cells only (Fig. 18).

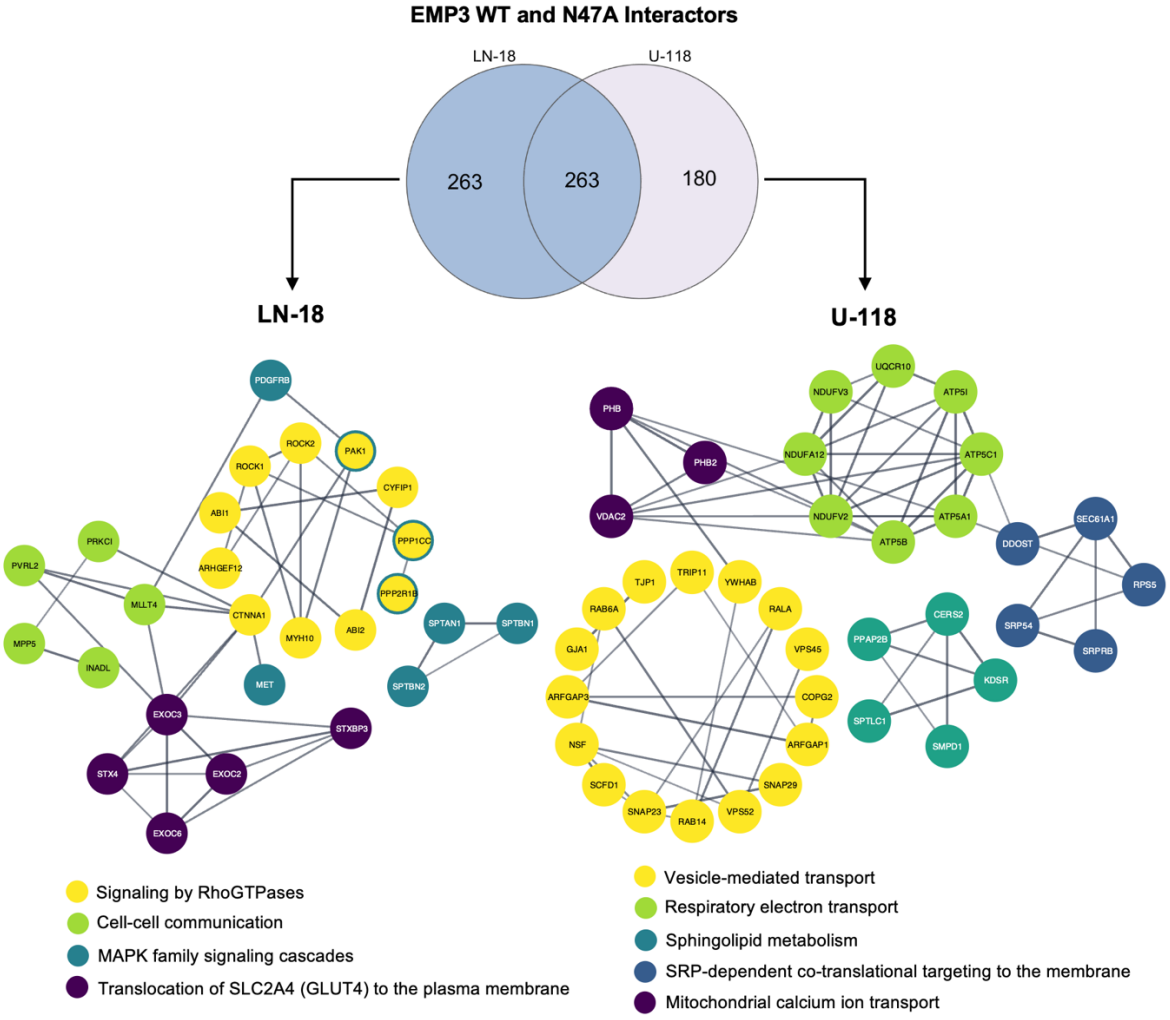

Figure 18. Cell line-specific interactors of EMP3. The STRING interaction networks depict proteins that interact with EMP3 WT/N47A in LN-18 (left) or U-118 (right) cells only. Only edges with STRING scores ≥ 0.700 and nodes with ≥ 2 interactors within 1 neighboring distance were included in the network. Nodes are colored and clustered according to the functional groups identified by STRING enrichment analysis. The colored borders on PAK1, PPP1CC, and PPP2R1B indicate their inclusion in the MAPK cluster as well.

On the other hand, a distinct set of vesicular trafficking proteins not found in the EMP3 core interactome were uniquely enriched in the U-118-specific EMP3 interaction network (Fig. 18). This cluster is specifically enriched for Golgi-localizing proteins involved in ER-to-Golgi anterograde transport (e.g., NSF), Golgi-to-ER retrograde transport (e.g., RAB6A), or both (e.g., COPG2, ARFGAP1, ARFGAP3). In addition, there was overrepresentation of mitochondrial-localizing proteins involved in oxidative phosphorylation and mitochondrial calcium ion transport, as well as proteins associated with sphingolipid metabolism. Interestingly, proteins functioning in signal recognition particle (SRP)-dependent co-

translational protein targeting to the membrane (e.g., SRP54, SRPRB, SEC61A1) and oligosaccharyltransferase (OST) complex-mediated *N*-glycosylation (e.g., DDOST) also selectively interacted with EMP3 in U-118 cells. The latter partly aligns with Western blot results showing greater EMP3 glycosylation levels in U-118 relative to LN-18 cells (see Section 4.3.3, Fig. 22 D). Thus, differential glycosylation between LN-18 and U-118 cells may be a direct consequence of cell line-specific interactions of EMP3 with the glycosylation machinery.

Meanwhile, glycosylation appeared to have minimal impact on the EMP3 core interactome, as majority of the hits were identified regardless of whether the EMP3 WT or N47A bait was used (Fig. 19). In contrast, significantly enriched EMP3 WT-specific hits were more frequently observed within the U-118-specific interactome, presumably due to U-118's higher dependence on glycosylation, as evidenced by the higher baseline level of this post-translational modification (PTM) in this cell line. These glycosylation-dependent EMP3 interactors included several mitochondrial-localizing proteins (e.g., NDUFV3, ATP5I, ATP5C1, ATP5A1, PHB, PHB2) as well as most of the proteins from the SRP cluster discussed above. Moreover, several of the abovementioned proteins involved in uni- or bi-directional ER-to-Golgi or Golgi-to-ER transport were also interacting specifically with the glycosylated form of EMP3 (Fig. 19). While further validation of these observations is warranted, the findings suggest that glycosylation of EMP3 may be important for mitochondrial localization and cell type-specific transport processes.

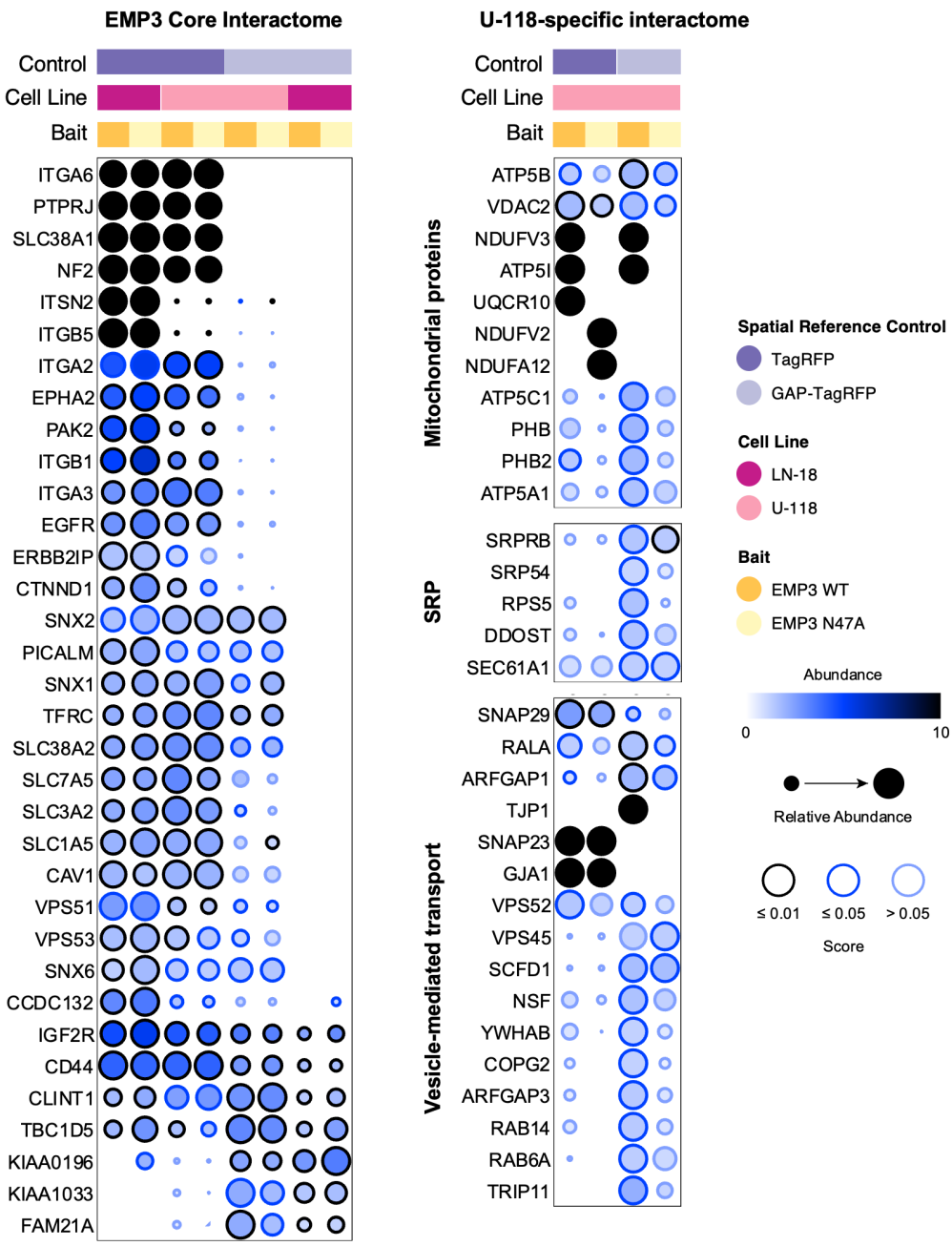

Figure 19. Impact of glycosylation on the EMP3 interactome. Dot plots depict the relative enrichment levels of BioID2 hits belonging to the EMP3 core interactome and its U-118-specific interaction network. Dot colors and sizes correspond to the $\log_2$-FCs of EMP3 WT or N47A baits relative to TagRFP or GAP-TagRFP spatial reference controls. The abundance cap automatically assigns a black fill color to proteins that were detected in EMP3 bait pull-downs only. Border colors correspond to p-values. Dot plots were generated using ProHits-viz (81).

4.3 Establishment and initial characterization of IDH-wt GBM EMP3 KO cellular models

4.3.1 Validation of CRISPR/Cas9-mediated knockout of EMP3

To further define EMP3's exact role within IDH-wt GBM cells, I then sought to validate and characterize reliable EMP3 knockout (EMP3 KO) cell culture models for downstream functional experiments. To this end, CRISPR/Cas9-edited DK-MG, LN-18, and U-118 single-cell clones, in which EMP3 has been deleted by Cas9 guided by an EMP3 guide RNA (gRNA), were obtained from a collaborator, Dr. Arne Christians (Hannover Medical School, Hannover, Germany). Corresponding controls were likewise acquired from the same source. Sanger sequencing of TA clones generated by cloning of the targeted genomic regions confirmed the existence of deleterious mutations or deletions that could mediate nonsense-mediated decay of EMP3 (Fig. 20 A). Confirming proper EMP3 KO, Western blotting showed absence of the band corresponding to EMP3 in cell lines targeted with the EMP3 gRNA (Fig. 20 B). Thus, these cell lines were used for downstream -omics experiments and functional assays.

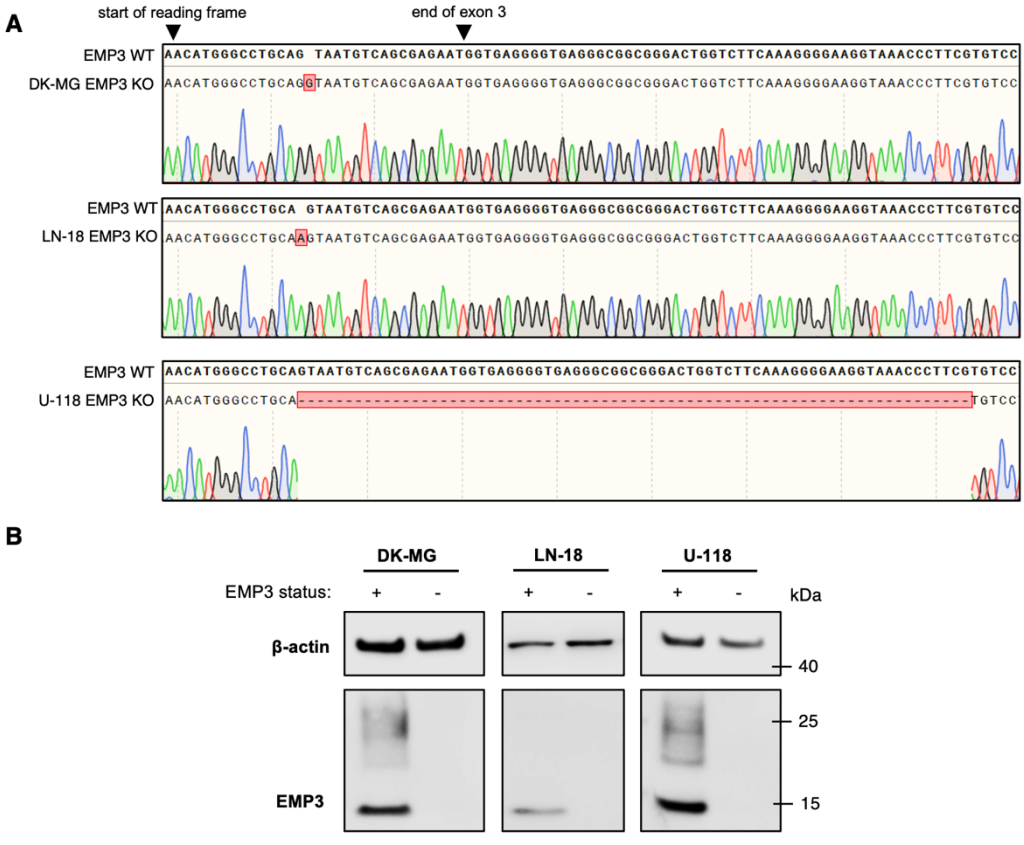

Figure 20. Validation of EMP3 KO IDH-wt GBM cellular models. A) Sanger sequencing of the EMP3 genomic region targeted by CRIPSR/Cas9 in DK-MG, LN-18, and U-118 cells. B) Western blots confirming proper EMP3 KO in the three sequence-verified cell lines.

4.3.2 Copy number analysis reveals characteristic IDH-wt GBM chromosomal changes and distinct genetic drivers for each cellular model

To obtain initial insights on the genetic drivers underlying the acquired cellular models, methylation profiling and copy number analysis was performed in our department. Briefly, wild-type (i.e., EMP3-expressing) DK-MG, LN-18, and U-118 cells were cultured for 72 hours; afterwards, genomic DNA was extracted and sent for methylation and copy number analysis in our molecular diagnostic. Methylation analysis did not provide a significant diagnostic assignment for all three cell lines, which is expected given that these were commercially available cell lines and are not freshly derived from patients. Among the three, only U-118 cells can be assigned a GBM subtype (RTK II); however, the diagnostic score was not significant ($P = 0.175$). On the other hand, copy number profiling revealed that all three cell lines exhibited common genetic alterations found in IDH-wt GBM: chromosome 7 gain with concomitant EGFR, CDK6, and MET amplification, chromosome 9 loss with CDKN2A/B deletion, and loss of chromosome 10 with (e.g. LN-18 and U-118) or without (e.g., DK-MG) PTEN deletion (Fig. 21). Apart from these common changes, each cell line also exhibited unique alterations. For example, DK-MG cells displayed amplification of MYCN, PDGFRA, and the chromosomal regions harboring the tumor suppressors TP53, NF1, and NF2. The greater number of amplifications in DK-MG relative to the other two cell lines may be due to the polyploidy present in this cell line. Meanwhile, LN-18 cells exhibited MDM4 deletions and additional losses in chromosomes 1, 4, and 5. U-118 cells harbored losses in chromosome 6. Additionally, both LN-18 and U-118 displayed chromosome 13 loss with RB1 deletion. Thus, the acquired cellular models simultaneously exhibited CNVs characteristic of GBMs as well as cell line-specific genomic alterations.

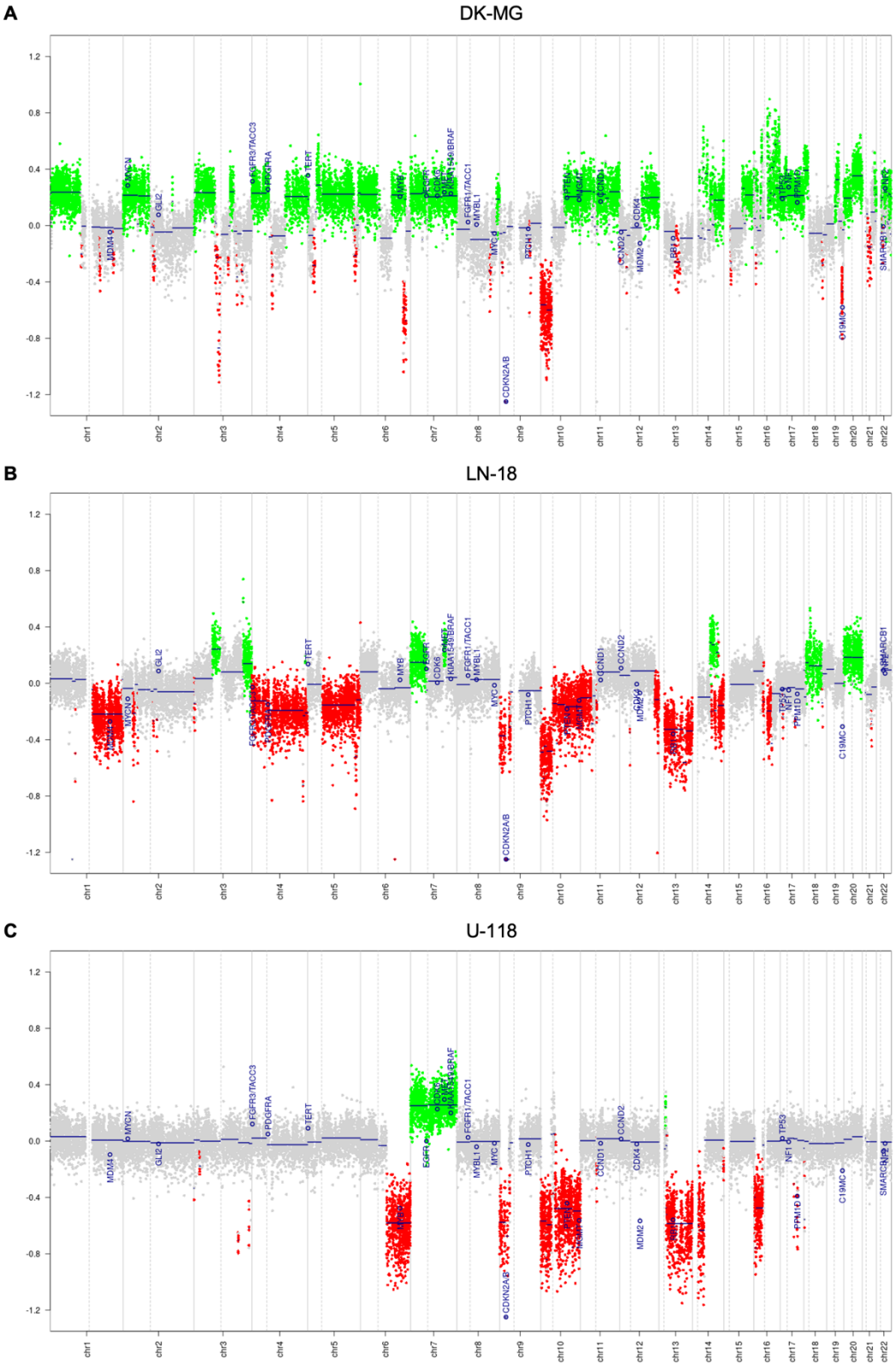

Figure 21. Copy number analysis of GBM cellular models. Copy number plots of DK-MG (A), LN-18 (B), and U-118 (C) cells showing amplified (green) and deleted (red) chromosomal regions.

4.3.3 Exploratory transcriptomic analysis indicates that GBM cellular models segregate along a RTK II/CL axis of variation

To gain a broad overview of the transcriptomic signatures of the cellular models, microarray analysis was also performed using total RNA extracted from 72-hour cultures of DK-MG, LN-18, and U-118 control and EMP3 KO cells. Microarray hybridization was performed by the Microarray Unit of the DKFZ GPCF, and I subsequently analyzed the resulting transcriptomic measurements. Principal component analysis (PCA) indicated that cell line identity accounts for most of the observed variation in gene expression across all cell lines (Fig. 22 A). While DK-MG and U-118 cells appear to segregate from each other within the PCA2 axis, the biggest separation was observed between LN-18 cells and the two other cell lines along the PCA1 axis. This suggests that LN-18 cells are quite distinct from DK-MG and U-118 cells in terms of transcriptomic profile. To determine what genes account for this variation, DK-MG and U-118 transcriptomes were clustered into one group and genes that were upregulated in that cluster compared to LN-18 cells were identified. Enrichment analysis of the upregulated genes revealed that the DK-MG and U-118 cluster characteristically overexpress genes involved in ECM-related processes, including ECM organization and collagen formation. Additionally, this cluster was also enriched in genes involved in RNA metabolism and signal transduction pathways, particularly RTK signaling (Fig. 22 B). This apparent reliance on RTK-dependent pathways suggests that DK-MG and U-118 may resemble RTK II/CL/AC-like GBMs more than LN-18 cells. Indeed, gene set enrichment analysis (GSEA) confirmed that the Verhaak CL gene set is positively correlated with upregulated genes in DK-MG and U-118 when compared to LN-18 cells (Fig. 22 C). On the other hand, Western blotting showed increased expression of the mesenchymal marker CD44 in LN-18 cells, suggesting that this cell line may be closer to the mesenchymal than the RTK II/CL phenotype (Fig. 22 D).

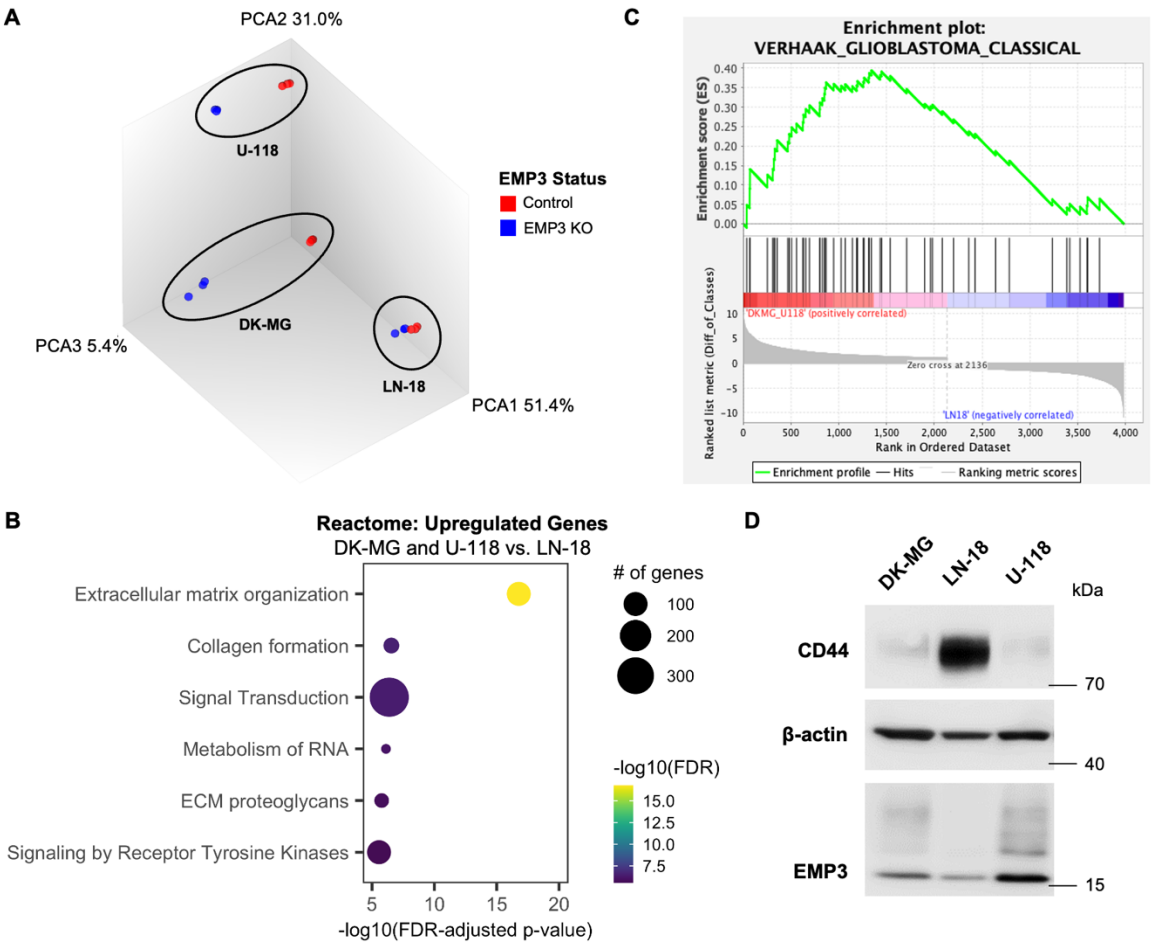

Figure 22. Exploratory analysis of the DK-MG, LN-18, and U-118 transcriptomes. A) PCA plot showing the segregation of control and EMP3 KO GBM cellular models across the three PCA axes. Colors specify EMP3 status. Percentages correspond to relative contribution of each axis to the overall variation in gene expression. B) Top Reactome terms upon enrichment analysis of upregulated genes in the DK-MG and U-118 cluster. C) GSEA plot showing enrichment of the Verhaak CL gene set in the DK-MG and U-118 cluster. D) Western blot showing relative levels of CD44 and EMP3 across the three cell lines.

Meanwhile, EMP3 status was identified to be the main determinant of the segregation along the third PCA axis (Fig. 22 A). While its contribution to overall variation in gene expression was minimal (5.4%), EMP3 KO still led to significant alterations in gene expression within each cell line. In particular, a total of 1415, 390, 1169 DEGs (i.e., absolute $\log_2$-FC$\geq$ 1, FDR-adjusted p-value $\leq$ 0.05) were identified in DK-MG, LN-18, and U-118 EMP3 KO cells relative to corresponding controls, respectively (Fig. 23 A-B). Building on the results of the PCA analysis, the Venn diagrams indicate that there were more common DEGs between DK-MG and U-118 cells than any other pairwise comparison. At the same time, LN-18 had fewer EMP3 KO-dependent DEGs than the two other cell lines, suggesting that this cell line is less sensitive to transcriptomic perturbations induced by loss of EMP3.

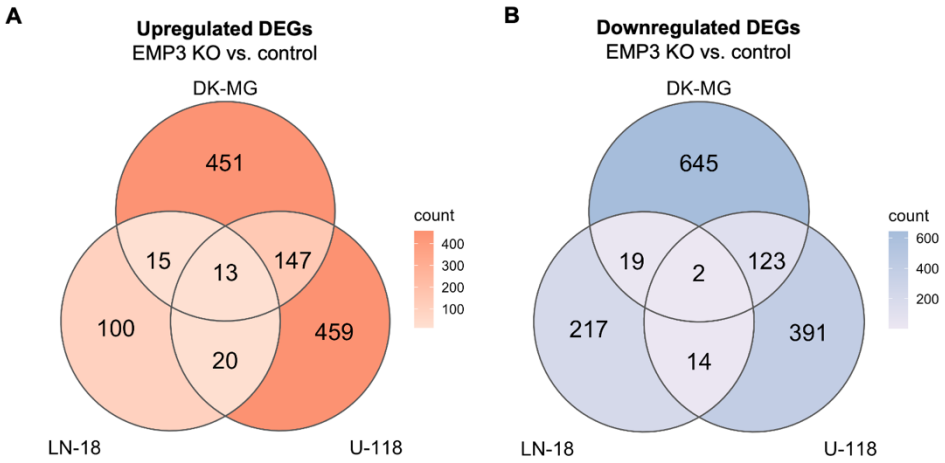

Figure 23. Summary of the number of DEGs in GBM cellular models. A) Venn diagram showing the overlap of upregulated (A) and downregulated (B) genes in the DK-MG, LN-18, and U-118 cells.

Collectively, the observed similarities and differences in transcriptomic signatures and CD44 marker expression prompted this study to designate DK-MG and U-118 cells as approximate models of RTK II/CL GBMs, and LN-18 of MES GBMs. Because DK-MG and U-118 had more commonly perturbed genes in response to EMP3 KO, these two cell lines were considered as interchangeable and supplementary models of EMP3 depletion in the setting of RTK II/CL GBM. On the other hand, the CD44-high MES-like LN-18 cell line was studied independently of the RTK II/CL-like cells in downstream experiments.

4.4 EMP3 sustains the EGFR/CDK2 signaling axis by restricting receptor degradation of EGFR in a TBC1D5-dependent manner

IDH-wt GBMs are primarily driven by dysregulated RTKs, the most notable and frequent of which is EGFR. Because EGFR was identified as an EMP3 interactor in the BioID2 screens, I then sought to examine how EMP3 could potentially regulate EGFR activity. Therefore, a series of biochemical, -omics, and phenotypic experiments was performed using RTK II/CL-like cells, as this subtype was shown to be the most dependent on EGFR signaling by previous studies.

4.4.1 Loss of EMP3 enhances EGF-induced late endosomal shuttling and degradation of EGFR

To begin assessing how EMP3 could impact EGFR activity, the kinetics of EGFR degradation and activation (i.e., phosphorylation at Tyr1068) in serum-starved U-118 control and EMP3 KO cells treated with EGF were measured by immunoblotting. Apart from inducing EGFR

activation, receptor-bound EGF also stimulates the internalization and subsequent degradation of EGFR in lysosomes (84,85); such a homeostatic mechanism normally acts to prevent the overactivation of growth factor receptors in non-malignant cells. To eliminate possible confounding effects of nascently produced receptors on the rate of EGFR degradation, cells were also pre-treated with 100 µg/mL of the protein synthesis inhibitor cycloheximide 1 hour prior to EGF administration. Western blotting of total cell lysates of EGF-treated U-118 control and EMP3 KO cells showed continuous EGFR degradation and extinction of the Tyr1068 signal over the course of 2 hours (Fig. 24 A). Noticeably, the rate of ligand-induced EGFR degradation is higher in the setting of EMP3 depletion, as EGFR levels were significantly lower in U-118 EMP3 KO cells at the 90 min and 120 min time points (Fig. 24 B). The same trend was observed for total EGFR levels in DK-MG cells across three individual trials; however, the difference was not statistically significant after compiling data points from the three trials (Fig. 24 C-D). Nonetheless, the apparent heightened degradation rates in both cell lines suggest that EMP3 restricts EGF-induced endolysosomal degradation of EGFR.

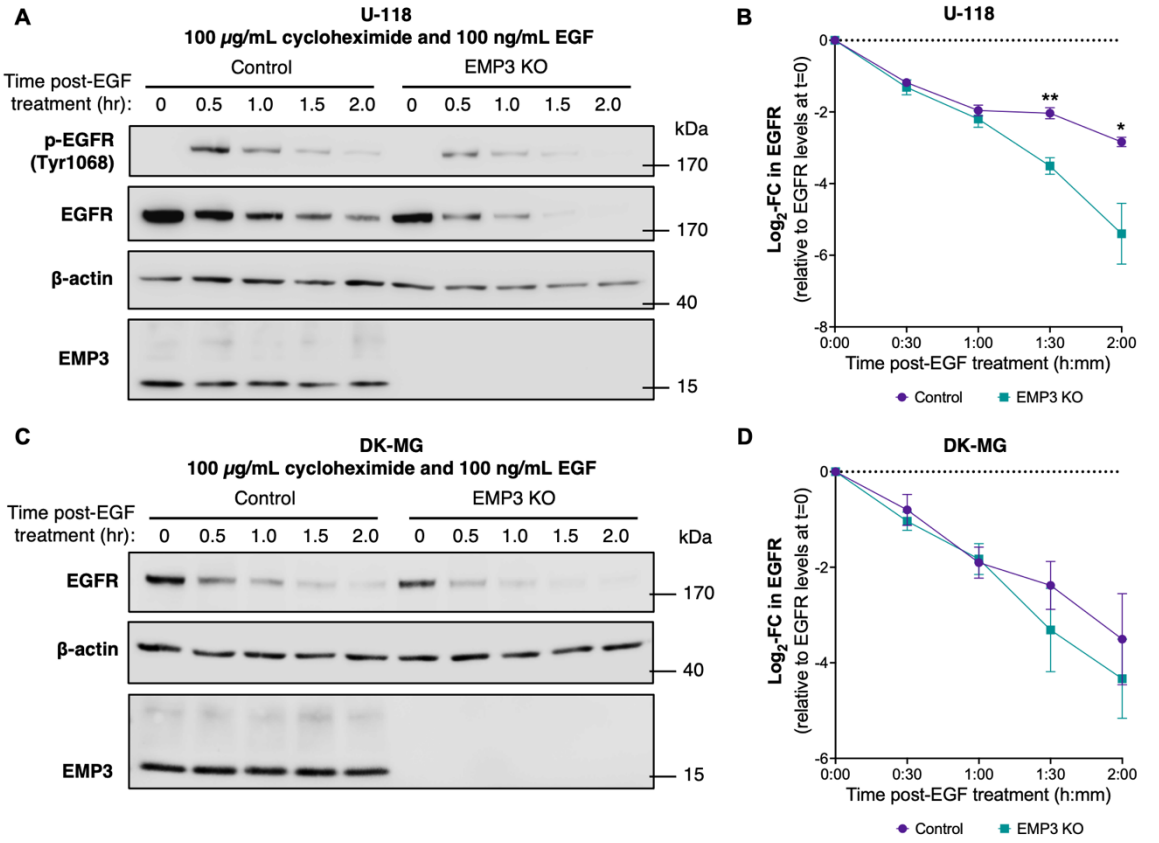

Figure 24. EGFR degradation in enhanced in the setting of EMP3 depletion. Western blotting and band intensity quantifications showing total EGFR levels in EGF-treated U-118 (A, B) and DK-MG (C, D) control and EMP3 KO cells over the course of 2 hours. The displayed blots and graphs represent n=3 independent experiments. Unpaired two-tailed t-test; *P≤0.05; **P ≤ 0.01.

EGFR degradation relies on a well-orchestrated trafficking mechanism that begins with receptor internalization and culminates in shuttling of the receptor from maturing endosomes to lysosomes (85). To test whether the enhanced EGFR degradation in EMP3 KO cells can be attributed to a trafficking defect, the co-localization of Tyr1068-phosphorylated EGFR and the late endosomal regulator RAB7, measured by PLA, were compared between control and EMP3 KO cells treated with 100 ng/mL EGF for 30 minutes. Activated RAB7 has been shown to promote EGFR degradation, as it facilitates the fusion of EGFR-containing late endosomes with lysosomes (84,85). The 30-min time point was chosen because at this point not all the receptors have been degraded as they are still in the process of being shuttled towards lysosomes (84). Quantification of the PLA signals showed increased association of activated EGFR with RAB7 in EGF-treated EMP3 KOs compared to controls (Fig. 25 A-B). Thus, EMP3 may normally serve to reduce endolysosomal degradation of EGFR by attenuating its shuttling towards late endosomes.

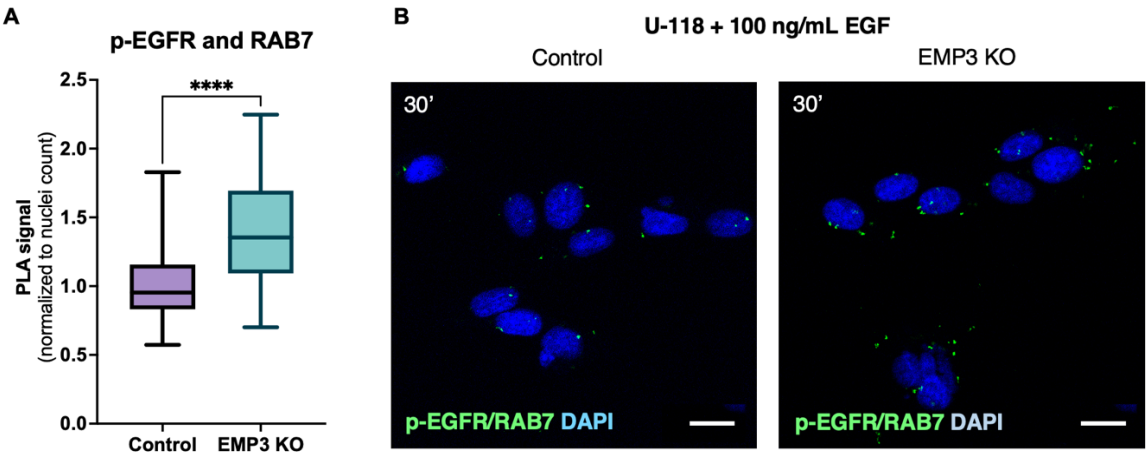

Figure 25. EMP3 KO induces increased EGF-induced association of phosphorylated EGFR and RAB7. A) Box plot of p-EGFR(Tyr1068)-RAB7 PLA signal quantification across n=3 independent experiments. A total of 10 fields were imaged and quantified per trial, and the resulting data points from three trials were compiled and statistically analyzed. Welch's t-test; ****P ≤ 0.0001. B) Representative microscopy images from p-EGFR-RAB7 PLA assays. Scale bar = 20 µm.

4.4.2 Overexpression of wild-type TBC1D5, but not a catalytically inactive mutant, rescues enhanced EGFR degradation in EMP3 KOs

EMP3 has no known catalytic domain and is therefore unlikely to mediate endosomal retention of EGFR on its own. Instead, it is likely to be cooperating with another protein to exert this effect. To identify possible candidates for this presumed mechanism, the endocytic regulators identified in the BioID2 screen were further assessed for any previously known functional associations with RAB7. Interestingly, cytosolic EMP3 appears to interact strongly with

TBC1D5, a retromer component and GTPase-activating protein that inhibits RAB7 activity by facilitating its GTP hydrolysis. Based on the available information, I then hypothesized that EMP3 may indirectly affect RAB7 dynamics and consequently, EGFR trafficking, in a manner dependent on its interaction with TBC1D5. To test this, wild-type TBC1D5 (TBC1D5 WT) and a catalytically inactive variant, TBC1D5 R169A/Q204A (TBC1D5 RQ), were first stably overexpressed in EMP3 KO cells. The proteins were tagged with the FLAG peptide sequence at the C-terminal end to facilitate Western blot detection. Supporting the hypothesis, Western blot results showed that TBC1D5 WT, but not TBC1D5 RQ, can effectively and consistently rescue the effects of EMP3 KO on EGFR degradation across three independent trials (Fig. 26). Thus, EMP3 may cooperate with TBC1D5 to prevent shuttling of internalized EGFR cargoes from endosomes to lysosomes.

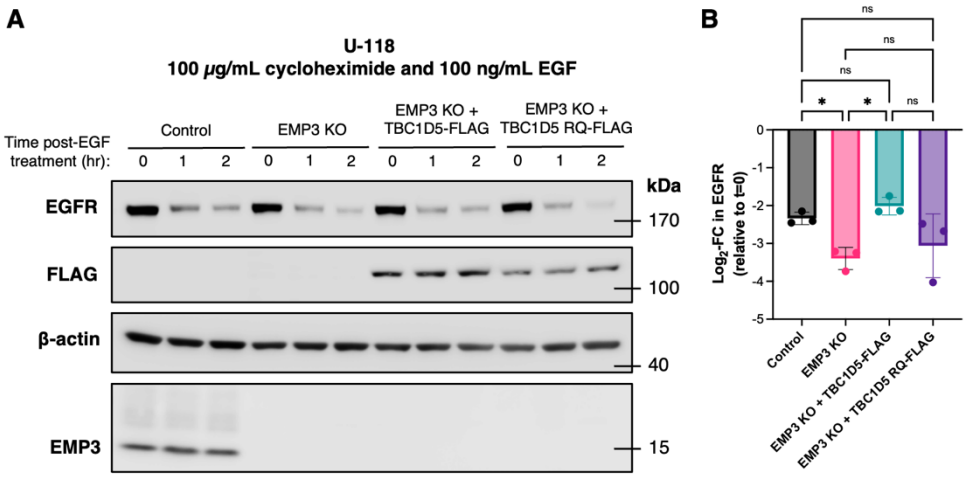

Figure 26. TBC1D5 WT, but not TBC1D5 RQ, reverses the effect of EMP3 KO on EGFR degradation. A) Western blots showing total EGFR levels in EGF-treated U-118 control, EMP3 KO, and TBC1D5 WT/RQ rescue cell lines over the course of 2 hours. B) Bar plot showing the log_2-FC in total EGFR levels of EGF-treated U-118 control, EMP3 KO, and EMP3 KO + TBC1D5 WT/RQ relative to untreated controls after 2 hours. Results are representative of n=3 independent experiments. Welch's ANOVA with Dunnett's T3 multiple comparisons test. ns – not significant; *P≤0.05.

4.4.3 EMP3 depletion inhibits EGFR-dependent transcriptional programs

To test how reduced EGFR stability translates into dysregulation of downstream signaling pathways, additional analysis was carried out using the transcriptomic data generated for DK-MG and U-118 cells. Briefly, DEGs between control and EMP3 KO cells were identified for each cell line, and the resulting lists were filtered and used as input for pathway analysis (Fig. 27 A). A total of 160 commonly upregulated and 125 commonly downregulated genes were identified between DK-MG and U-118 EMP3 KOs (Fig. 27 B-C), hinting that EMP3 depletion may be inducing similar transcriptomic changes in these two cell lines. KEGG enrichment analysis indicated that genes involved in DNA replication and the cell cycle are the most enriched in the list of 125 commonly downregulated genes (Fig. 27 D). In contrast, no KEGG terms were enriched when using the set of commonly upregulated genes as input, suggesting that these transcripts, while coincidentally regulated, are not functionally connected. Thus, EMP3 may be specifically important for sustaining transcriptional programs that drive cellular proliferation in these two RTK II/CL-like cell lines.

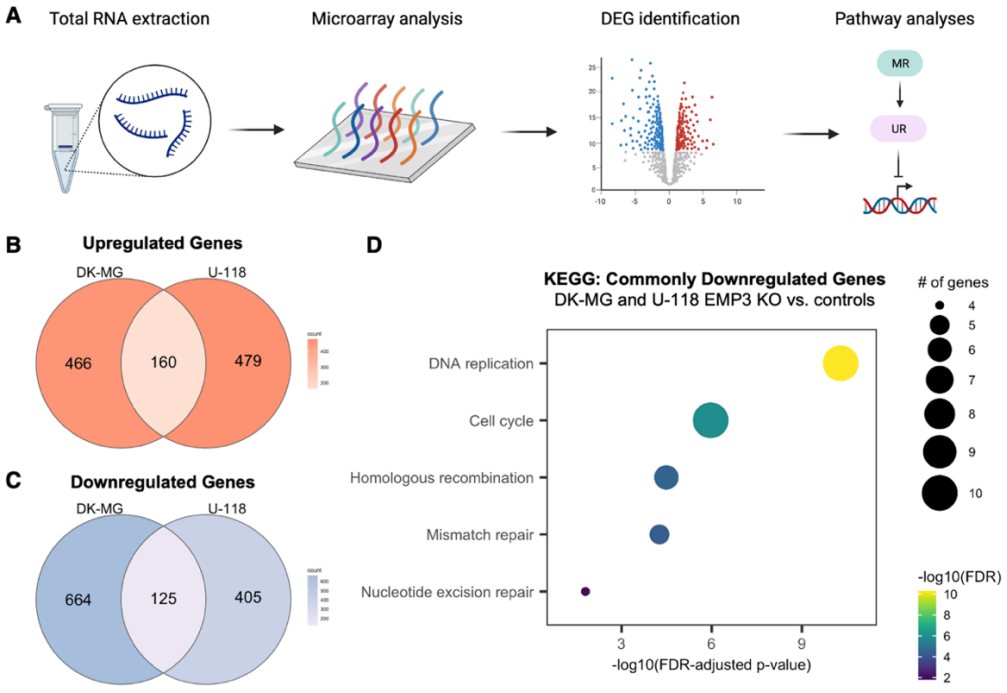

Figure 27. DNA replication- and cell cycle-related genes are downregulated in RTK II/CL-like EMP3 KOs. A) Schematic diagram depicting the workflow for microarray-based gene expression analysis. Figure was created using BioRender.com. B, C) Venn diagram showing the overlap of upregulated (B) and downregulated (C) genes in DK-MG and U-118 EMP3 KOs. D) Dot plot showing KEGG terms enriched in the commonly downregulated gene set. Circle sizes represent number of DEGs associated for each term, while color scale represents -log10(FDR-adjusted p-values).

On the other hand, GSEA of the DK-MG and U-118 DEGs revealed that an EGFR activation signature previously identified in lung cancer cells (86) was enriched in EMP3-expressing control cells. Conversely, the EGFR inhibition gene set defined by the same study was overrepresented in EMP3 KO cells (Fig. 28). In line with the degradation assays, this analysis orthogonally shows that EMP3 KO attenuates EGFR activity in both DK-MG and U-118 cells.

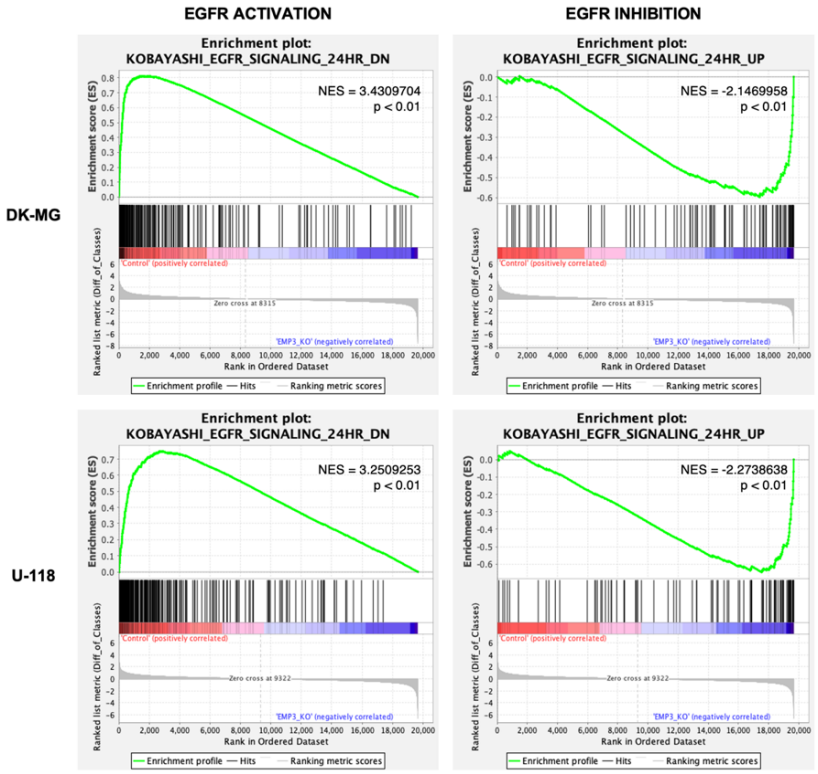

Figure 28. GSEA of DK-MG and U-118 DEGs. Enrichment plots showing upregulation of EGFR activation (left panel) and inhibition (right panel) signatures in DK-MG (top) and U-118 (bottom) control and EMP3 KO cells, respectively. DEGs (black bars) were sorted based on the $\log_2$-FCs between control and EMP3 KO cells. Genes that are upregulated in control and EMP3 KO cells are marked by the red and blue segments, respectively. Enrichment scores (ES) of contributing genes are continuously plotted in green along the x-axis. A positive or negative ES score (y-axis) indicates a positive correlation with genes upregulated in control or EMP3 KO cells, respectively. NES: normalized enrichment scores.

To further obtain biological insight from the transcriptomic data, upstream pathway analysis was independently performed for each cell line using the Ingenuity Pathway Analysis (IPA) software (Qiagen) and the list of DEGs as input. This approach identified putative activated (i.e., z-score ≥ 2, p-value ≤ 0.05) and inhibited (i.e., z-score ≤ -2, p-value ≤ 0.05) master regulators (MRs) that could potentially account for the transcriptomic changes induced by EMP3 KO. In line with the GSEA results, the EGFR ligand EGF was determined to be among the commonly inhibited MRs in both DK-MG and U-118 cells (Fig. 29 A-B). Furthermore, enrichment analysis of the inhibited MRs within DK-MG and U-118 EMP3 KOs also showed

that RTK-dependent signaling pathways (e.g., PI3K/AKT and MAPK) are negatively affected in both cell lines (Fig. 29 C-D).

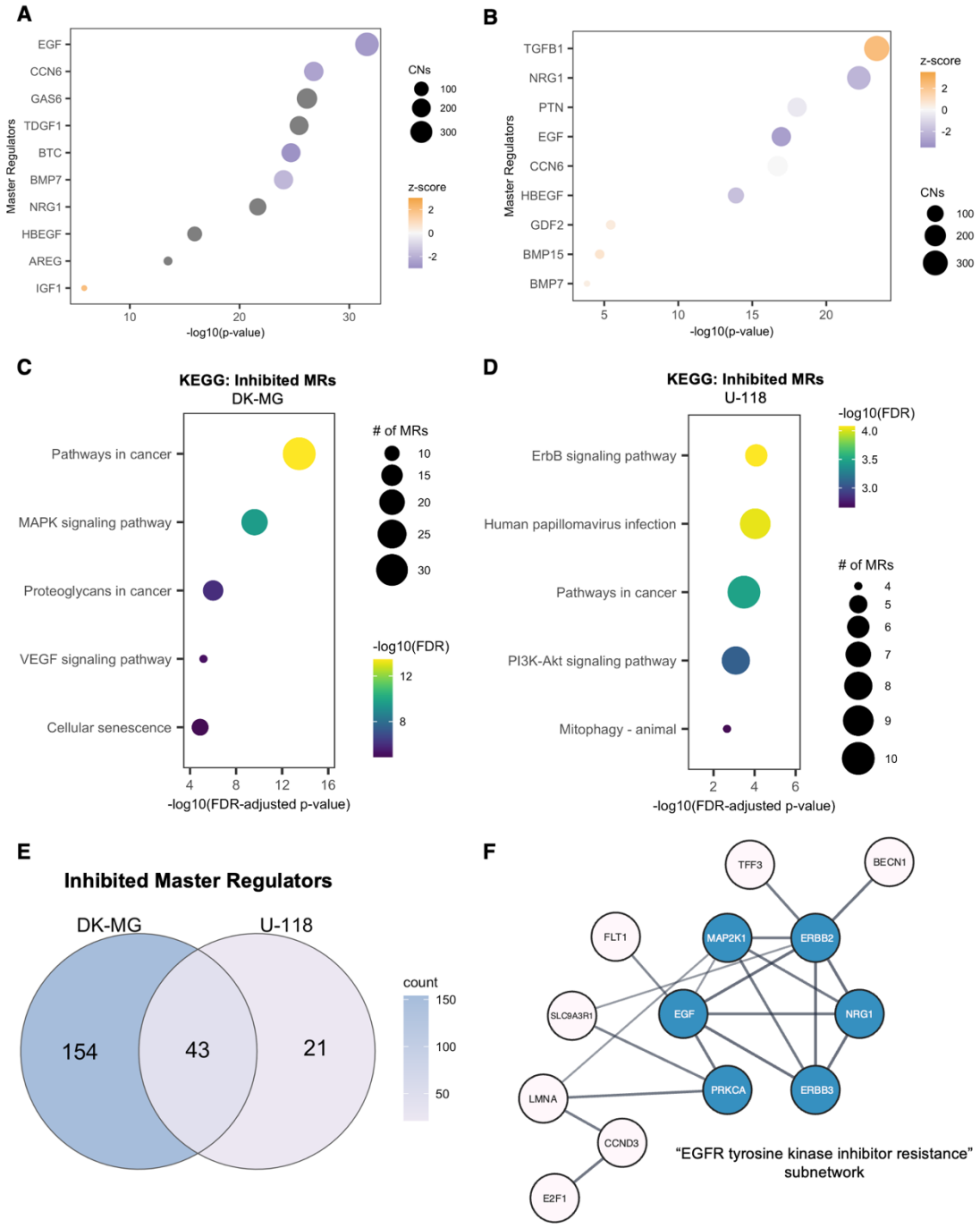

Figure 29. IPA analysis of DK-MG and U-118 DEGs. A,B) Dot plots showing inhibited master regulators (MRs) in DK-MG (A) and U-118 (B) EMP3 KOs. Color scale corresponds to activation z-scores (orange – activated; purple – inhibited), while circle sizes indicate the number of associated causal networks (CNs) for each MR. C,D) Dot plots showing top KEGG terms overrepresented within DK-MG (C) and U-118 (D) MRs. Color scale corresponds to -log10(FDR-adjusted p-values), while circle sizes denote the number of associated MR per term. E) Venn diagram showing the overlap of inhibited MRs in DK-MG and U-118 cells. F) An "EGFR tyrosine kinase inhibitor resistance" subnetwork is enriched among the network of commonly inhibited MRs.

Network analysis of the 43 commonly inhibited MRs in both cell lines further revealed overrepresentation of a subnetwork involved in EGFR tyrosine kinase inhibitor resistance (Fig. 29 E-F). Notably, this subnetwork included known EGFR/RTK ligands (e.g., EGF, NRG1), dimerization partners (e.g., ERBB2, ERBB3), and downstream effectors (e.g., MAP2K1, PRKCA), hinting that impaired EGFR stability may also be correlated with or negatively impacting the activity of its interactors. Taken together, the results of the microarray-based gene expression profiling point toward the dysregulation of EGFR and its downstream signaling in RTK II/CL-like DK-MG and U-118 cells, which culminates in the reduced transcription of genes involved in cell cycle progression.

4.4.4 Phosphoproteomic analysis reveals that EMP3 KO in RTK II/CL-like cells converges into CDK1/2 inhibition

To further characterize signaling defects induced by the loss of EMP3, mass spectrometry-based phosphoproteomic analysis of DK-MG and U-118 control and EMP3 KO cells was performed. Briefly, total cell lysates were collected from GBM cells and submitted to the MS-based Protein Analysis Unit for phosphopeptide enrichment and MS analysis (Fig. 30 A). This led to the identification of 2569 and 628 differentially phosphorylated sites (i.e., absolute $\log_2$-FC ≥ 1 and FDR-adjusted p-value ≤ 0.05) in DK-MG and U-118 EMP3 KOs, respectively (Fig. 30 B and 31). Strikingly, DK-MG EMP3 KOs had more phosphosite alterations than U-118 KOs, suggesting that the former is more susceptible to signaling defects caused by loss of EMP3. Intersection of the identified phosphosites revealed a total of 190 common differentially regulated phosphosites between the two cell lines; out of these, 160 were regulated in the same manner (i.e., $\log_2$-FC in the same direction) (Fig. 30 C). Notably, dephosphorylation events were highly overrepresented within the set of commonly regulated phosphosites (i.e., 157 common dephosphorylation events vs. 3 common phosphorylation events). To determine which biological processes could be affected by the common dephosphorylation events, enrichment analysis was performed. Results indicated the cell cycle to be the most significantly enriched Reactome term, with 22 out of 157 dephosphorylated proteins associated with this process (Fig. 30 D). Thus, EMP3 KO may be inducing dephosphorylation of cell cycle regulators in RTK II/CL-like cells.

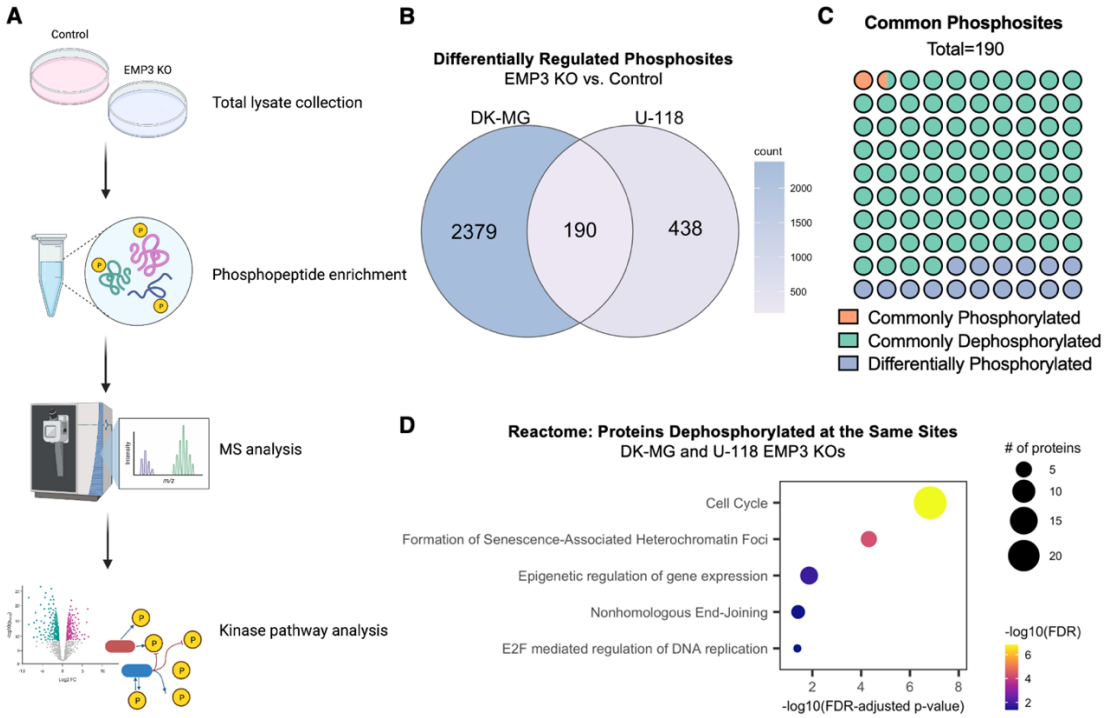

Figure 30. Phosphoproteomic analysis of DK-MG and U-118 EMP3 KOs. A) Phosphoproteomics workflow. Figure was created using BioRender.com. B) Venn diagram of the overlap of differentially regulated phosphosites in DK-MG and U-118 EMP3 KOs. C) Dot plot depicting the proportion of commonly affected phosphosites that are phosphorylated, dephosphorylated, or differentially phosphorylated in DK-MG and U-118 control and EMP3 KO cells. D) Dot plot showing Reactome terms enriched in the set of proteins that are dephosphorylated at the same sites in DK-MG and U-118 EMP3 KOs. Circle sizes represent number of proteins associated for each term, while color scale represents significance levels.

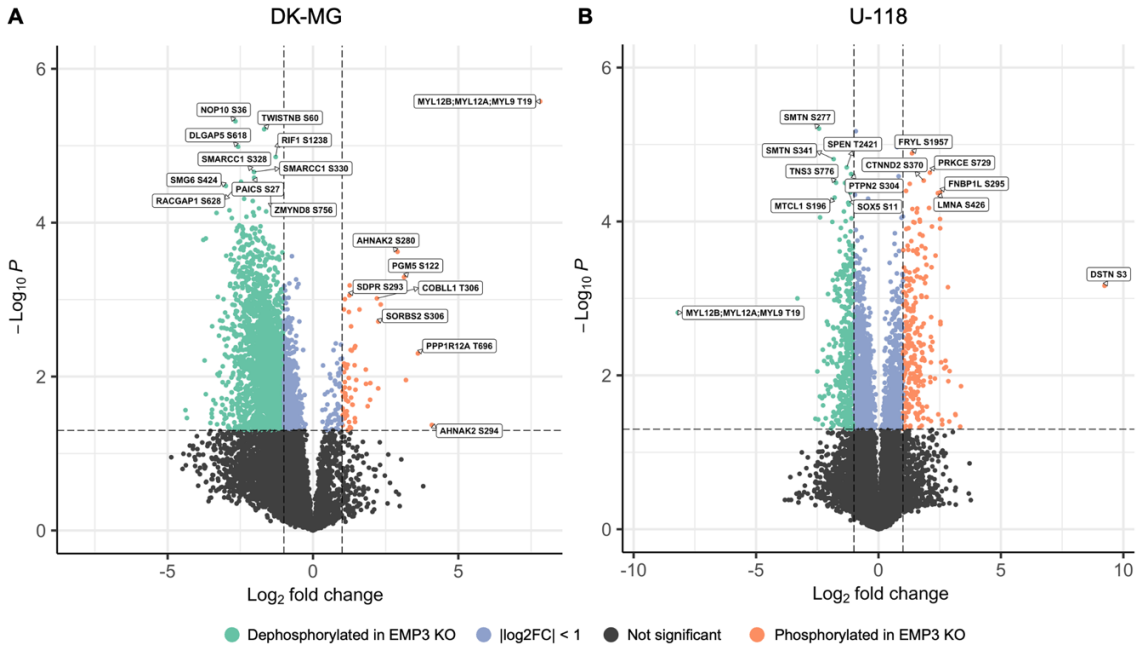

Figure 31. Volcano plots of differentially phosphorylated sites in DK-MG and U-118 EMP3 KOs. An absolute log_2-FC cut-off ≥ 1 and p-value cut-off ≤ 0.05 were used to identify phosphorylated (red) and dephosphorylated (green) phosphosites in DK-MG (A) and U-118 (B) EMP3 KOs vs. control. Phosphosites that did not satisfy the log_2-FC or p-value cut-offs are shown in purple and black, respectively.

To obtain further insight on the possible causes of these phosphosite changes, upstream pathway analysis using IPA was performed. Using the list of differentially regulated phosphoproteins along with their corresponding phosphorylation log_2-fold changes as input, IPA predicted a set of MRs that are activated or inhibited in EMP3 KOs relative to controls. Interestingly, immediate downstream effectors of EGFR were inhibited in DK-MG (e.g., CDK4/6, PIK3CA) and U-118 (e.g., AKT1, CDK2) EMP3 KOs (Fig. 32 A-B). These effectors, while involved in the same pathways, were not fully identical between the cell lines, suggesting cell type-specific rewiring of signaling networks in response to EMP3 KO.

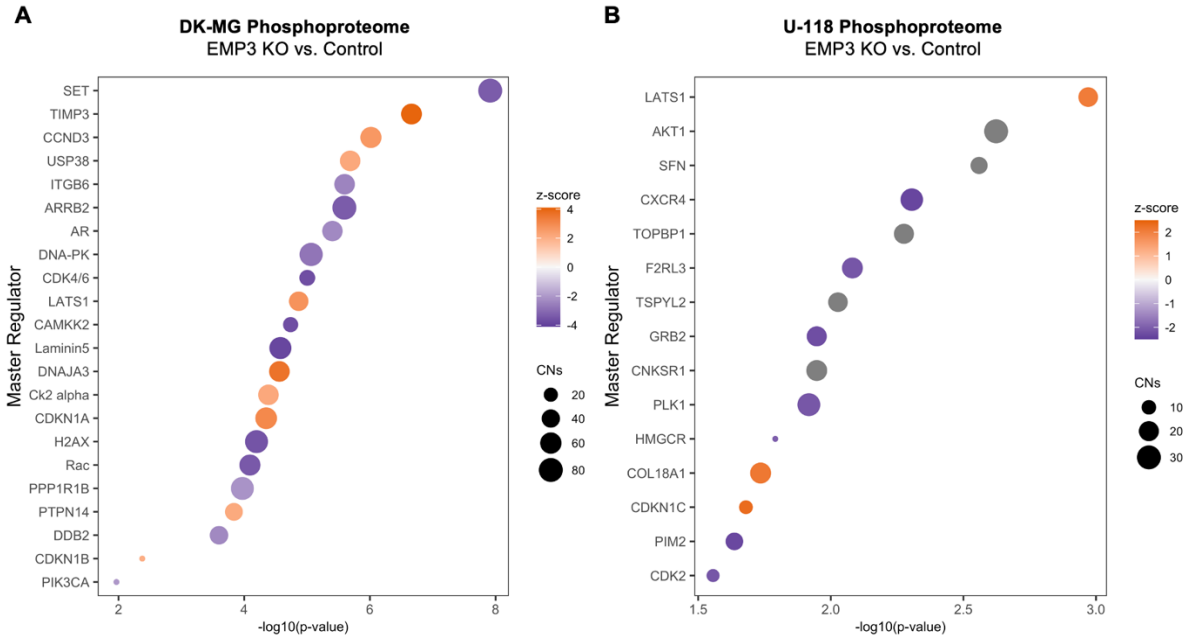

Figure 32. IPA analysis of the DK-MG and U-118 EMP3 KO phosphoproteomes. Dot plots showing activated and inhibited MRs based on the DK-MG (A) and U-118 (B) total phosphoproteomes. Color scale represents activation z-scores (activated – orange; inhibited – purple), while circle sizes represent number of associated causal networks (CNs) for each MR.

Restricting the analysis to proteins with commonly regulated phosphosites only, IPA also predicted dysregulation of various cell cycle regulators in both cell lines. These included activation of CDKN1C, a negative regulator of cell cycle progression; inhibition of the cyclin-dependent kinase CDK2, which promotes G1-to-S phase transition; and inhibition of CDC25B, which normally induces mitosis by facilitating G2-to-M phase transition (Fig. 33). Thus, EMP3 KO may lead to the inhibition of factors that normally induce cell cycle progression.

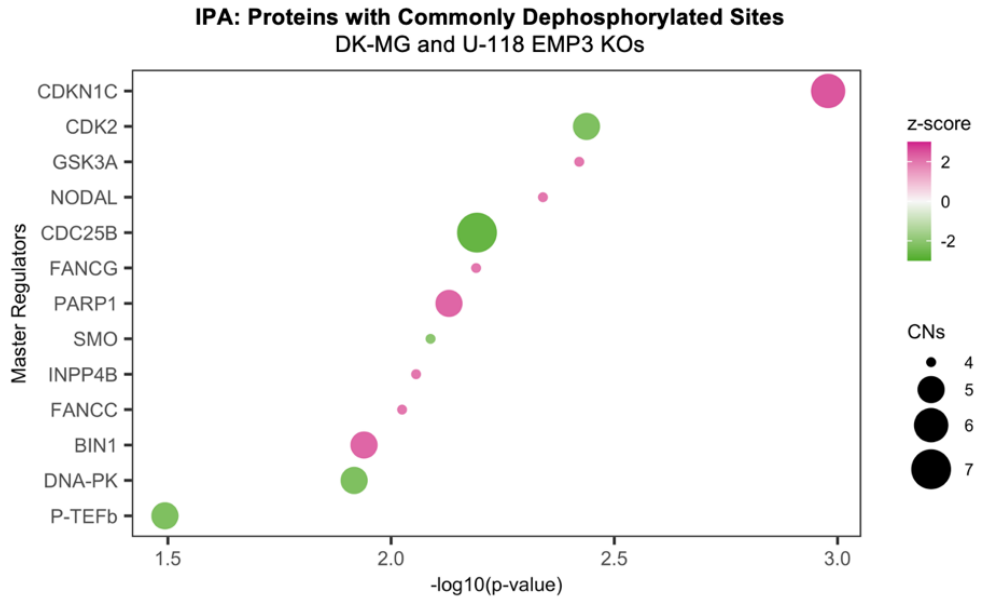

Figure 33. IPA analysis of proteins with shared dephosphorylations in DK-MG and U-118 EMP3 KOs. Dot plot showing activated and inhibited MRs based on proteins with commonly dephosphorylated sites in both EMP3 KO cell lines. Color scale represents activation z-scores (activated – magenta; inhibited – green), while circle sizes represent number of associated causal networks (CNs) for each MR.

To supplement the insights gained through IPA analysis, upstream kinase prediction using two independent bioinformatic tools, Kinase Enrichment Analysis (KEA) and Robust Inference of Kinase Activity (RoKAI), were also performed (79,82). For KEA, the input list was restricted to the 157 proteins with commonly dephosphorylated sites in DK-MG and U-118 cells, given that this tool is unable to consider quantitative measures of phosphorylation changes in the analysis. Using three different kinase-substrate databases, KEA consistently predicted CDK2 as the most significant upstream kinase responsible for the phosphorylation of most of the proteins in the input list (Fig. 34 A). Aside from CDK2, CDK1 was also consistently identified as top 2 hit in 2 out 3 of KS databases that KEA used in the analysis. Thus, CDK1/2 inhibition may underlie the shared dephosphorylation events in DK-MG and U-118 cells. Meanwhile, the EGFR effector AKT1 had the greatest number of dephosphorylated substrates when comparing all three kinase enrichment results, suggesting that AKT1 inactivation may also be shared feature of EMP3-depleted RTK II/CL-like cells. Other notable downstream RTK effectors predicted to be inhibited by KEA analysis include MAPK8, an intermediate serine-threonine kinase that resides between receptors and transcription factors in the RTK signaling cascade; and CDKs 4 and 6, cyclin-dependent kinases responsible for RB1 phosphorylation and subsequent cell cycle progression through the G1 phase.

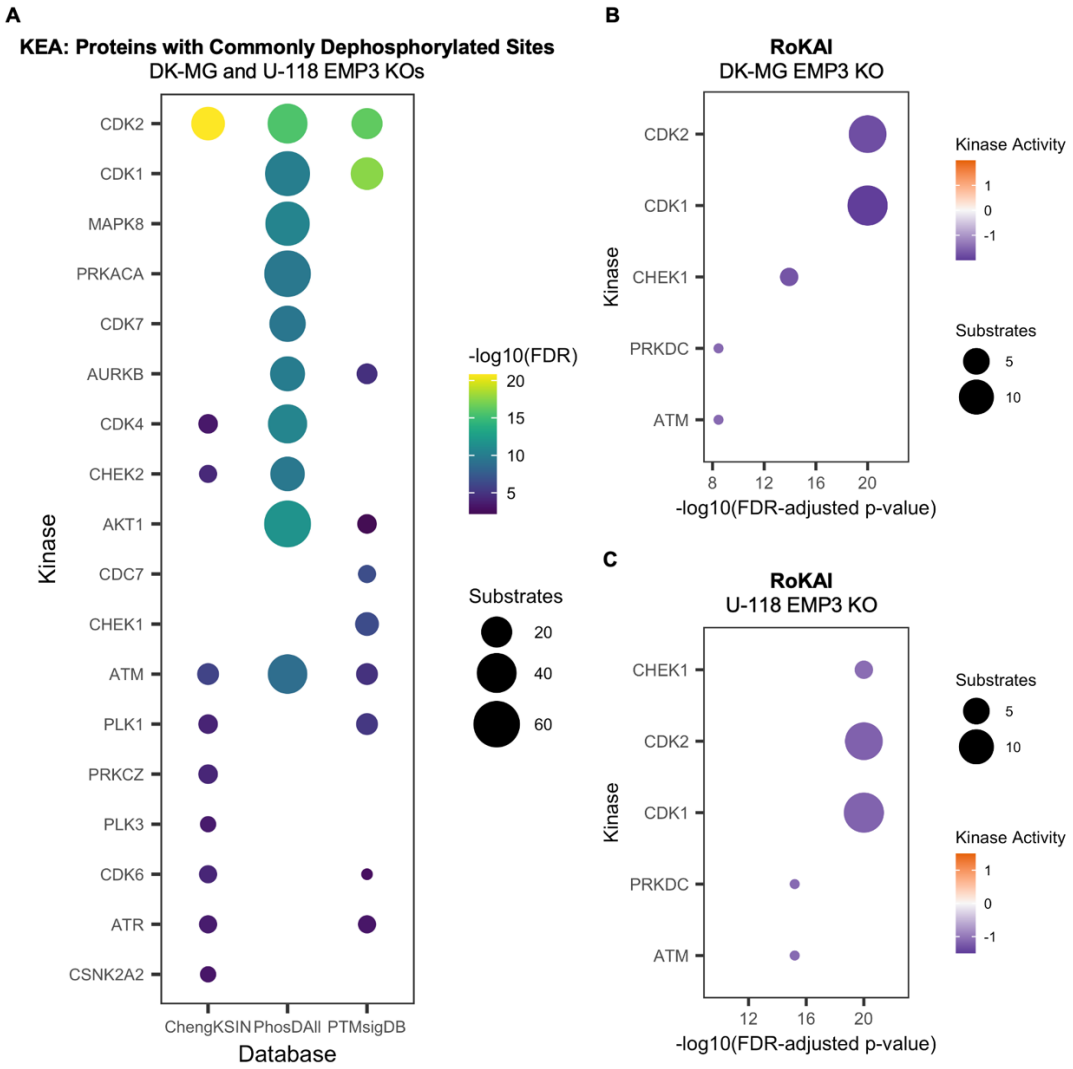

Figure 34. KEA and RoKAI analysis of commonly dephosphorylated proteins and phosphosites in DK-MG and U-118 EMP3 KOs. A) Dot plot showing top 10 significantly enriched upstream kinases in each kinase-substrate database as predicted by KEA. Color scale represents -log10(FDR-adjusted p-values), while circle sizes represent number of input substrates for each kinase. B, C) Dot plots showing top 5 significantly enriched upstream kinases based on common phosphosite changes in DK-MG (B) and U-118 (C) EMP3 KOs as predicted by RoKAI. Color scale represents kinase activity, while circle sizes represent number of input substrates for each kinase.

In contrast to KEA, RoKAI can provide a more granular analysis, as it includes both phosphosite identities and their quantitative measures in its identification of upstream kinases (82). Thus, for this tool, the list of commonly regulated proteins in DK-MG and U-118 cells along with the accompanying phosphosites and $\log_2$-fold changes were used as input. Interestingly, results still revealed a huge overlap with the previous IPA and KEA analyses, as CDK2 and CDK1 were predicted to be significantly inhibited in both DK-MG and U-118 cells (Fig. 34 B-C). Notably, the extent of CDK1/2 inhibition is observed to be greater in DK-MG cells, again highlighting the greater susceptibility of this cell line to EMP3 KO.

Taken together, pathway analysis and upstream kinase prediction of the phosphoproteomic data suggests that EMP3 KO induces inhibition of early EGFR effectors, which distally converges into inhibition of CDK1/2. This leads to the reduced phosphorylation of CDK1/2 substrates, which may potentially drive cell cycle arrest and reduce tumor cell proliferation.

4.4.5 EMP3 KOs have impaired mitogenic response to EGF and greater sensitivity to targeted EGFR inhibition

The multi-layered -omics and functional data generated in this study suggest that EGFR activity is compromised in RTK II/CL-like DK-MG and U-118 cells. To characterize how EMP3 KO-induced impairment of EGFR activity translates phenotypically, proliferation rates of DK-MG and U-118 control and EMP3 KO cells in both serum-containing and EGF-only conditions were measured. Results showed that DK-MG and U-118 EMP3 KO cells are less proliferative than controls when grown in media containing 10% FBS (Fig. 35 A-B). This is line with gene expression profiling and phosphoproteomics data indicating dysregulation of DNA replication and cell cycle processes in EMP3 KOs. Likewise, DK-MG and U-118 EMP3 KO cells grown in serum-free media supplemented with daily treatment of 100 ng/mL EGF for three consecutive days exhibited a blunted mitogenic response to the growth factor compared to the corresponding controls (Fig. 35 C-D). Thus, EMP3 KO-induced alterations in the EGFR-dependent transcriptome and phosphoproteome ultimately translate into defects in the ligand-dependent proliferation of RTK II/CL-like GBM cells.

As part of the lab's broader EMP3 project, a Bachelor's thesis student in the lab under my supervision, Natalie Bächle, also optimized multiple apoptosis assays to determine whether EMP3 confers resistance against generalized kinase inhibition by the apoptosis inducer staurosporine (STS). Her main results indicated that both DK-MG and U-118 EMP3 KOs have increased caspase 3/7 activity after treatment with 1 μM STS for 4 hours (Fig. 35 E-F). Thus, apart from arresting cellular proliferation, loss of EMP3 also makes RTK II/CL-like cells more susceptible to STS-induced cell death.

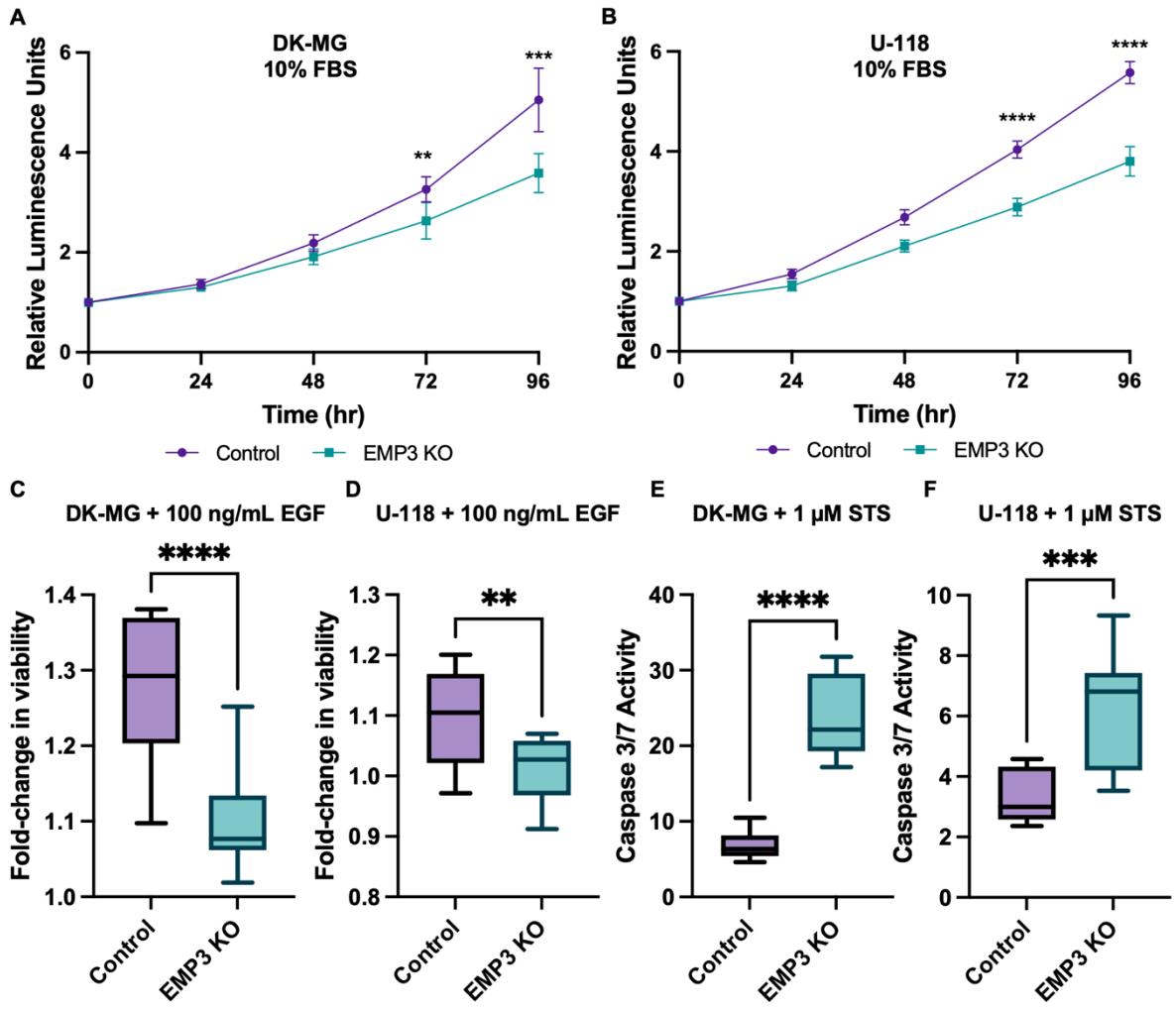

Figure 35. *In vitro* phenotypic assays indicate attenuation of cell proliferation and apoptosis resistance in DK-MG and U-118 EMP3 KOs. A, B) CellTiter-Glo® assays measuring proliferation rates of DK-MG (A) and U-118 (B) control and EMP3 KO cells grown in media with 10% FBS over the course of 96 hours. Mean relative luminescence units (RLU) correspond to fold-changes in ATP levels per day relative to Day 0 and are plotted as points. Error bars represent 95% confidence intervals. Results are representative of n=3 independent experiments. Unpaired t-test; **P<0.01, ***P<0.001, ****P<0.0001. C, D) Box plots showing mitogenic response of serum-starved DK-MG (C) and U-118 (D) control and EMP3 KO cells to daily treatment with 100 ng/mL EGF for 72 hours. The y-axis corresponds to the fold-change in ATP levels relative to untreated cells. Results are representative of n=3 independent experiments. Unpaired t-test; **P < 0.01, ****P < 0.0001. E,F) Box plots showing caspase 3/7 activity in STS-treated DK-MG and U-118 (F) control and EMP3 KO cells, as performed by Natalie Bächle. The y-axis corresponds to fold-changes in caspase 3/7 levels relative to untreated cells. Results are representative of n=3 independent experiments. Welch's t-test; ***P < 0.001, **** P < 0.0001.

To further assess the potential translational relevance of EMP3 inhibition, the differential sensitivity of EMP3 KOs and controls to targeted EGFR inhibition was assessed. To do so, U-118 control and EMP3 KO cells were treated with increasing concentrations of osimertinib (AZD9291) for 24 hours. Osimertinib is a brain-penetrant, third-generation EGFR inhibitor that is currently being explored as a potential therapeutic agent against GBM. Dose-response cell viability curves indicate that EMP3 KO increases the sensitivity of U-118 cells to osimertinib (Fig. 36 A). This was also reflected in the observed reduction in the half-maximal inhibitory concentration (IC_{50}) values in EMP3 KO cells (Fig. 36 B). Importantly, this effect

was reversed with stable re-introduction of EMP3 in EMP3 KOs (see Appendix Supplementary Fig. 10), confirming that increased sensitivity to osimertinib is indeed a specific effect of EMP3 depletion. Moreover, caspase 3/7 assays showed that 24-hour osimertinib treatment at a sub-IC_{50} level of 2.5 µM induced far greater apoptotic activity in EMP3 KOs vs. controls (Fig. 36 C). Again, this was rescued by re-expression of EMP3. Thus, RTK II/CL-like GBM cells may employ EMP3 to mediate therapeutic resistance against EGFR inhibitors.

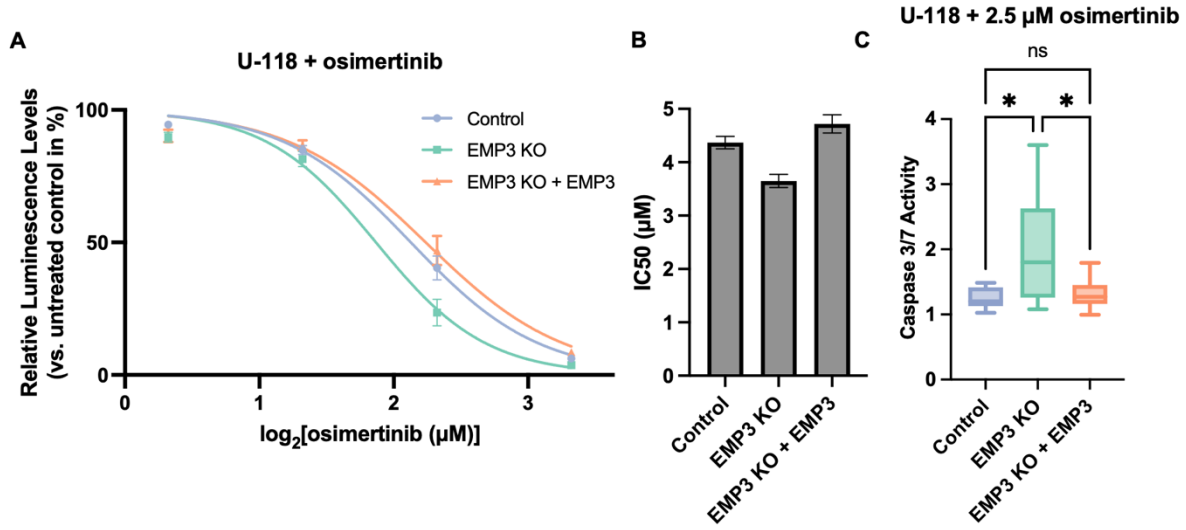

Figure 36. EMP3 KO synergizes with targeted EGFR inhibition by osimertinib in U-118 cells. A) Dose-response curve showing the viability of control and EMP3 KO cells with or without stable re-introduction of EMP3 after treatment with increasing concentrations of osimertinib for 24 hours. Mean fold-changes (in %) relative to untreated cells are plotted as points in the y-axis. Error bars represent SD across n=3 independent experiments. B) Bar plots showing the predicted IC_{50} values of osimertinib in the three cell lines. Error bars represent SEM across n=3 independent experiments. C) Caspase 3/7 activity of the three cell lines in response to 24-hour treatment with 2.5 µM osimertinib. Lines represent mean fold-changes in caspase 3/7 levels relative to untreated controls. Error bars correspond to SD across n=3 independent experiments. Welch's ANOVA with Dunnett's T3 multiple comparisons test; ns – not significant; *P < 0.05.

4.4.6 High EMP3 expression in TCGA GBMs correlates with increased expression of total and phosphorylated EGFR

To determine whether these *in vitro* findings can be reflected in the clinical setting, the association between EMP3 and EGFR expression in the TCGA GBM cohort was explored using the GlioVis portal (version 0.20) (67). Tumors were segregated into EMP3-high and -low groups using the median EMP3 expression level in the Agilent-4502A microarray as the cutoff. Proteins upregulated in the EMP3-high groups were then identified using the available reverse phase protein array (RPPA) protein measurements. RPPA is an antibody-based technique involving protein extraction from tumor samples followed by SDS denaturation and probing of target proteins imprinted on nitrocellulose slides (67,87). Upregulated proteins were defined as those having a RPPA score difference ≥ 0 between EMP3-high and -low groups.

Results showed that total and phosphorylated (Tyr1068 and Tyr1173) EGFR were among the top upregulated proteins in EMP3-high relative to EMP3-low tumors (Fig. 37 A-D). Again, these findings align with the biochemical, gene expression, and phosphoproteomic data showing the dependence of EGFR on EMP3 to maintain its stability and signaling.

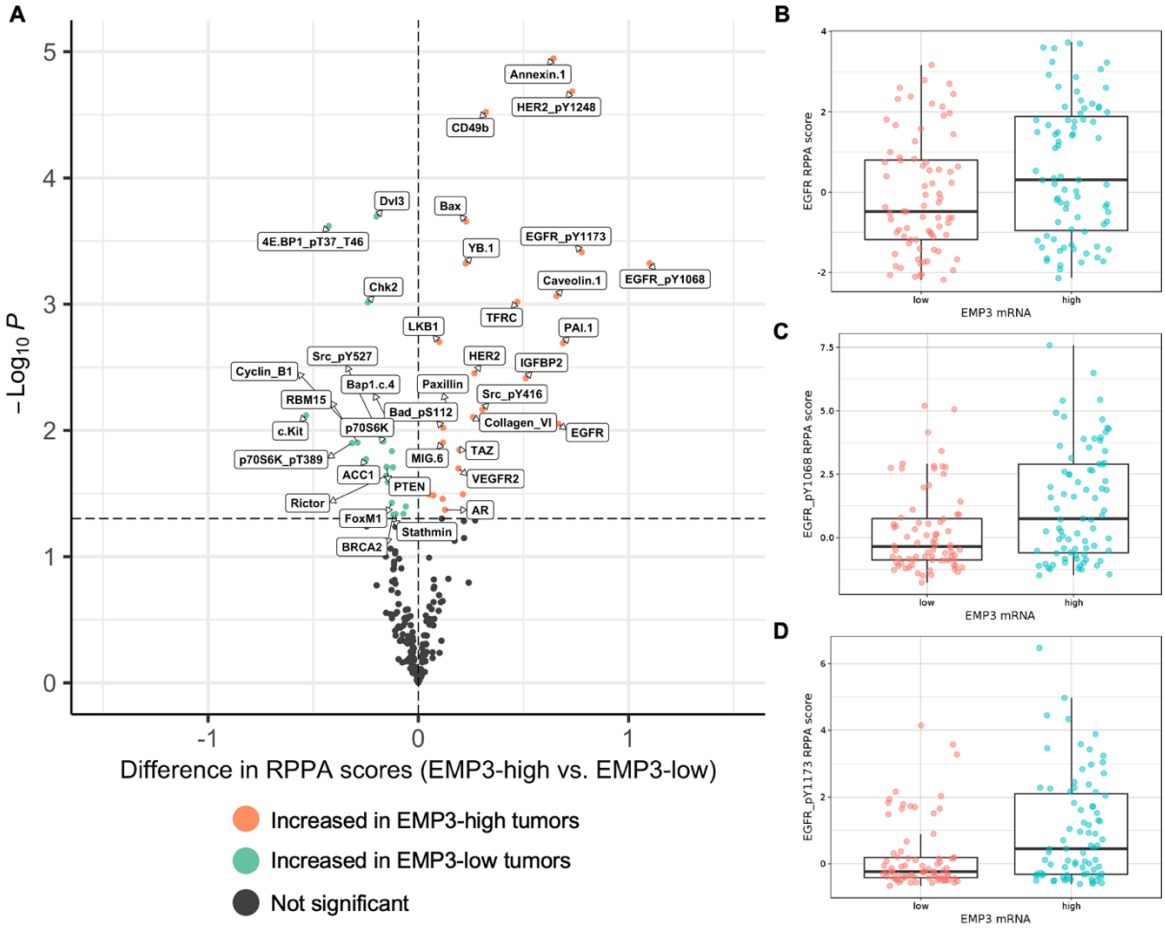

Figure 37. EMP3-high TCGA GBM tumors have higher EGFR and p-EGFR levels than EMP3-low tumors. A) Volcano plot depicting proteins that have higher abundance in EMP3-high (red) vs. EMP3-low tumors (green). Median EMP3 expression based on the Agilent-4502A microarray data was used as the cutoff to separate EMP3-high from EMP3-low tumors. A p-value cutoff ≤ 0.05 was used to identify proteins with significant differences between RPPA scores. Proteins that do not pass the p-value cutoff are colored black. B-D) Box plots showing levels of total EGFR (B), Tyr1068-phosphorylated EGFR (C), and Tyr1173-phosphorylated EGFR (D) in EMP3-high vs. EMP3-low IDH-wt GBMs. Figures were obtained from the GlioVis portal version 0.20 (http://gliovis.bioinfo.cnio.es/, accessed 09 July 2022).

4.5 EMP3 facilitates the assembly of CD44s-MET signaling complexes in mesenchymal-like LN-18 GBM cells

The LN-18 cell line expresses the mesenchymal marker CD44 at a higher level than RTK II/CL-like cells, making LN-18 a more suitable cellular model for investigating the role of EMP3 in MES-like GBMs. Because EMP3 is known to form a direct and stable interaction complex with CD44s in this cell line, I sought to further characterize the EMP3-CD44s interaction and investigate the possible regulatory effects that EMP3 might have on CD44s in the context of MES-like GBM cells.

4.5.1 Truncation mutagenesis putatively identifies CD44s domains required for EMP3 interaction

CD44s possesses several structural domains that may mediate its interactions with its binding partners. These domains include 1) a globular N-terminal extracellular domain bearing hyaluronan-binding motifs; 2) a stem structure that is often glycosylated and may mediate growth factor interactions in the presence of variant exons; 3) a transmembrane region critical for membrane localization; and 4) a C-terminal intracellular domain (ICD) that binds to cytoskeletal regulators and signaling adaptors including the ezrin, radixin, moesin (ERM) protein family (88,89). To determine which of these domains may be directly interacting with EMP3, plasmid constructs encoding serially truncated versions of CD44s tagged with FLAG at the C-terminal ends were cloned and expressed in LN-18 cells. The expressed constructs included 1) full-length CD44s as the positive control; 2) CD44s ΔNTD, which does not contain the N-terminal domain; 3) CD44s ΔNTD-stem, which only contains the transmembrane segment and the ICD; and 4) the CD44s ICD only (Fig. 38 A). Western blotting of eluates resulting from FLAG pull-downs revealed that all the truncated proteins did not co-immunoprecipitate with EMP3 (Fig. 38 B), indicating that only the full-length version of CD44s is able to interact with EMP3 or that the N-terminal globular domain is responsible for the interaction. Because it was not possible to express the N-terminal domain alone, this study was unable to distinguish between those two possibilities. Regardless, the CD44s stem structure, transmembrane region, and the cytoplasmic tail can be ruled out as sufficient for the CD44s-EMP3 interaction.

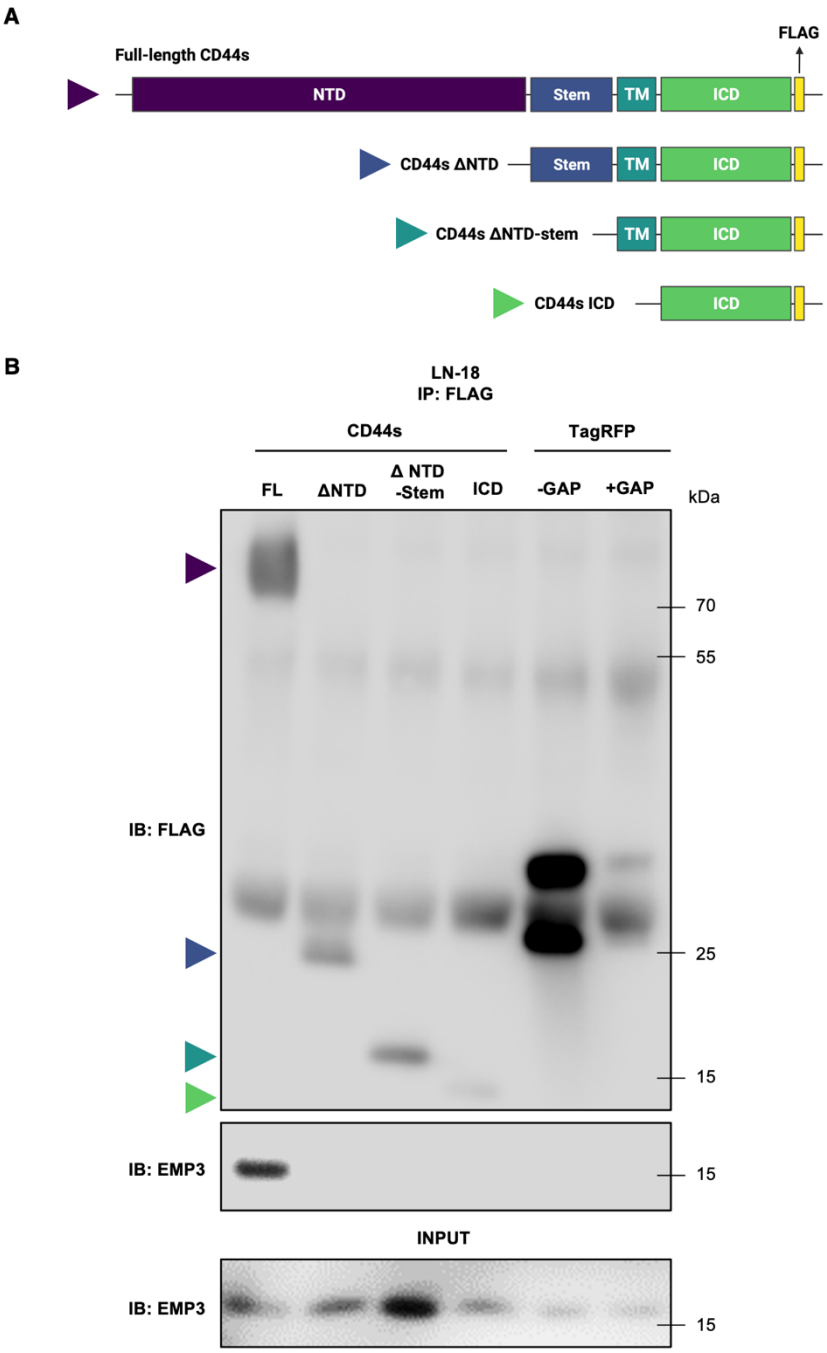

Figure 38. FLAG pull-downs of serially truncated CD44s-FLAG proteins revealed that EMP3 only physically associates with full-length CD44s. A) Schematic diagram showing serially truncated CD44s plasmids used in the pull-down experiments. B) Western blotting showing successful pull-down of full-length and truncated CD44s-FLAG proteins. EMP3 co-immunoprecipitated with full-length CD44s only. Results shown are representative of n=2 independent experiments.

4.5.2 The CD44-EMP3 complex exclusively interacts with MET and Rho GTPase/RAC1 effectors in LN-18 cells

To characterize the subcellular context in which the CD44-EMP3 complex could operate in within MES-like LN-18 cells, the LN-18 BioID2 data was re-examined to identify proteins that may directly associate with both EMP3 and CD44. This mesenchymal CD44-EMP3 subnetwork was generated by identifying EMP3 WT and N47A interactors that are also functionally or physically associated with CD44 within two neighboring distances based on STRING (version 11.5). EMP3 N47A hits were included to encompass all possible CD44-EMP3 interactors, given that the CD44-EMP3 interaction appears to be glycosylation-independent. Additionally, hits identified in the parallel U-118 BioID2 screen were excluded to ensure the network's mesenchymal specificity. This mapping approach revealed a well-connected network of EMP3-and CD44-interacting membrane proteins that are enriched for Rho GTPase signaling effectors (e.g., ROCK1, ROCK2), RAC1 targets (e.g., PAK1, PAK4), and mesenchymal RTKs (e.g., MET, PDGFRB) (Fig. 39). Thus, the CD44-EMP3 complex appears to mainly reside in areas of the plasma membrane marked by the presence of mesenchymal receptors and their downstream effectors.

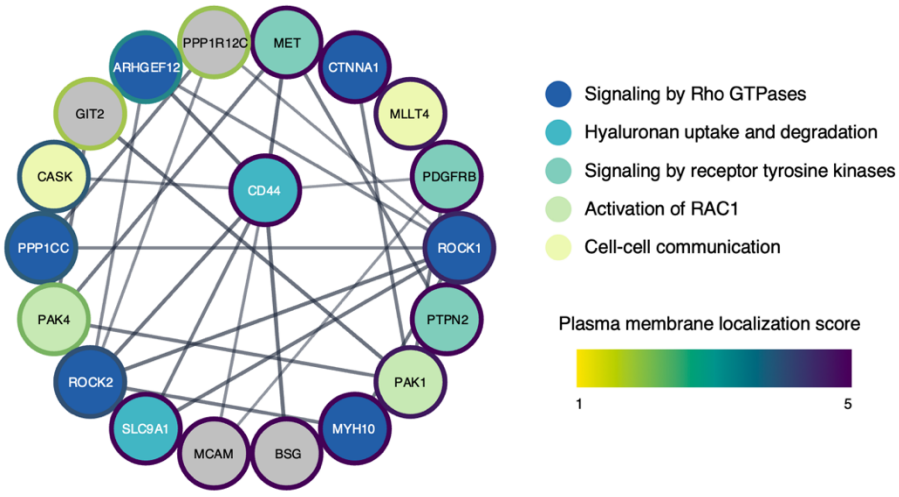

Figure 39. A mesenchymal CD44-EMP3 subnetwork exclusively found in LN-18 cells. The STRING interaction network depicts EMP3 interacting partners that are also functionally or physically associated with CD44 within two neighboring distances. Only edges with STRING scores ≥ 0.700 and nodes with degrees ≥ 2 were included in the final network. Plasma membrane localization scores are color-mapped onto the node borders. Node borders indicate plasma membrane localization scores.

4.5.3 Loss of EMP3 abolishes complex formation between CD44s and MET

The BioID2 data suggests that EMP3 may play a role in the formation of signal transduction complexes in the plasma membrane of MES-like LN-18 cells. To provide a proof-of-principle of this hypothesis, I examined the possible effects of EMP3 KO on complex formation between the novel EMP3 interactors CD44s and MET. To do so, CD44s-FLAG proteins were expressed in LN-18 control and EMP3 KO cells, and FLAG pull-downs were performed. Immunoblotting of the FLAG pull-down eluates showed that CD44s, but not the TagRFP controls, co-immunoprecipitated with EMP3 and MET (Fig. 40 A). Notably, both the mature membrane-localizing 140 kDa form of MET and to a lesser extent, the ER-localizing single-chain 170 kDa precursor co-immunoprecipitated with CD44 and EMP3. More importantly, loss of EMP3 abrogated the co-immunoprecipitation of CD44s and MET, indicating that EMP3 is required for the CD44s-MET interaction.

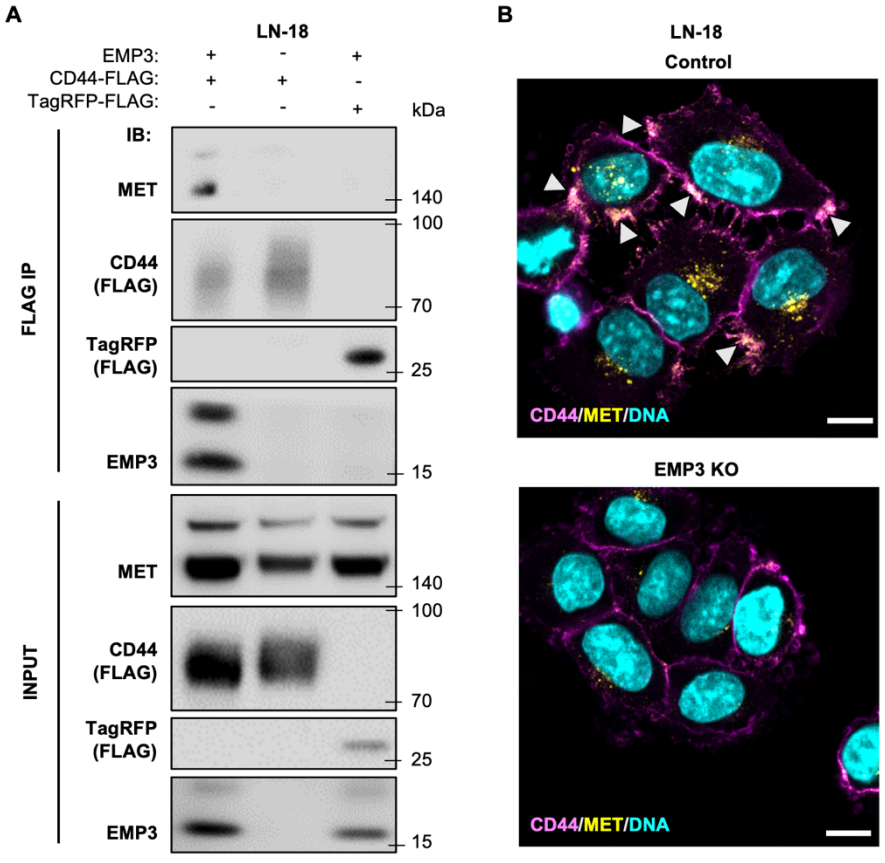

Figure 40. EMP3 is required to maintain CD44s-MET complexes on the plasma membrane. A) Western blotting demonstrating co-immunoprecipitation of CD44s-FLAG, EMP3, and MET in LN-18 control cells only. TagRFP-FLAG was also pulled down to confirm that the interactions are specific to CD44s and not the FLAG tag. Results are representative of n=2 independent experiments. B) IF staining of CD44 and MET in LN-18 control and EMP3 KO cells. Nuclei were stained with DAPI. Scale bar = 10 µm. Results are representative of n=2 independent experiments.

The existence of an EMP3-dependent CD44s-MET complex was further substantiated by immunofluorescence (IF) experiments, which showed the presence of co-localizing CD44 and MET signals in the plasma membrane of EMP3-expressing, but not EMP3 KO, cells (Fig. 40 B). However, no intracellular co-localization of CD44 and MET was detected by IF in EMP3-expressing cells, suggesting that the observed interaction between CD44s-FLAG and the 170 kDa MET precursor may be artificial and may have occurred after cell lysis. Moreover, IF images showed that in EMP3 KO cells, CD44s is still present in the cell surface, while the MET signal was virtually absent in the membrane and noticeably reduced in the perinuclear region. This staining pattern suggests significantly reduced MET expression or stability in EMP3 KOs, although this is not strongly supported by the MET blots (Fig. 40A). Collectively, both the FLAG pull-downs and IF experiments indicate that EMP3 associates with the membrane-localized CD44s-MET complex, and that EMP3 depletion abolishes the formation of this complex presumably through reduced membrane targeting of MET.

4.5.4 Cell surface proteome profiling confirm reduced membrane expression of MET upon EMP3 depletion

The previous experiments strongly point to a possible generalized role of EMP3 in membrane targeting and/or receptor organization in MES-like GBM cells. To identify other proteins that may be similarly regulated by EMP3 in an unbiased manner, mass spectrometry analysis of the cell surface proteome of LN-18 control and EMP3 KO cells was also performed. This approach relied on the selective labeling of membrane proteins with Sulfo-NHS-SS-biotin, a thiol-cleavable and amine-reactive form of biotin that can be incubated with live cells to initiate cell surface biotinylation (Fig. 41 A). After the labeling period, biotinylated membrane proteins were selectively purified by streptavidin pull-downs and submitted to the MS-based Protein Analysis Unit for mass spectrometry analysis. Afterwards, I further processed the resulting list of identified proteins by filtering for proteins with 1) highly probable membrane localization (i.e., plasma membrane COMPARTMENTS score ≥ 4) and 2) altered membrane abundance upon EMP3 KO (i.e., absolute $\log_2$-FC ≥ 0.50; Welch's t-test p-value ≤ 0.05). A relaxed $\log_2$-FC cutoff was particularly applied to detect proteins with subtle changes in membrane expression levels. This analysis pipeline revealed 24 membrane proteins whose membrane localization is altered upon EMP3 depletion (Fig. 41 B). Notably, only 1 protein (NRP1) was differentially abundant in a parallel proteomic screen, suggesting that all the other observed changes are strictly due to changes in membrane localization instead of protein abundances.

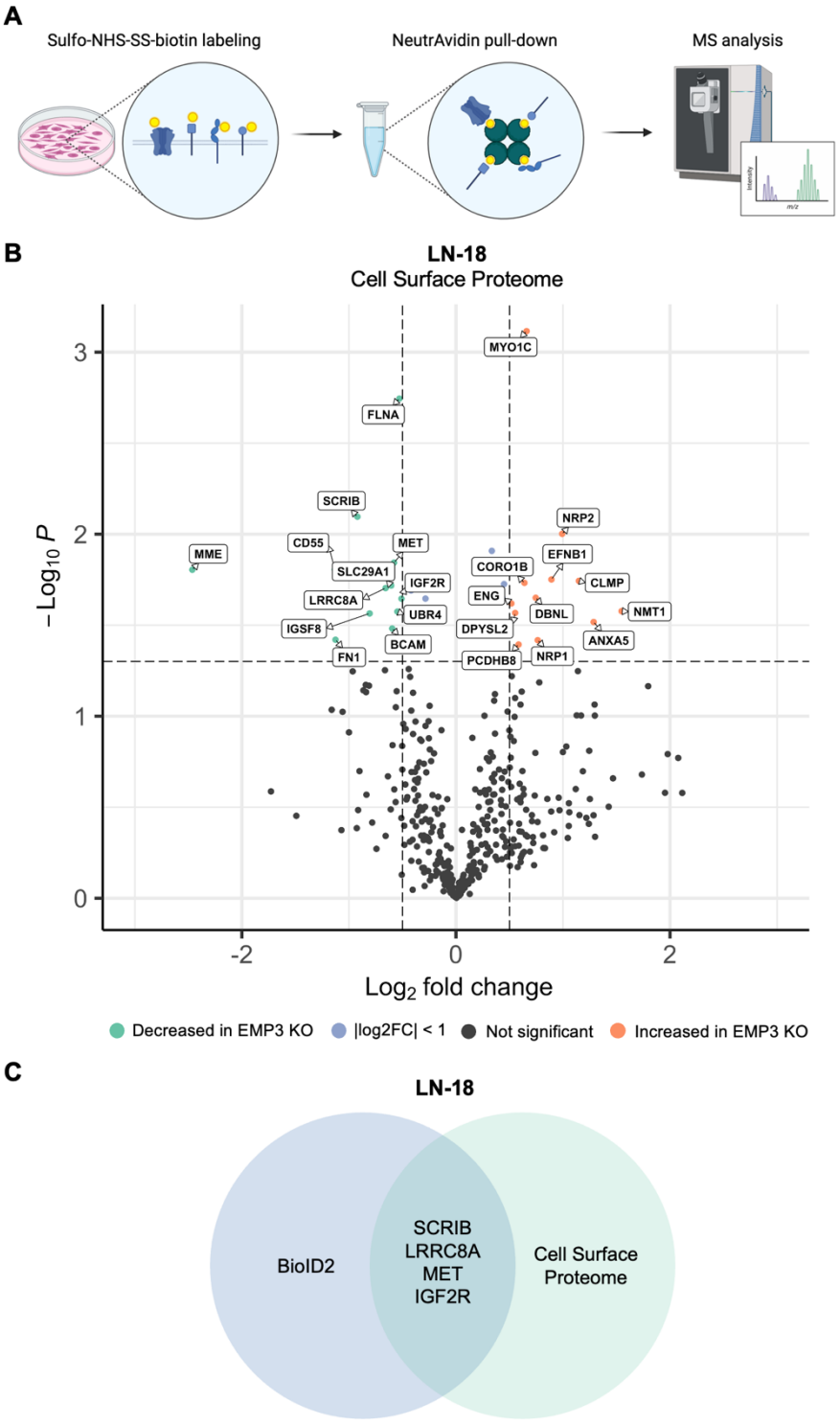

Figure 41. Mass spectrometry-based analysis of the cell surface proteomes of LN-18 control and EMP3 KO cells. A) Workflow for MS-based cell surface proteome analysis. Figure was created using BioRender.com. B) Volcano plots depicting differential abundance of membrane proteins in LN-18 control and EMP3 KOs. An absolute $\log_2$-FC cut-off ≥ 0.5 and p-value cut-off ≤ 0.05 were used to identify proteins with increased (red) and decreased (green) membrane localization in EMP3 KOs. Proteins that did not pass the $\log_2$-FC and p-value cutoffs are colored in purple and black, respectively. C) Venn diagram showing the overlap of the hits obtained from the LN-18 BioID2 and cell surface proteome screens.

Intersection of the cell surface proteome screen with the previous LN-18 BioID2 screen revealed four common hits, all with reduced membrane expression upon EMP3 KOs: protein scribble homolog (SCRIB), volume-regulated anion channel subunit (LRRC8A), MET, and IGF2R (Fig. 41 C). Strikingly, CD44 was not identified as a hit in the cell surface proteome screen. This is consistent with the previous IF experiment that showed reduced membrane expression of MET but not of CD44. Thus, while EMP3 has a minimal effect on the cell surface proteome of LN-18 cells, it appears to be important for the membrane targeting of a small subset of proteins, most notably the mesenchymal receptor and EMP3/CD44 interactor MET.

4.5.5 EMP3 KO impairs CD44 and MET oncogenic signaling

To test whether EMP3 can modulate the downstream oncogenic signaling of either member of the CD44s-MET complex, proliferation assays were performed with serum-starved LN-18 control and EMP3 KO cells treated daily with 100 µg/mL of the CD44 ligand hyaluronic acid (HA) or 100 ng/mL of the MET ligand hepatocyte growth factor (HGF) for 72 hours. Results showed that EMP3 KO cells have significantly dampened mitogenic response to both HA (Fig. 42 A) and HGF (Fig. 42 B). Moreover, as demonstrated by Natalie Bächle, EMP3 KO cells exhibited a greater increase in caspase 3/7 activity compared to control cells upon STS treatment (Fig. 42 C). Thus, reduction of MET membrane expression and abrogation of CD44s-MET complex formation in LN-18 EMP3 KO cells correlate with impaired HA- and HGF-induced cell proliferation and increased susceptibility to apoptosis.

Additionally, to characterize signaling defects caused by EMP3 KO in LN-18 cells, microarray hybridization and upstream pathway analysis was performed as previously described for RTK II/CL-like cells. Because a second MES-like EMP3 KO cell line was not available at the time of analysis, an additional LN-18 EMP3 KO cell line generated using a different guide RNA (provided by Dr. Arne Christians; see Appendix Supplementary Fig. 11) was used to identify high-confidence transcriptomic alterations specific to EMP3 KO. Using commonly regulated DEGs between the two LN-18 EMP3 KO cell lines as input, IPA predicted CD44 to be among the top inhibited master regulators in the two LN-18 EMP3 KO cell lines (Fig. 42 D). Moreover, downstream MET effectors like ERK and MAPK1 were also predicted to be slightly inhibited based on the DEG list. Interestingly, IQGAP1, a protein involved in Rho GTPase and RAC1 signaling, also exhibited a negative activation z-score. Collectively, these results are consistent with impaired CD44 and MET downstream signaling in LN-18 EMP3 KOs.

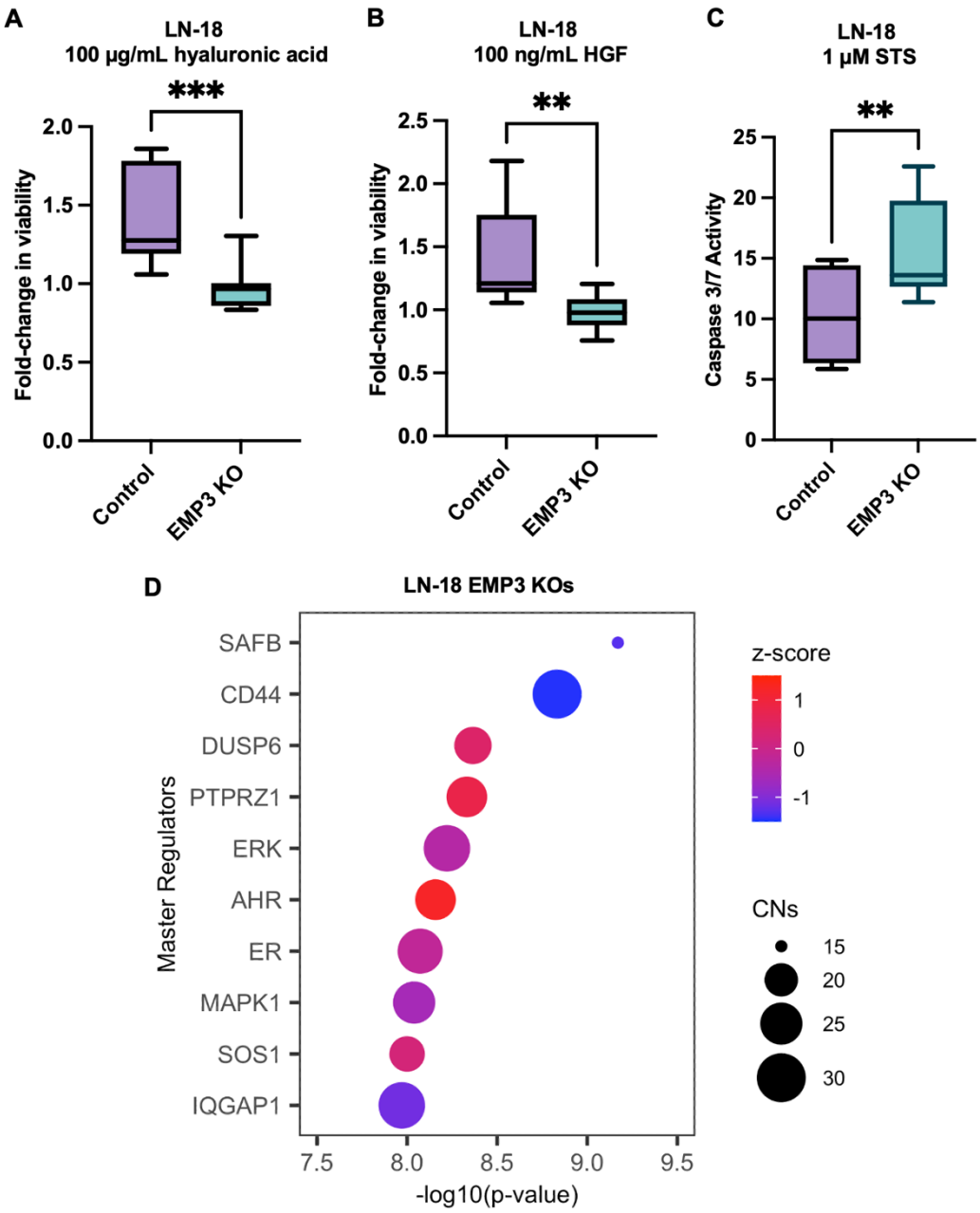

Figure 42. EMP3 KO impairs downstream CD44 and MET signaling. A, B) Box plots showing the mitogenic response of serum-starved LN-18 control and EMP3 KO cells to daily treatment with 100 µg/mL HA (A) or 100 ng/mL HGF (B) for 72 hours. The y-axis corresponds to the fold-change in ATP levels relative to untreated cells. Results are representative of n=3 independent experiments. Welch's t-test; **P < 0.01, ***P < 0.001. C) Box plots showing caspase 3/7 activity in STS-treated LN-18 control and EMP3 KO cells, as performed by Natalie Bächle. The y-axis corresponds to fold-changes in caspase 3/7 levels relative to untreated cells. Results are representative of n=3 independent experiments. Unpaired t-test; **P < 0.01. D) Dot plots showing inhibited master regulators (MRs) in LN-18 EMP3 KOs. Color scale corresponds to activation z-scores (red – activated; blue – inhibited), while circle sizes indicate the number of associated causal networks (CNs) for each MR.

5 Discussion

5.1 The EMP3 interactome

5.1.1 EMP3's core interaction network

Previously, a yeast-two-hybrid (Y2H) screen identified novel interacting partners of EMP3, majority of which localize in the plasma membrane or in endocytic vesicles and are involved in protein trafficking (45). Several of these interactors were validated by orthogonal methods, allowing the researchers to confidently hypothesize about EMP3's possible involvement in membrane organization and receptor trafficking events. However, the study was limited in that the identified hits were only restricted to the coding sequences (CDS) present in the Gateway prey library (The GPCF Gateway Full ORF Clone collection was a gift of the GPCF Vector and Clone Repository). Moreover, the top interactors were confirmed only in the context of non-glioma cell lines, and further functional validation of the proposed hypotheses was not performed. Thus, prior to this study, the subcellular context in which EMP3 operates in and its exact function in IDH-wt GBM remained to be elucidated.

To solve this problem and to define EMP3's interactome in a comprehensive and unbiased manner, I utilized BioID2-based proximity labeling coupled to mass spectrometry analysis. This approach has several advantages over other commonly used approaches to screen for protein-protein interactions (PPIs). Notably, BioID2 can generate a historical record of *in situ* PPIs in a quantitative and highly sensitive manner (83,90). This method, therefore, is very much suitable for mapping the interactome of a putative trafficking protein like EMP3. Indeed, with BioID2, this study was able to build upon the previous Y2H screen and identify a greater number of novel, putative EMP3 interactors in two molecularly distinct GBM cell lines. Majority of these interactors, with the exception of CD44, were not identified in a parallel AP-MS screen that relied on co-immunoprecipitation of interacting partners after cell lysis, highlighting BioID2's unique ability to identify even very weak or transient interactions *in situ.*

In line with the previous Y2H screen performed by Christians et al. (45), the newly discovered EMP3 interactors were enriched for both membrane proteins and trafficking regulators. At the membrane, EMP3 appears to interact with several receptors important for GBM oncogenic signaling, including RTKs (e.g., EGFR, MET, PDGFRB), integrins, and receptors involved in the Hippo-Merlin signaling pathway (e.g., CD44, EPHA2). Notably, majority of these

receptors are known to reside in lipid rafts – highly compartmentalized membrane microdomains marked by high concentrations of signaling molecules (91–94). This observation supports a previous hypothesis that suggested a possible role of EMP3 in the organization and/or clustering of raft-resident membrane receptors (45). Indeed, as proof-of-hypothesis, I demonstrated how EMP3 KO abrogates the formation of a signaling complex between the mesenchymal GBM receptors CD44 and MET (see Section 5.2.2). Further studies are necessary to systematically define other receptor dimerization or clustering events that may be similarly regulated by EMP3.

On the other hand, the intracellular protein complexes identified by BioID2 mapped EMP3's movement through several trafficking routes. Particularly, the findings suggest that EMP3 may be internalized within clathrin-coated vesicles (CCVs), cycle from endosomes to the trans-Golgi network (TGN) via retromer-dependent retrograde transport, or alternatively recycle back to the membrane through EARP-positive endosomes. This high-resolution map of EMP3's movement inside the cell sheds further light on the possible trafficking pathways that may be traversed by and/or actively regulated by this tetraspanin. Within the scope of this study, it was demonstrated that EMP3 restricts EGFR trafficking into late endosomes, most likely by cooperating with the novel EMP3 interactor and retromer component TBC1D5 (see Section 5.2.1). Future mechanistic studies should dig deeper into the other regulatory functions that EMP3 might exert on the other trafficking routes mentioned above. Moreover, it will be important to pinpoint other GBM-relevant receptors aside from EGFR whose trafficking might also be influenced by EMP3.

5.1.2 Impact of cell identity and glycosylation on the EMP3 interactome

The BioID2 experimental design employed here also allowed this study to assess the impact of cellular identity and glycosylation on the EMP3 interactome. Between the two factors, cell identity appears to have a stronger impact, as multiple clusters of cell type-specific interactors were identified in both U-118 and LN-18 cells. This is not surprising, given that previous studies have shown how PPI networks can undergo context-dependent reorganization in different cell and tissue types (95,96). Specifically, the U-118 BioID2 screen uniquely yielded several mitochondrial-localizing proteins involved in oxidative phosphorylation, as well as proteins involved in OST-mediated glycosylation (e.g. DDOST). The former indicates a possible mitochondrial function for EMP3 in RTK II/CL GBMs, while the latter aligns well with Western blotting experiments showing greater EMP3 glycosylation in U-118 versus LN-

18 cells. Additionally, several proteins involved in bidirectional ER-to-Golgi anterograde and Golgi-to-ER retrograde transport appears to interact with EMP3 exclusively in U-118 cells. Subtle differences can even be observed within the EMP3 core interactome, with retromer components (e.g., TBC1D5, SNX2) garnering higher BioID2 enrichment scores in U-118 versus LN-18 cells. On the other hand, the LN-18 screen uniquely yielded mesenchymal receptors (e.g., MET, PDGFRB), as well as a subnetwork of proteins involved in Rho GTPase and RAC1 signaling. This suggests that in MES-like cells, EMP3 may be more involved in epithelial-to-mesenchymal transition, cytoskeletal remodeling, and/or the induction of cell migration and invasion. This cell type-specific rewiring of the EMP3 interactome may exist to fine-tune EMP3 function and to allow EMP3 to exert slightly different pro-tumorigenic functions in RTK II/CL/AC-like and MES-like cells. Indeed, this is supported by -omics data generated in this study, which showed cell type-specific signaling defects upon EMP3 KO.

On the other hand, glycosylation appears to have a minimal impact on EMP3's core interactome, as there was a huge overlap between EMP3 WT and N47A BioID2 hits. While both glycosylated and non-glycosylated EMP3 interact with the same partners, this study has not been able to rule out a possible effect of EMP3 glycosylation on the activity of these interactors. Protein glycosylation has been shown to mediate various aspects of cancer biology, ranging from signal transduction to intercellular interactions (97). For example, it may be possible for glycosylated EMP3 to sequester ligands and deliver these to partner RTKs, similar to how glycan modifications in MET improves accessibility to HGF (98). Alternatively, glycosylated EMP3 may differentially regulate lateral membrane organization and/or facilitate receptor interactions, as has been shown for glycoprotein-dependent clustering of integrins (99). Further mechanistic investigations will certainly be needed to assess how glycosylation affects EMP3 and its intra- and inter-cellular interacting partners.

Meanwhile, comparative analysis of the EMP3 WT and N47A interactome exclusively found in U-118 cells—which exhibit higher levels of glycosylated EMP3 than LN-18 cells— revealed more striking differences and additional insights on this PTM. In U-118 cells, the SRP/OST complex, as well as proteins involved in ER-to-Golgi anterograde transport and membrane delivery, appear to preferentially interact with glycosylated EMP3. These complexes are typically associated with nascent membrane protein synthesis (100–102); thus, glycosylated EMP3 may simply represent newly synthesized pools of EMP3 that have yet to undergo *N*-glycan trimming and ER exit. Previous studies have noted how glycosylation of nascent

proteins could be important for proper folding and membrane targeting (102). Still, because the N47A mutant appears to localize in the membrane and even interact with various membrane proteins, it is unlikely for EMP3 glycosylation to be essential for these processes. Thus, with respect to protein synthesis, quality control, and plasma membrane delivery, the N47 glycan is most likely inconsequential and is just a by-product of the close association between newly synthesized EMP3 and the glycosylation machinery.

Interestingly, the U-118 BioID2 data also hints at a preferential interaction between glycosylated EMP3 and mitochondrial proteins involved in calcium ion and respiratory electron transport (e.g., PHB, PHB2, ATP5I, ATP5C1, ATP5A1). Glycan modifications have been previously shown to regulate the mitochondrial localization of eukaryotic protein isoforms. For example, in yeast, abrogation of *N*-glycosylation with tunicamycin treatment abolished the mitochondrial localization of certain glycoproteins (103). In contrast, ATP synthase subunit α, which normally localizes in the mitochondria, has been shown to traffic to the plasma membrane of neural cells as a glycosylated isoform (104). In the case of EMP3, the N47 glycan—while dispensable for membrane trafficking—may be responsible for preferentially directing the protein towards the inner mitochondrial membrane. Further experiments will be necessary to validate this hypothesis as well as to elucidate the possible molecular function of EMP3 in the mitochondria.

5.2 EMP3 fulfills multiple oncogenic functions in a cell type-specific manner

This work, in line with previous studies, point towards EMP3 being a moonlighting protein. Moonlighting proteins are defined as proteins with multiple context-dependent functions that differ depending on their spatiotemporal context (105). These moonlighting functions typically arise when there is a 1) post-translational modification, 2) change in the cell type or timing of protein expression, 3) change in interaction partners, or 4) change in subcellular localization (105). In GBM, EMP3 appears to be primed to have moonlighting ability, as it easily fulfills these four conditions. EMP3 1) can be glycosylated (45), 2) is expressed in two different GBM cellular states (i.e., AC-like and MES-like cells) (42), and as shown by the BioID2 screens performed in this study, 3) has multiple interaction partners and 4) is multi-localizing. The last two conditions are also supported by other studies, which have shown EMP3's ability to interact with multiple membrane receptors (e.g., RTKs, TGFBR2, CD44, etc.) and localize in different cellular compartments (42,50,66). Also supporting the existence of cell type-specific

functions, EMP3's regulatory effect on TGFBR2 was shown to be specific to CD44-high GBM cells only (66).

To further understand how GBM subtype could rewire EMP3's function, it was necessary for this study to obtain and characterize EMP3 KO cellular models that mimic either EMP3-expressing subgroup. For the purpose of cell type classification, I found transcriptomic analysis coupled with CD44 marker expression to be sufficient, as it allowed proper segregation and classification of the adherent GBM cells into either RTK/CL-like or MES-like states. On the other hand, methylation analysis failed to classify the cellular models in the same manner, presumably because it is better suited for cells or tissues freshly derived from patients. Regardless, by applying biochemical, transcriptomics, and proteomics approaches on the EMP3 KO cell lines, this study has uncovered novel GBM cell type-specific functions of EMP3. Specifically, RTK II/CL-like DK-MG and U-118 cells appear to depend on EMP3 to sustain EGFR signaling, while MES-like LN-18 cells rely on EMP3 for the membrane organization of the mesenchymal receptors CD44 and MET. These two distinct mechanisms are discussed in further detail in the succeeding sections.

5.2.1 EMP3 – a regulator of EGFR trafficking and signaling in RTK II/CL-like cells

Past investigations on EMP3 have shown that it may regulate EGFR activity in non-glioma cells. EMP3 depletion by shRNA is known to reduce total and/or phosphorylated EGFR levels and inhibit EGFR's downstream effectors in several cellular contexts (45,61,62). Christians et al. further proposed that these effects may be due to EMP3's putative trafficking function, given than EMP3 was found to interact with several EGFR trafficking regulators in their Y2H screen, most notably FLOT1 and HTATIP2 (45). However, whether EMP3 does indeed affect EGFR activity by regulating receptor trafficking and whether such an effect is applicable to GBM cells remained to be clarified. In this study, I discovered a novel EMP3-dependent mechanism by which EGFR activity could be sustained in RTK II/CL-like IDH-wt GBM (Fig. 43). Specifically, I found out that EMP3 restricts EGFR trafficking into $RAB7^{+}$ late endosomes, and by doing so, it limits EGFR's eventual lysosomal degradation. Enhanced EGFR degradation secondary to EMP3 KO was rescued by overexpression of the novel EMP3 interactor TBC1D5, indicating that EMP3 and TBC1D5 may cooperate to exert this stabilizing effect on EGFR. Consequently, EMP3 sustains EGFR downstream signaling in RTK II/CL-like cells. This is supported by the phosphoproteomic data, which indicate inhibition of immediate, early effectors of EGFR (e.g., AKT1) as well as distal inhibition of EGFR targets

like CDK2. At the transcriptomic level, these signaling defects eventually lead to a reduction in the transcription of cell cycle-related and EGFR-responsive genes. Phenotypically, EMP3 depletion reduced proliferation rates, which is indirectly indicative of impaired cell cycle progression in RTK II/CL-like cells. Moreover, RTK II/CL-like cells depleted of EMP3 exhibited blunted mitogenic response to EGF and increased sensitivity to generalized and targeted kinase inhibition by staurosporine and osimertinib, respectively. Importantly, the findings correlate well with clinical data showing reduced total and phosphorylated EGFR levels in EMP3-low TCGA IDH-wt GBMs. Collectively, these results indicate that RTK II/CL-like cells may specifically rely on EMP3 to sustain EGFR-dependent oncogenic phenotypes in IDH-wt GBMs.

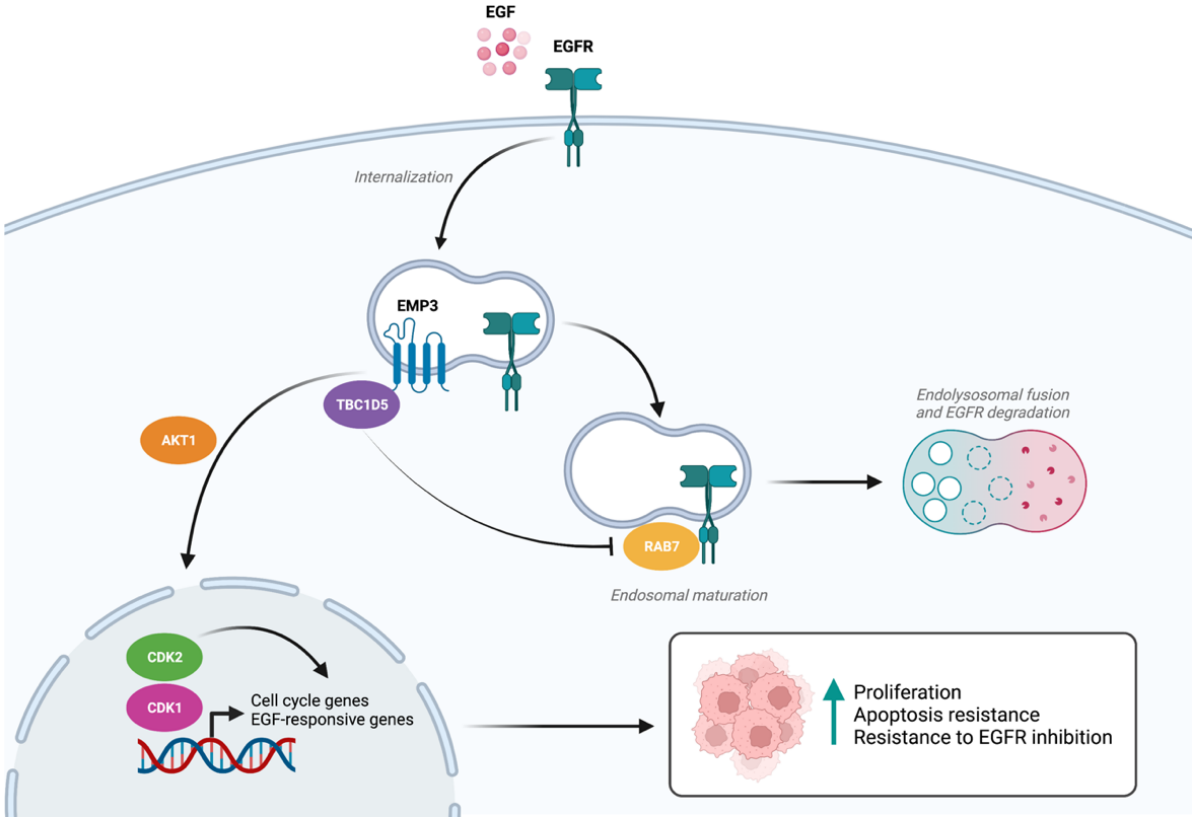

Figure 43. EMP3 restricts EGFR degradation and downstream signaling in RTK II/CL-like GBM cells. Upon binding to EGF, EGFR is internalized and trafficked towards endolysosomal degradation. Endosomal EMP3 and TBC1D5 may cooperate to restrict RAB7-dependent endosomal maturation and lysosomal fusion. This leads to the retention of EGFR, thus sustaining the downstream activity of AKT1 and the cyclin-dependent kinases CDK1 and CDK2. Consequently, there is increased transcription of genes involved in DNA replication, cell cycle, and EGFR tyrosine kinase inhibitor resistance. At the phenotypic level, this translates into increased cellular proliferation and mitogenic response to EGF, as well as reduced sensitivity to generalized and targeted EGFR inhibition. Figure was created using BioRender.com.

These findings also expand our knowledge of the retromer complex's involvement in EGFR trafficking. Several retromer components, most notably SNX1 and SNX2, have been previously linked to the regulation of EGFR degradation. For example, SNX1 overexpression

has been shown to reduce EGFR stability (106), while ablation of SNX2 localization in endosomes by mutation of its phox homology (PX) domain has been shown to inhibit ligand-induced degradation of EGFR (107). In this study, I have uncovered a novel role of another retromer component, TBC1D5, in this degradative process. TBC1D5 has long been known for its ability to inhibit RAB7 activity by facilitating its GTP hydrolysis (108–110). By inactivating RAB7, TBC1D5 can modulate a variety of RAB7-dependent processes, including RAB7 binding to the retromer complex (109), RAB7-mediated mitophagy (110), and RAB7 localization to late endosomal membranes (108,110,111). The latter is the most relevant to this study, as RAB7 late endosomal localization acts a key switch in EGFR degradation (85,112,113). As endosomes bearing internalized EGFR cargoes mature, they shed the early endosomal marker RAB5 and bind to activated GTP-bound RAB7 instead (112,113). Consequently, activated RAB7 directs the movement of late endosomes towards the lysosome-rich perinuclear area, where they eventually fuse with lysosomes to facilitate EGFR degradation (85). In this study, overexpression of TBC1D5 selectively reversed the effects of EMP3 KO on EGFR degradation in a manner that is dependent on its catalytic activity. This readout coincides well with the presumed inhibition of RAB7 activity by TBC1D5. Because EMP3 is validated to interact with TBC1D5, it is conceivable that the former could facilitate the latter's recruitment into maturing endosomes. By doing so, EMP3 could facilitate TBC1D5's restrictive effect on RAB7-dependent degradation of EGFR cargoes. This proposed model is not without precedence, as TBC1D5 is known to promote the recycling of ITGA5/ITGB1 and the retrieval of IGF2R from endosomes to the trans-Golgi network (114). Interestingly, these receptors were also identified in this study as EMP3 interactors, raising the question of whether EMP3 is also required for TBC1D5-dependent recycling of these non-EGFR receptors. To further validate the existing model, it will be necessary for future studies to examine how EMP3 modulates TBC1D5 recruitment in endosomes containing internalized EGFR. Moreover, to assess the broader impact of the proposed mechanism, systematic identification of other GBM receptors that rely on this EMP3/TBC1D5-dependent trafficking step will also be of interest.

Apart from uncovering this novel trafficking mechanism, I also mapped the downstream effects of EMP3 KO-induced reduction in EGFR stability. Specifically, the phosphoproteomic data indicate that EMP3 KO leads to the inhibition of immediate EGFR effectors (e.g. AKT1), which ultimately converges into the inhibition of cyclin-dependent kinases, most significantly CDK2. CDK2 has long been known to be a distal effector of EGFR. Knockdown of CDK2 can

reverse EGF-dependent oncogenic transformation (115), while EGFR activation by EGF has been shown to induce CDK2 activation (116). In GBM, inhibition of EGFR activity by the small molecule tyrosine kinase inhibitor AG1478 led to a reduction in CDK2 levels and G_1 arrest (117). Conversely, CDK2 activation has also been shown to promote *in vitro* proliferation, apoptosis resistance, and *in vivo* growth of GBM tumors (118). Consistent with this, CDK2 inhibition in RTK II/CL-like DK-MG and U-118 cells correlated well with the reduced transcription of genes involved in DNA replication and cell cycle progression. EMP3 KO-induced CDK2 inhibition also coincided with phenotypic defects that are indicative of impaired EGFR signaling. Thus, EMP3-dependent maintenance of EGFR stability sustains the EGFR/CDK2 signaling axis in RTK II/CL-like cells.

5.2.2 EMP3 – a putative organizer of CD44s and MET signaling complexes in MES-like cells

While this work was ongoing, an independent group working on the characterization of the *EMP3*-coded MAM blood antigen in erythroid cells also identified a direct and stable interaction between EMP3 and CD44 via co-immunoprecipitation (50). The authors further discovered that EMP3 may stabilize CD44 in mature erythrocytes and regulate CD44 distribution in dividing erythroid progenitors. However, the functional relevance of the EMP3-CD44 interaction remained unclear, especially in the context of CD44-high and EMP3-high MES-like GBMs. In this study, I independently discovered that EMP3 interacts with the standard isoform of CD44, CD44s, via multiple PPI experiments (i.e., BioID2, AP-MS, reciprocal FLAG pull-downs). The interaction requires full-length CD44s and can be situated within a broader interaction network as indicated by the BioID2 data. Specifically, in MES-like LN-18 cells, EMP3 and CD44 putatively interacts with mesenchymal RTKs (e.g., MET and PDGFRB) and various signaling effectors from the Rho GTPase family of proteins. Indeed, for the first time, I show that CD44s associates with MET in a manner that requires EMP3. Interestingly, loss of EMP3 concomitantly reduced the membrane presentation of MET but not of CD44, suggesting that reduced CD44s-MET complex formation may be a secondary effect of a MET-specific trafficking defect. Furthermore, loss of EMP3 abrogates HA-induced CD44 and HGF-induced MET mitogenic signaling and increases sensitivity to STS-induced apoptosis, indicating that EMP3's regulatory effect extends beyond mere structural organization of the CD44s-MET complex.

Future mechanistic studies will certainly be required to determine how EMP3 could support ligand-induced CD44 and MET signaling. In the case of CD44, it is plausible for EMP3 to 1)

act as a co-receptor via its extracellular domain (i.e., by regulating HA availability or binding) and/or 2) regulate the activity of CD44 downstream targets via its cytoplasmic-facing region (Fig. 44). A similar co-receptor function has already been demonstrated between EMP3 and TGFBR2 in CD44-high GBM cells (66), making the first scenario not unlikely. In this situation, it will also be of interest to understand how EMP3 glycosylation (or non-glycosylation, as it appears to be the case in LN-18 cells) could impact CD44's interaction with its ligand. Variable *N*-glycosylation of CD44 itself is known to either promote or inhibit HA binding; given that CD44 closely interacts with EMP3 in the membrane, it is possible that the presence (or absence) of glycans on EMP3 could modulate this process as well. While this study has shown that EMP3 interacts with CD44 in a glycosylation-independent manner, it has not ruled out a possible differential effect of EMP3 WT and N47A mutant proteins on HA binding or CD44s activity.

On the other hand, EMP3 may also facilitate the activation of Rho GTPase effectors identified in the LN-18 BioID2 screen. Several of these proteins are known to be downstream targets of CD44, and their activation by HA-bound CD44 induces a variety of oncogenic processes (119). EMP3's close interaction with these effectors suggests that it could facilitate the recruitment and eventual activation of these proteins on the cytoplasmic-facing side of CD44s-EMP3 complex (Fig. 44). Conversely, loss of EMP3 could attenuate this process. Consistent with this model, I have shown that EMP3 KO leads to the inhibition of CD44- and IQGAP1-dependent transcriptional programs in LN-18 EMP3 KO cells. IQGAP1 is a Rho GTPase effector that associates with CD44 upon HA induction (119,120). HA-bound CD44 activates IQGAP1, which subsequently induces ERK2 activation followed by ELK and estrogen receptor (ER)-α phosphorylation (119,120). This signaling cascade activates cyclin D1 and the transcription of ELK- and ER-responsive genes, culminating in increased tumor cell migration and proliferation (119,120). Consistent with this process, the microarray data also indicate slight reduction in the transcription of ERK- and ER-responsive genes upon EMP3 KO. While IQGAP1 was not identified as an EMP3 interactor in the BioID2 screen, it is known to interact with and activate the EMP3-interacting Rho GTPase PAK1 (121–123), indicating a plausible route by which EMP3 could ultimately influence IQGAP1 activity. Alternatively, EMP3-dependent activation of other Rho GTPases upon HA-CD44 binding may simply mimic the downstream transcriptional effects of IQGAP1 activation. While the mechanism remains unclear and the exact contribution of EMP3's extracellular and cytoplasmic domains to this

process needs further elucidation, it is certain that EMP3 is critical for CD44 activity, as EMP3 KO leads to inhibition of a CD44/IQGAP1 signaling and HA-induced proliferation.

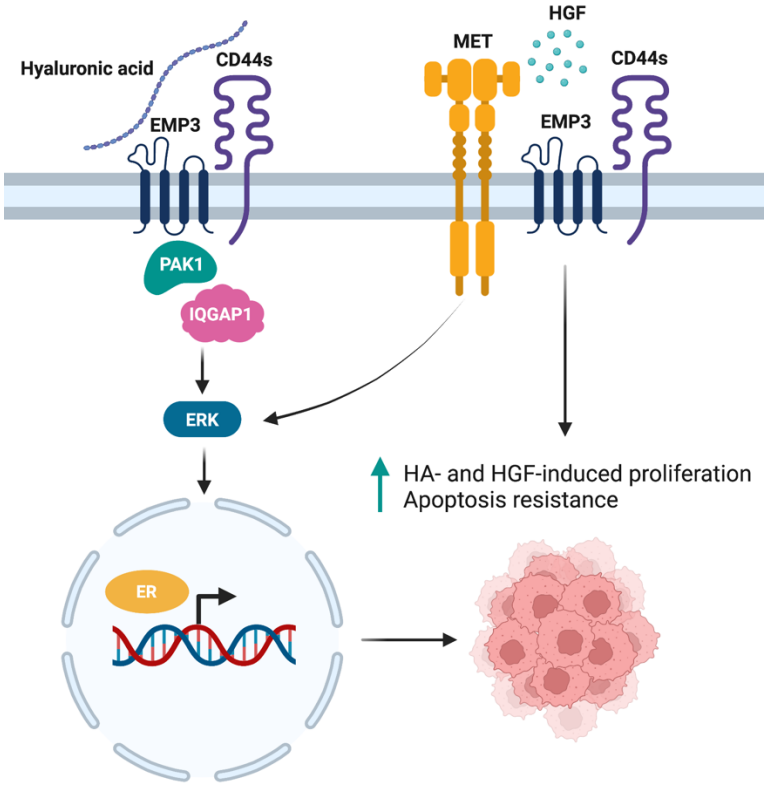

Figure 44. EMP3 putatively organizes the membrane interactions of CD44s and MET in MES-like cells. EMP3 may facilitate HA-CD44s signaling by acting as a co-receptor or by bridging CD44s to downstream Rho GTPase effectors (e.g. PAK1) identified in the LN-18 BioID2 screen. EMP3-dependent CD44 signaling may then activate the IQGAP1/ERK/ER signaling cascade, as supported by the transcriptomics data. Alternatively, EMP3 also promotes the formation of CD44s-MET complexes on the membrane. These complexes may then act to promote HGF/MET/ERK signaling and apoptosis resistance. Loss of EMP3 in MES-like cells abrogates HA- and HGF-induced cellular proliferation and sensitizes cells to STS-induced apoptosis. Figure was created using BioRender.com.

The findings in this study also show that EMP3 concomitantly supports MET signaling, as EMP3 KO attenuated the proliferative response of LN-18 cells to the MET ligand HGF and increased their sensitivity to apoptosis (Fig. 44). This may be a direct consequence of the abrogation of CD44s-MET complex formation, given that CD44 has been previously shown to be required for HGF-induced MET activation and contributory to MET-dependent apoptosis resistance (89,124,125). In primary keratinocytes and other cell lines, the CD44v6 splice isoform forms a complex with MET in an HGF-dependent manner (124). HGF-MET-CD44v6 complex formation then promotes MET autophosphorylation and internalization, as well as the activation of the pro-survival MET effectors MEK and ERK (124,126). Interestingly, ERK was also predicted to be slightly inhibited in LN-18 EMP3 KO cells. This is consistent with the idea

that EMP3 is required for CD44s-MET binding and downstream ERK activation. How EMP3 exactly facilitates CD44s-MET binding remains an open question. Like other tetraspanins, EMP3 may simply influence the lateral movement and clustering of these receptors (127,128). The cell surface proteome and immunostaining data, however, indicate that EMP3 may also be necessary to keep MET in the membrane. Therefore, EMP3 KO-induced abrogation of CD44s-MET binding may partially result from this initial membrane localization defect. In this regard, it will be interesting to dissect how EMP3 could regulate MET membrane presentation. It is worth noting that SNX2, a retromer component and an EMP3 interactor, has already been shown to promote the membrane localization of MET (129). Given this, future investigations may elucidate how EMP3 and SNX2 could synergistically act together to keep MET in the membrane and by doing so, enhance the probability of CD44s-MET complex formation.

5.3 EMP3 – potential implications and therapeutic potential in IDH-wt GBM

The findings reported in this study can have several implications in the context of IDH-wt GBM. First, EMP3's multifunctional nature indicates how it could also contribute to the underlying molecular heterogeneity of IDH-wt GBMs. As discussed earlier, IDH-wt GBMs are a molecularly diverse group of tumors, with each tumor harboring multiple cellular states and anatomic regions that are distinct at the genetic, epigenetic, transcriptomic, proteomic, and even metabolomic levels. EMP3-expressing GBM cells are mostly restricted to the subtypes that are driven by EGFR signaling (i.e., RTK II/CL/AC) or the tumor microenvironment (i.e., MES). As shown here, EMP3 interacts with distinct proteins and fulfills unique functions in cellular models that approximately recapitulate these two subtypes. These findings provide proof-of-concept for another level of heterogeneity that must be considered in IDH-wt GBM, namely the subcellular functional diversity that may emerge from protein moonlighting and cell type-specific PPI networks. The existence of moonlighting functions, coupled with reorganization of PPI networks, can confer cells with specialized functions; these, in turn, ultimately allow the appearance of cell type-specific phenotypes (96,105,130). This is perfectly demonstrated by EMP3, as it moonlights from being a trafficking protein and EGFR regulator in RTK II/CL-like cells (this study) to being a membrane organizer and ECM co-receptor in MES-like cells (this study), a TGFBR2 co-receptor in CD44-high GBMs (66), and a regulator of macrophage and T cell function in the GBM microenvironment (75). These distinct mechanisms, while compartmentalized in different cell types, may ultimately cooperate at the tissue level of organization to ensure sustained oncogenicity of the whole tumor.

Second, this study also shows how EMP3 can potentially contribute to the development of therapeutic resistance in IDH-wt GBMs. As proof-of-principle, I have demonstrated how EMP3 can attenuate the inhibitory effects of EGFR targeting in RTK II/CL-like GBM cells. This effect is most likely rooted in EMP3's ability to stabilize EGFR and sustain its downstream signaling. Tumor cells typically develop similar resistance mechanisms to ensure their constant survival. During the course of GBM development, EMP3 overexpression might have emerged as an added non-oncogene dependency to help EGFR-dependent RTK II/CL-like tumor cells sustain oncogenic RTK signaling. By overexpressing EMP3, tumor cells can bypass homeostatic mechanisms (e.g., endolysosomal degradation) that would have otherwise kept EGFR amplification or overactivation in check. Such a mechanism, in cooperation with other known compensatory processes (e.g., RTK switching, subclonal evolution, cell state plasticity), may partly explain why anti-EGFR monotherapies have been generally unsuccessful in the treatment of IDH-wt GBMs (131–133). Moving forward, similar EMP3-dependent drug resistance mechanisms in MES-like cells must also be identified and elucidated. Moreover, drug discovery efforts should consider targeting non-oncogene dependencies like EMP3 as part of combinatorial treatment regimens, as these targets may also play a crucial role in the emergence of therapeutic resistance.

5.4 Outlook

To better understand EMP3's function, several lines of investigation can be further pursued in future studies. First, systematic analysis of EMP3's involvement in various trafficking steps (e.g., clathrin-mediated endocytosis, endosome-to-Golgi retrograde transport, endocytic recycling) can be performed to determine EMP3's exact contribution to these processes. It will be critical to evaluate whether EMP3 is just a passive endosomal cargo, or whether it can also actively regulate these trafficking routes similar to how it restricts EGFR shuttling into late endosomes. This can be evaluated by testing the effect of EMP3 KO on the trafficking of established CCV-, retromer-, or EARP-associated cargoes. With this, it can be clarified why EMP3 needs to cycle back and forth from the plasma membrane and into these intracellular compartments.

Likewise, EMP3's impact on receptor function at the level of the plasma membrane can be further elucidated. In this regard, it will be of interest to test EMP3's broader role in the lateral organization or ligand-induced clustering of EMP3-associated RTKs and ECM receptors. Furthermore, the potential relevance of EMP3 in intercellular communication can also be

assessed by using co-culture systems that mimic putative EMP3-dependent cell-to-cell interactions in IDH-wt GBMs. Given EMP3's expression in macrophages and T cells, it will be of particular interest to obtain insights on how EMP3 could also influence immune surveillance by these cell types. Moreover, considering the possible modulatory effect of EMP3-attached glycans on intra- and inter-cellular interactors and the glycosylation-dependent PPI networks described in this study, further characterization of the functional consequences of EMP3 *N*-glycosylation will be necessary.

To further elucidate EMP3's cell type-specific functions and to better assess its therapeutic potential, it will also be necessary to use model systems that better recapitulate subtype-specific tumor biology. These may include molecularly classified patient-derived spheroid cultures, glioblastoma brain organoids, and/or PDX models. *In vitro* models can be further subjected to high-throughput drug screens to identify possible treatments that could synergize with EMP3 inhibition. Subsequently, top hits can be further validated with animal models. With respect to EMP3 targeting, it may also be promising to initiate the preclinical development of an EMP3 inhibitor that could be tested on the relevant model systems. An antibody-based modality (e.g., neutralizing antibodies, antibody-based degraders, or chimeric antigen receptor T cells) may provide a reasonable starting point, given that EMP3 is mostly cell surface-exposed. However, drug design must be balanced carefully with other anticipated issues like BBB permeability as well as potential off-target effects on non-malignant cells that also express EMP3. While there is still a long way to go before an EMP3 inhibitor can be developed and put to clinical use, this study provides a compelling rationale to continue investigating EMP3's function and its potential therapeutic relevance in IDH-wt GBM.

6 Attributions

EMP3 KO cells were provided by Dr. Arne Christians. EMP3 WT/N47A and TagRFP coding sequences in pDONR221 and the pMXs-GW-IRES-BsdR plasmid were provided by Dr. Stefan Pusch. The DKFZ Clone Repository provided the following plasmids: pMXs-GW-IRES-PuroR, TBC1D5 -STOP in pDONR223. The template for cloning the BioID2 tag was provided by Dr. David Reuß. Caspase-Glo® 3/7 assays performed on STS-treated GBM cells were performed under my supervision by Natalie Bächle as part of her Bachelor's thesis. Osimertinib treatments were performed together with Alexandra Krauß. Susanne Gärtner provided valuable technical support in TA cloning and BioID2 experiments. Johanna Knieper provided technical support for FLAG pull-down of CD44 truncation mutants. The DKFZ Antibody Core Facility provided the EMP3 antibody used in this study. Dr. Damir Krunic from the DKFZ Light Microscopy Facility provided the ImageJ script for quantifying PLA signals. Gene expression profiling was performed by the Microarray Unit of the DKFZ GPCF. The MS-based Protein Analysis Unit performed MS analysis and provided valuable support in the downstream analysis of MS data.

7 Acknowledgements

My deepest gratitude goes to the Helmholtz International Graduate School for Cancer Research and the SFB 1389 UNITE Glioblastoma Consortium for collectively funding my doctoral studies over the course of four years. My PhD would not have been possible without your financial support.

Thank you also to Dr. Stefan Pusch, for giving me the chance to be part of the CCU Neuropathology and work on the EMP3 project. Thank you so much for being a supportive and kind mentor throughout the years and for giving me the scientific freedom to pursue questions that interest me. For the trust, guidance, encouragement, opportunities, and all the little tips, be it about PPI experiments or life in academia, thank you.

Thank you also to Prof. Dr. med. Andreas von Deimling, for pushing me to always think about the significance of my work and what it will mean for patients suffering from a monstrous disease like GBM. Thank you for all the advice and encouragement and for always helping me ground my work.

To my TAC and thesis defense examiners, Prof. Dr. Peter Angel and Dr. Francesca Ciccolini, thank you for constantly providing constructive feedback and posing challenging but necessary questions. Your valuable input helped me bring the project into its final form.

To Dr. Dominic Helm, Martin Schneider, and the rest of DKFZ MS Core Facility, thank you for always being so accommodating, helpful, and supportive with the MS experiments. A lot of my data would not have been generated without your technical expertise.

To Dr. Damir Krunic, for guiding me through microscopy experiments and for providing the scripts that helped me analyze my images. Thank you also for all the funny jokes during training sessions.

To Dr. Julia Zaman, for being a constant presence over the past four years. Thank you for the support and for always trying to understand my project and provide feedback. Thank you also for sharing your time and knowledge whenever I need help or have stupid questions, and for giving me the right amount of pressure to finish this thesis.

To the trio of students that allowed me to experience the joy of mentoring: Ivana Karabogdan, Alexandra Krauß, Natalie Bächle. Thank you for being very excellent students and for helping

me push the EMP3 project forward. Special thanks to Ivana for proofreading my thesis and for giving the CD44 and TurboID subprojects a chance, to Alex for the amazing hands which proved to be critical for the osimertinib experiments, and to Natalie for being so diligent with all the apoptosis experiments. Thank you for all the stimulating scientific discussions and for all your curious questions. Thank you also for the friendship, the laughter, and all the deep and shallow conversations over lunch or waiting times.

To the rest of the B300 crew, past and present: Jessica Eisel, Flávio De Campos Mello Monteiro, Antonia Tietzel, David Vonhören, Philipp Sievers, Jana Quadrizius, Lars Noller, Susanne Gärtner, Johanna Knieper, Eric Poisel, Maria Hörner, Austin Millwood, thank you for the company and for helping cultivate a nice lab environment.

To my German language teacher, Marion Erb, for being so patient and resolute at teaching me Deutsch. Thank you for being so welcoming and friendly as it really helped me overcome being intimidated at learning the language.

To my Heidelberg/Mannheim HighDef Pinoy family—Josh, Fidel, Paulo, Arlou, Angel, and Aileen—thank you for all the adobo we've shared, the board game and movie nights, Yangda runs, and picnics by the Neckar. Thank you for simply being my home away from home.

To Iván, thank you for the deep friendship starting from the DKFZ selection round. You have been a real brother since Day 1.

To the GradMAP core team—Carlo, Weaverly, Louise, Paul—thank you for all your crazy ideas and inviting me to be part of this wonderful endeavor. It was a honor to help bring GradMAP into existence with all of you.

To Charles, Jana, and the rest of the SPiNE crew, for all the stimulating online meetings about neuroscience. Special thanks to Charles for being a confidant and a mentor, and to Jana for always spending the time to catch up with me.

To Prof. Dr. Reynaldo Garcia for helping me jumpstart my scientific career, my deepest thanks.

To Pat, for showing me the way. Thank you.

To Bea, my dad and mom, and my brothers, for believing in me and for always being there during good times and bad. Thank you for being my source of strength throughout this journey.

8 References

1. Weller, M. *et al.* Michael Weller , Wolfgang Wick , Ken Aldape , Michael Brada , Mitchell Berger , Stefan M. Pfister , Ryo Nishikawa , Mark Rosenthal , Patrick Y. Wen , Roger Stupp and Guido Reifenberger. *Nat Rev Dis Primers* 1, 15017 (2015).

2. McLendon, R. *et al.* Comprehensive genomic characterization defines human glioblastoma genes and core pathways. *Nature* 455, 1061–8 (2008).

3. Wen, P. Y. *et al.* Glioblastoma in adults: a Society for Neuro-Oncology (SNO) and European Society of Neuro-Oncology (EANO) consensus review on current management and future directions. *Neuro-oncology* 22, 1073–1113 (2020).

4. Ostrom, Q. T., Cioffi, G., Waite, K., Kruchko, C. & Barnholtz-Sloan, J. S. CBTRUS Statistical Report: Primary Brain and Other Central Nervous System Tumors Diagnosed in the United States in 2014–2018. *Neuro-oncology* 23, iii1–iii105 (2021).

5. Louis, D. N. *et al.* The 2021 WHO Classification of Tumors of the Central Nervous System: a summary. *Neuro-oncology* 23, 1231–1251 (2021).

6. Yabo, Y. A., Niclou, S. P. & Golebiewska, A. Cancer cell heterogeneity and plasticity: A paradigm shift in glioblastoma. *Neuro-oncology* noab269- (2021). doi:10.1093/neuonc/noab269

7. White, K. *et al.* New hints towards a precision medicine strategy for IDH wild-type Glioblastoma. *Ann Oncol* 31, 1679–1692 (2020).

8. Solinge, T. S. van, Nieland, L., Chiocca, E. A. & Broekman, M. L. D. Advances in local therapy for glioblastoma — taking the fight to the tumour. *Nat Rev Neurol* 1–16 (2022). doi:10.1038/s41582-022-00621-0

9. Patel, A. P. *et al.* Single-cell RNA-seq highlights intratumoral heterogeneity in primary glioblastoma. *Sci New York N Y* 344, 1396–401 (2014).

10. Neftel, C. *et al.* An Integrative Model of Cellular States, Plasticity, and Genetics for Glioblastoma. *Cell* 178, 835-849.e21 (2019).

11. Stupp, R. *et al.* Effects of radiotherapy with concomitant and adjuvant temozolomide versus radiotherapy alone on survival in glioblastoma in a randomised phase III study: 5-year analysis of the EORTC-NCIC trial. *Lancet Oncol* 10, 459–466 (2009).

12. Zhu, P., Du, X. L., Lu, G. & Zhu, J.-J. Survival benefit of glioblastoma patients after FDA approval of temozolomide concomitant with radiation and bevacizumab: A population-based study. *Oncotarget* 8, 44015–44031 (2017).

13. Llaguno, S. R. A. & Parada, L. F. Cell of origin of glioma: biological and clinical implications. *Brit J Cancer* 115, 1445–1450 (2016).

14. Lee, J. H. *et al.* Human glioblastoma arises from subventricular zone cells with low-level driver mutations. *Nature* 560, 243–247 (2018).

15. Alcantara Llaguno, S. R. *et al.* Adult Lineage-Restricted CNS Progenitors Specify Distinct Glioblastoma Subtypes. *Cancer Cell* 28, 429–440 (2015).

16. Llaguno, S. A. *et al.* Cell-of-origin susceptibility to glioblastoma formation declines with neural lineage restriction. *Nat Neurosci* 22, 545–555 (2019).

17. Llaguno, S. A. *et al.* Malignant Astrocytomas Originate from Neural Stem/Progenitor Cells in a Somatic Tumor Suppressor Mouse Model. *Cancer Cell* 15, 45–56 (2009).

18. Couturier, C. P. *et al.* Single-cell RNA-seq reveals that glioblastoma recapitulates a normal neurodevelopmental hierarchy. *Nat Commun* 11, 3406 (2020).

19. Chen, R. *et al.* A Hierarchy of Self-Renewing Tumor-Initiating Cell Types in Glioblastoma. *Cancer Cell* 17, 362–375 (2010).

20. Wang, J. *et al.* CD133 negative glioma cells form tumors in nude rats and give rise to CD133 positive cells. *Int J Cancer* 122, 761–768 (2008).

21. Ogden, A. T. *et al.* Identification of A2B5+CD133− Tumor-Initiating Cells in Adult Human Gliomas. *Neurosurgery* 62, 505–515 (2008).

22. Al-Mayhani, T. F. *et al.* A non-hierarchical organization of tumorigenic NG2 cells in glioblastoma promoted by EGFR. *Neuro-oncology* 21, 719–729 (2019).

23. Körber, V. *et al.* Evolutionary Trajectories of IDHWT Glioblastomas Reveal a Common Path of Early Tumorigenesis Instigated Years ahead of Initial Diagnosis. *Cancer Cell* 35, 692-704.e12 (2019).

24. Phillips, H. S. *et al.* Molecular subclasses of high-grade glioma predict prognosis, delineate a pattern of disease progression, and resemble stages in neurogenesis. *Cancer Cell* 9, 157–173 (2006).

25. Verhaak, R. G. W. *et al.* Integrated Genomic Analysis Identifies Clinically Relevant Subtypes of Glioblastoma Characterized by Abnormalities in PDGFRA, IDH1, EGFR, and NF1. *Cancer Cell* 17, 98–110 (2010).

26. Wang, Q. *et al.* Tumor Evolution of Glioma-Intrinsic Gene Expression Subtypes Associates with Immunological Changes in the Microenvironment. *Cancer Cell* 32, 42-56.e6 (2017).

27. Brennan, C. *et al.* Glioblastoma Subclasses Can Be Defined by Activity among Signal Transduction Pathways and Associated Genomic Alterations. *Plos One* 4, e7752 (2009).

28. Wang, L.-B. *et al.* Proteogenomic and metabolomic characterization of human glioblastoma. *Cancer Cell* 39, 509-528.e20 (2021).

29. Sturm, D. *et al.* Hotspot Mutations in H3F3A and IDH1 Define Distinct Epigenetic and Biological Subgroups of Glioblastoma. *Cancer Cell* 22, 425–437 (2012).

30. Capper, D. *et al.* DNA methylation-based classification of central nervous system tumours. *Nature* 555, 469–474 (2018).

31. Horbinski, C., Berger, T., Packer, R. J. & Wen, P. Y. Clinical implications of the 2021 edition of the WHO classification of central nervous system tumours. *Nat Rev Neurol* 1–15 (2022). doi:10.1038/s41582-022-00679-w

32. Wu, Y. *et al.* Glioblastoma epigenome profiling identifies SOX10 as a master regulator of molecular tumour subtype. *Nat Commun* 11, 6434 (2020).

33. Ceccarelli, M. *et al.* Molecular Profiling Reveals Biologically Discrete Subsets and Pathways of Progression in Diffuse Glioma. *Cell* 164, 550–563 (2016).

34. Chaligne, R. *et al.* Epigenetic encoding, heritability and plasticity of glioma transcriptional cell states. *Nat Genet* 1–11 (2021). doi:10.1038/s41588-021-00927-7

35. Garofano, L. *et al.* Pathway-based classification of glioblastoma uncovers a mitochondrial subtype with therapeutic vulnerabilities. *Nat Cancer* 2, 141–156 (2021).

36. Sottoriva, A. *et al.* Intratumor heterogeneity in human glioblastoma reflects cancer evolutionary dynamics. *Proc National Acad Sci* 110, 4009–4014 (2013).

37. Johnson, K. C. *et al.* Single-cell multimodal glioma analyses identify epigenetic regulators of cellular plasticity and environmental stress response. *Nat Genet* 1–13 (2021). doi:10.1038/s41588-021-00926-8

38. Puchalski, R. B. *et al.* An anatomic transcriptional atlas of human glioblastoma. *Science* 360, 660–663 (2018).

39. Lam, K. H. B. *et al.* Topographic mapping of the glioblastoma proteome reveals a triple-axis model of intra-tumoral heterogeneity. *Nat Commun* 13, 116 (2022).

40. Hahn, W. C. *et al.* An expanded universe of cancer targets. *Cell* 184, 1142–1155 (2021).

41. Ben-Porath, I., Kozak, C. A. & Benvenisty, N. Chromosomal Mapping ofTmp(Emp1),Xmp(Emp2), andYmp(Emp3), Genes Encoding Membrane Proteins Related toPmp22. *Genomics* 49, 443–447 (1998).

42. Martija, A. A. & Pusch, S. The Multifunctional Role of EMP3 in the Regulation of Membrane Receptors Associated with IDH-Wild-Type Glioblastoma. *Int J Mol Sci* 22, 5261 (2021).

43. Taylor, V. & Suter, U. Epithelial membrane protein-2 and epithelial membrane protein-3: two novel members of the peripheral myelin protein 22 gene family. *Gene* 175, 115–120 (1996).

44. Wang, Y.-W., Cheng, H.-L., Ding, Y.-R., Chou, L.-H. & Chow, N.-H. EMP1, EMP 2, and EMP3 as novel therapeutic targets in human cancer. *Biochimica Et Biophysica Acta Bba - Rev Cancer* 1868, 199–211 (2017).

45. Christians, A., Poisel, E., Hartmann, C., Deimling, A. & Pusch, S. Characterization of the epithelial membrane protein 3 interaction network reveals a potential functional link to mitogenic signal transduction regulation. *Int J Cancer* 145, 461–473 (2019).

46. Thul, P. J. *et al.* A subcellular map of the human proteome. *Science* 356, eaal3321 (2017).

47. Uhlén, M. *et al.* Tissue-based map of the human proteome. *Science* 347, 1260419 (2015).

48. Alam, O. A single-cell-type transcriptomics map of human tissues. *Nat Genet* 53, 1275–1275 (2021).

49. Kusumoto, Y. *et al.* Epithelial membrane protein 3 (Emp3) downregulates induction and function of cytotoxic T lymphocytes by macrophages via TNF-α production. *Cell Immunol* 324, 33–41 (2018).

50. Thornton, N. *et al.* Disruption of the tumour-associated EMP3 enhances erythroid proliferation and causes the MAM-negative phenotype. *Nat Commun* 11, 3569 (2020).

51. Kanton, S. *et al.* Organoid single-cell genomic atlas uncovers human-specific features of brain development. *Nature* 574, 418–422 (2019).

52. Uzquiano, A. *et al.* Single-cell multiomics atlas of organoid development uncovers longitudinal molecular programs of cellular diversification of the human cerebral cortex. *Biorxiv* 2022.03.17.484798 (2022). doi:10.1101/2022.03.17.484798

53. Bolin, L. M. *et al.* HNMP-1: A Novel Hematopoietic and Neural Membrane Protein Differentially Regulated in Neural Development and Injury. *J Neurosci* 17, 5493–5502 (1997).

54. Bolin, L. M. *et al.* HNMP-1: A Novel Hematopoietic and Neural Membrane Protein Differentially Regulated in Neural Development and Injury. *J Neurosci* 17, 5493–5502 (1997).

55. Alaminos, M. *et al.* EMP3, a Myelin-Related Gene Located in the Critical 19q13.3 Region, Is Epigenetically Silenced and Exhibits Features of a Candidate Tumor Suppressor in Glioma and Neuroblastoma. *Cancer Res* 65, 2565–2571 (2005).

56. Xue, Q. *et al.* Epithelial membrane protein 3 is frequently shown as promoter methylation and functions as a tumor suppressor gene in non-small cell lung cancer. *Exp Mol Pathol* 95, 313–318 (2013).

57. Fumoto, S. *et al.* EMP3 as a tumor suppressor gene for esophageal squamous cell carcinoma. *Cancer Lett* 274, 25–32 (2009).

58. Ma, Q. *et al.* EMP3, which is regulated by miR-663a, suppresses gallbladder cancer progression via interference with the MAPK/ERK pathway. *Cancer Lett* 430, 97–108 (2018).

59. Zhou, W. *et al.* EMP3 Overexpression in Primary Breast Carcinomas is not Associated with Epigenetic Aberrations. *J Korean Med Sci* 24, 97–103 (2009).

60. Zhou, K., Sun, Y., Dong, D., Zhao, C. & Wang, W. EMP3 negatively modulates breast cancer cell DNA replication, DNA damage repair, and stem-like properties. *Cell Death Dis* 12, 844 (2021).

61. Hsieh, Y.-H. *et al.* Targeting EMP3 suppresses proliferation and invasion of hepatocellular carcinoma cells through inactivation of PI3K/Akt pathway. *Oncotarget* 6, 34859–34874 (2015).

62. Wang, Y.-W. *et al.* Potential Significance of EMP3 in Patients with Upper Urinary Tract Urothelial Carcinoma: Crosstalk with ErbB2-PI3K-Akt Pathway. *J Urology* 192, 242–251 (2014).

63. Amaddii, M. *et al.* Flotillin-1/Reggie-2 Protein Plays Dual Role in Activation of Receptor-tyrosine Kinase/Mitogen-activated Protein Kinase Signaling*. *J Biol Chem* 287, 7265–7278 (2012).

64. Zhang, C., Li, A., Zhang, X. & Xiao, H. A Novel TIP30 Protein Complex Regulates EGF Receptor Signaling and Endocytic Degradation*. *J Biol Chem* 286, 9373–9381 (2011).

65. Yue, H., Xu, Q. & Xie, S. High EMP3 expression might independently predict poor overall survival in glioblastoma and its expression is related to DNA methylation. *Medicine* 97, e9538 (2018).

66. Jun, F. *et al.* Epithelial membrane protein 3 regulates TGF-β signaling activation in CD44-high glioblastoma. *Oncotarget* 8, (2016).

67. Bowman, R. L., Wang, Q., Carro, A., Verhaak, R. G. W. & Squatrito, M. GlioVis data portal for visualization and analysis of brain tumor expression datasets. *Neuro-oncology* 19, 139–141 (2016).

68. Hara, T. *et al.* Interactions between cancer cells and immune cells drive transitions to mesenchymal-like states in glioblastoma. *Cancer Cell* (2021). doi:10.1016/j.ccell.2021.05.002

69. Bhaduri, A. *et al.* Outer Radial Glia-like Cancer Stem Cells Contribute to Heterogeneity of Glioblastoma. *Cell Stem Cell* 26, 48-63.e6 (2020).

70. Guo, X., Su, J. & He, X. A 4-gene panel predicting the survival of patients with glioblastoma. *J Cell Biochem* 120, 16037–16043 (2019).

71. Gao, Y.-F. *et al.* PPIC, EMP3 and CHI3L1 Are Novel Prognostic Markers for High Grade Glioma. *Int J Mol Sci* 17, 1808 (2016).

72. Gerber, N. K. *et al.* Transcriptional diversity of long-term glioblastoma survivors. *Neuro-oncology* 16, 1186–1195 (2014).

73. Colman, H. *et al.* A multigene predictor of outcome in glioblastoma. *Neuro-oncology* 12, 49–57 (2009).

74. Kahm, Y.-J., Kim, R.-K., Jung, U. & Kim, I.-G. Epithelial membrane protein 3 regulates lung cancer stem cells via the TGF-β signaling pathway. *Int J Oncol* 59, 80 (2021).

75. Chen, Q. *et al.* EMP3 mediates glioblastoma-associated macrophage infiltration to drive T cell exclusion. *J Exp Clin Canc Res* 40, 160 (2021).

76. Mootha, V. K. *et al.* PGC-1α-responsive genes involved in oxidative phosphorylation are coordinately downregulated in human diabetes. *Nat Genet* 34, 267–273 (2003).

77. Subramanian, A. *et al.* Gene set enrichment analysis: A knowledge-based approach for interpreting genome-wide expression profiles. *Proc National Acad Sci* 102, 15545–15550 (2005).

78. Krämer, A., Green, J., Pollard, J. & Tugendreich, S. Causal analysis approaches in Ingenuity Pathway Analysis. *Bioinformatics* 30, 523–530 (2014).

79. Kuleshov, M. V. *et al.* KEA3: improved kinase enrichment analysis via data integration. *Nucleic Acids Res* 49, W304–W316 (2021).

80. Tyanova, S. *et al.* The Perseus computational platform for comprehensive analysis of (prote)omics data. *Nat Methods* 13, 731–740 (2016).

81. Knight, J. D. R. *et al.* ProHits-viz: a suite of web tools for visualizing interaction proteomics data. *Nat Methods* 14, 645–646 (2017).

82. Yılmaz, S. *et al.* Robust inference of kinase activity using functional networks. *Nat Commun* 12, 1177 (2021).

83. Kim, D. I. *et al.* An improved smaller biotin ligase for BioID proximity labeling. *Mol Biol Cell* 27, 1188–1196 (2016).

84. Francavilla, C. *et al.* Multilayered proteomics reveals molecular switches dictating ligand-dependent EGFR trafficking. *Nat Struct Mol Biol* 23, 608–618 (2016).

85. Bakker, J., Spits, M., Neefjes, J. & Berlin, I. The EGFR odyssey – from activation to destruction in space and time. *J Cell Sci* 130, 4087–4096 (2017).

86. Kobayashi, S. *et al.* Transcriptional Profiling Identifies Cyclin D1 as a Critical Downstream Effector of Mutant Epidermal Growth Factor Receptor Signaling. *Cancer Res* 66, 11389–11398 (2006).

87. Akbani, R. *et al.* Realizing the Promise of Reverse Phase Protein Arrays for Clinical, Translational, and Basic Research: A Workshop Report The RPPA (Reverse Phase Protein Array) Society. *Mol Cell Proteomics* 13, 1625–1643 (2014).

88. Ponta, H., Sherman, L. & Herrlich, P. A. CD44: From adhesion molecules to signalling regulators. *Nat Rev Mol Cell Bio* 4, 33–45 (2003).

89. Zöller, M. CD44: can a cancer-initiating cell profit from an abundantly expressed molecule? *Nat Rev Cancer* 11, 254–267 (2011).

90. Varnaitė, R. & MacNeill, S. A. Meet the neighbors: Mapping local protein interactomes by proximity-dependent labeling with BioID. *Proteomics* 16, 2503–2518 (2016).

91. Simons, K. & Toomre, D. Lipid rafts and signal transduction. *Nat Rev Mol Cell Bio* 1, 31–39 (2000).

92. Casaletto, J. B. & McClatchey, A. I. Spatial regulation of receptor tyrosine kinases in development and cancer. *Nat Rev Cancer* 12, 387–400 (2012).

93. Lee, J.-L., Wang, M.-J., Sudhir, P.-R. & Chen, J.-Y. CD44 Engagement Promotes Matrix-Derived Survival through the CD44-SRC-Integrin Axis in Lipid Rafts. *Mol Cell Biol* 28, 5710–5723 (2008).

94. Ono, Y. J. *et al.* Met Signaling Cascade Is Amplified by the Recruitment of Phosphorylated Met to Lipid Rafts via CD24 and Leads to Drug Resistance in Endometrial Cancer Cell Lines. *Mol Cancer Ther* 14, 2353–2363 (2015).

95. Luck, K. *et al.* A reference map of the human binary protein interactome. *Nature* 580, 402–408 (2020).

96. Huttlin, E. L. *et al.* Dual proteome-scale networks reveal cell-specific remodeling of the human interactome. *Cell* 184, 3022-3040.e28 (2021).

97. Pinho, S. S. & Reis, C. A. Glycosylation in cancer: mechanisms and clinical implications. *Nat Rev Cancer* 15, 540–555 (2015).

98. Cecchi, F. *et al.* Targeted Disruption of Heparan Sulfate Interaction with Hepatocyte and Vascular Endothelial Growth Factors Blocks Normal and Oncogenic Signaling. *Cancer Cell* 22, 250–262 (2012).

99. Paszek, M. J. *et al.* The cancer glycocalyx mechanically primes integrin-mediated growth and survival. *Nature* 511, 319–325 (2014).

100. Hebert, D. N., Lamriben, L., Powers, E. T. & Kelly, J. W. The intrinsic and extrinsic effects of N-linked glycans on glycoproteostasis. *Nat Chem Biol* 10, 902–910 (2014).

101. Shrimal, S., Cherepanova, N. A. & Gilmore, R. Cotranslational and posttranslocational N-glycosylation of proteins in the endoplasmic reticulum. *Semin Cell Dev Biol* 41, 71–78 (2015).

102. Xu, C. & Ng, D. T. W. Glycosylation-directed quality control of protein folding. *Nat Rev Mol Cell Bio* 16, 742–752 (2015).

103. Kung, L. A. *et al.* Global analysis of the glycoproteome in Saccharomyces cerevisiae reveals new roles for protein glycosylation in eukaryotes. *Mol Syst Biol* 5, 308–308 (2009).

104. Schmidt, C. *et al.* Amyloid precursor protein and amyloid beta-peptide bind to ATP synthase and regulate its activity at the surface of neural cells. *Mol Psychiatr* 13, 953–69 (2007).

105. Singh, N. & Bhalla, N. Moonlighting Proteins. *Annu Rev Genet* 54, 1–21 (2020).

106. Kurten, R. C., Cadena, D. L. & Gill, G. N. Enhanced Degradation of EGF Receptors by a Sorting Nexin, SNX1. *Science* 272, 1008–1010 (1996).

107. Gullapalli, A. *et al.* A Role for Sorting Nexin 2 in Epidermal Growth Factor Receptor Down-regulation: Evidence for Distinct Functions of Sorting Nexin 1 and 2 in Protein Trafficking. *Mol Biol Cell* 15, 2143–2155 (2004).

108. Seaman, M. N. J., Harbour, M. E., Tattersall, D., Read, E. & Bright, N. Membrane recruitment of the cargo-selective retromer subcomplex is catalysed by the small GTPase Rab7 and inhibited by the Rab-GAP TBC1D5. *J Cell Sci* 122, 2371–2382 (2009).

109. Seaman, M. N. J., Mukadam, A. S. & Breusegem, S. Y. Inhibition of TBC1D5 activates Rab7a and can enhance the function of the retromer cargo-selective complex. *J Cell Sci* 131, jcs.217398 (2018).

110. Jimenez-Orgaz, A. *et al.* Control of RAB7 activity and localization through the retromer-TBC1D5 complex enables RAB7-dependent mitophagy. *Embo J* 37, 235–254 (2018).

111. Kvainickas, A. *et al.* Retromer and TBC1D5 maintain late endosomal RAB7 domains to enable amino acid–induced mTORC1 signalingRetromer maintains amino acid signaling. *J Cell Biology* 218, 3019–3038 (2019).

112. Huotari, J. & Helenius, A. Endosome maturation. *Embo J* 30, 3481–3500 (2011).

113. Borchers, A.-C., Langemeyer, L. & Ungermann, C. Who's in control? Principles of Rab GTPase activation in endolysosomal membrane trafficking and beyond. *J Cell Biol* 220, e202105120 (2021).

114. Jia, D. *et al.* Structural and mechanistic insights into regulation of the retromer coat by TBC1d5. *Nat Commun* 7, 13305 (2016).

115. Peng, C. *et al.* Cyclin-dependent kinase 2 (CDK2) is a key mediator for EGF-induced cell transformation mediated through the ELK4/c-Fos signaling pathway. *Oncogene* 35, 1170–1179 (2016).

116. Bill, H. M. *et al.* Epidermal Growth Factor Receptor-Dependent Regulation of Integrin-Mediated Signaling and Cell Cycle Entry in Epithelial Cells. *Mol Cell Biol* 24, 8586–8599 (2004).

117. Carrasco-García, E. *et al.* Small tyrosine kinase inhibitors interrupt EGFR signaling by interacting with erbB3 and erbB4 in glioblastoma cell lines. *Exp Cell Res* 317, 1476–1489 (2011).

118. Wang, J. *et al.* Cyclin-Dependent Kinase 2 Promotes Tumor Proliferation and Induces Radio Resistance in Glioblastoma. *Transl Oncol* 9, 548–556 (2016).

119. Bourguignon, L. Y. W. Hyaluronan-mediated CD44 activation of RhoGTPase signaling and cytoskeleton function promotes tumor progression. *Semin Cancer Biol* 18, 251–259 (2008).

120. Bourguignon, L. Y. W., Gilad, E., Rothman, K. & Peyrollier, K. Hyaluronan-CD44 Interaction with IQGAP1 Promotes Cdc42 and ERK Signaling, Leading to Actin Binding, Elk-1/Estrogen Receptor Transcriptional Activation, and Ovarian Cancer Progression. *J Biol Chem* 280, 11961–11972 (2005).

121. Li, R. *et al.* Localization of the PAK1-, WASP-, and IQGAP1-specifying Regions of Cdc42*. *J Biol Chem* 274, 29648–29654 (1999).

122. Awasthi, A. *et al.* Rap1b facilitates NK cell functions via IQGAP1-mediated signalosomes. *J Exp Medicine* 207, 1923–1938 (2010).

123. Abel, A. M. *et al.* IQGAP1: Insights into the function of a molecular puppeteer. *Mol Immunol* 65, 336–349 (2015).

124. Orian-Rousseau, V., Chen, L., Sleeman, J. P., Herrlich, P. & Ponta, H. CD44 is required for two consecutive steps in HGF/c-Met signaling. *Gene Dev* 16, 3074–3086 (2002).

125. Orian-Rousseau, V. & Sleeman, J. CD44 is a Multidomain Signaling Platform that Integrates Extracellular Matrix Cues with Growth Factor and Cytokine Signals. *Adv Cancer Res* 123, 231–254 (2014).

126. Hasenauer, S. *et al.* Internalization of Met Requires the Co-Receptor CD44v6 and Its Link to ERM Proteins. *Plos One* 8, e62357 (2013).

127. Berditchevski, F. & Odintsova, E. Tetraspanins as Regulators of Protein Trafficking. *Traffic* 8, 89–96 (2007).

128. Yáñez-Mó, M., Barreiro, O., Gordon-Alonso, M., Sala-Valdés, M. & Sánchez-Madrid, F. Tetraspanin-enriched microdomains: a functional unit in cell plasma membranes. *Trends Cell Biol* 19, 434–446 (2009).

129. Ogi, S. *et al.* Sorting nexin 2-mediated membrane trafficking of c-Met contributes to sensitivity of molecular-targeted drugs. *Cancer Sci* 104, 573–583 (2013).

130. Bludau, I. & Aebersold, R. Proteomic and interactomic insights into the molecular basis of cell functional diversity. *Nat Rev Mol Cell Bio* 1–14 (2020). doi:10.1038/s41580-020-0231-2

131. Pearson, J. R. D. & Regad, T. Targeting cellular pathways in glioblastoma multiforme. *Signal Transduct Target Ther* 2, 17040 (2017).

132. Silva, E. C. D., Mercier, M.-C., Etienne-Selloum, N., Dontenwill, M. & Choulier, L. A Systematic Review of Glioblastoma-Targeted Therapies in Phases II, III, IV Clinical Trials. *Cancers* 13, 1795 (2021).

133. Oprita, A. *et al.* Updated Insights on EGFR Signaling Pathways in Glioma. *Int J Mol Sci* 22, 587 (2021).

9 Appendix

9.1 Plasmid Maps

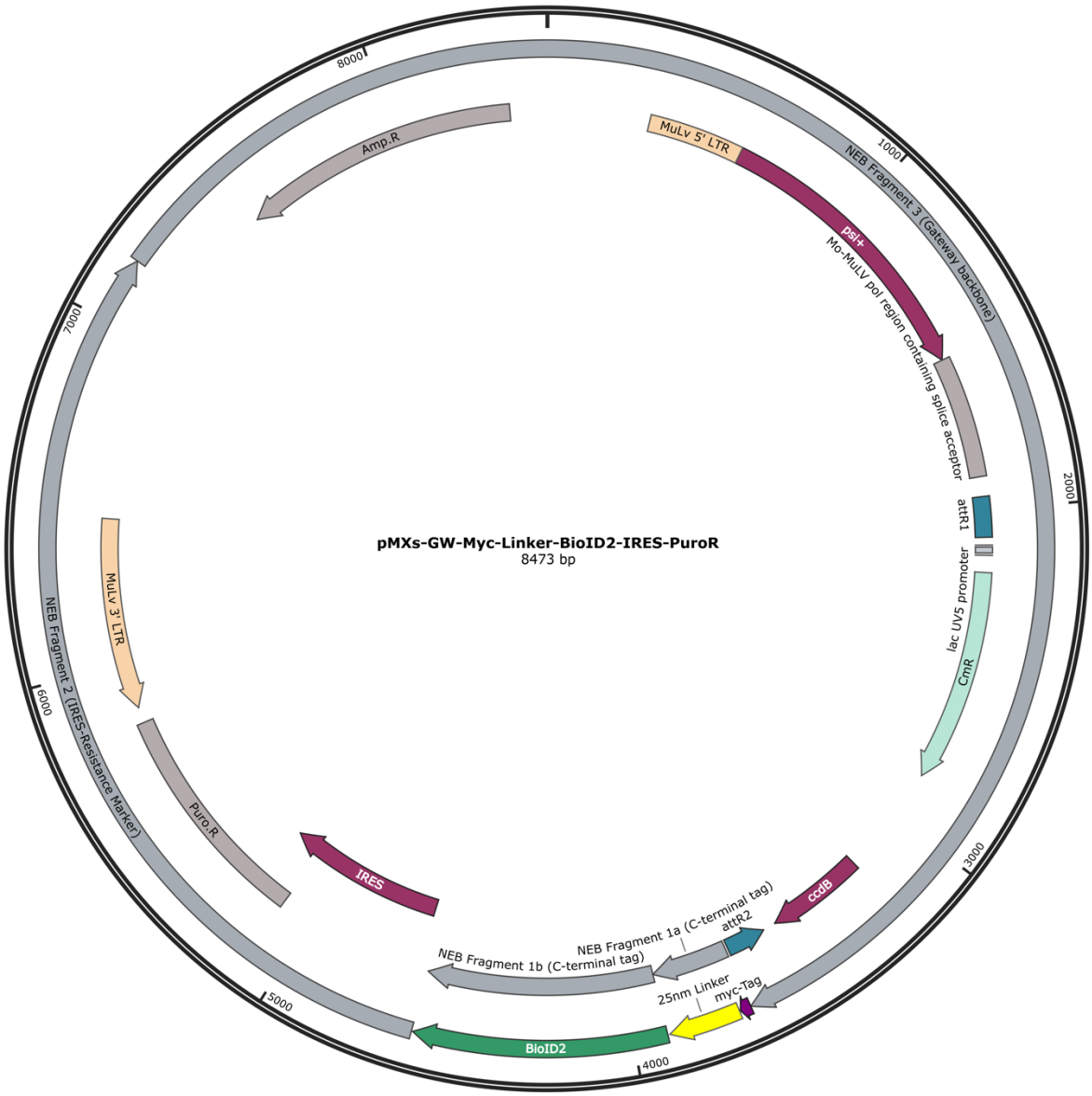

Supplementary Figure 1. Plasmid map of Gateway™-compatible pMXs-GW-Myc-Linker-BioID2-IRES-PuroR destination vector. DNA fragments used for DNA assembly (i.e., NEB Fragments 1a-3) are indicated. The BioID2 tag is located C-terminally to a Myc tag-Linker cassette that immediately follows the Gateway (GW) cassette. An IRES-PuroR cassette is located downstream of the BioID2 tag. Fusion protein expression is driven by the 5' murine leukemia virus (MuLv) long terminal repeat (LTR).

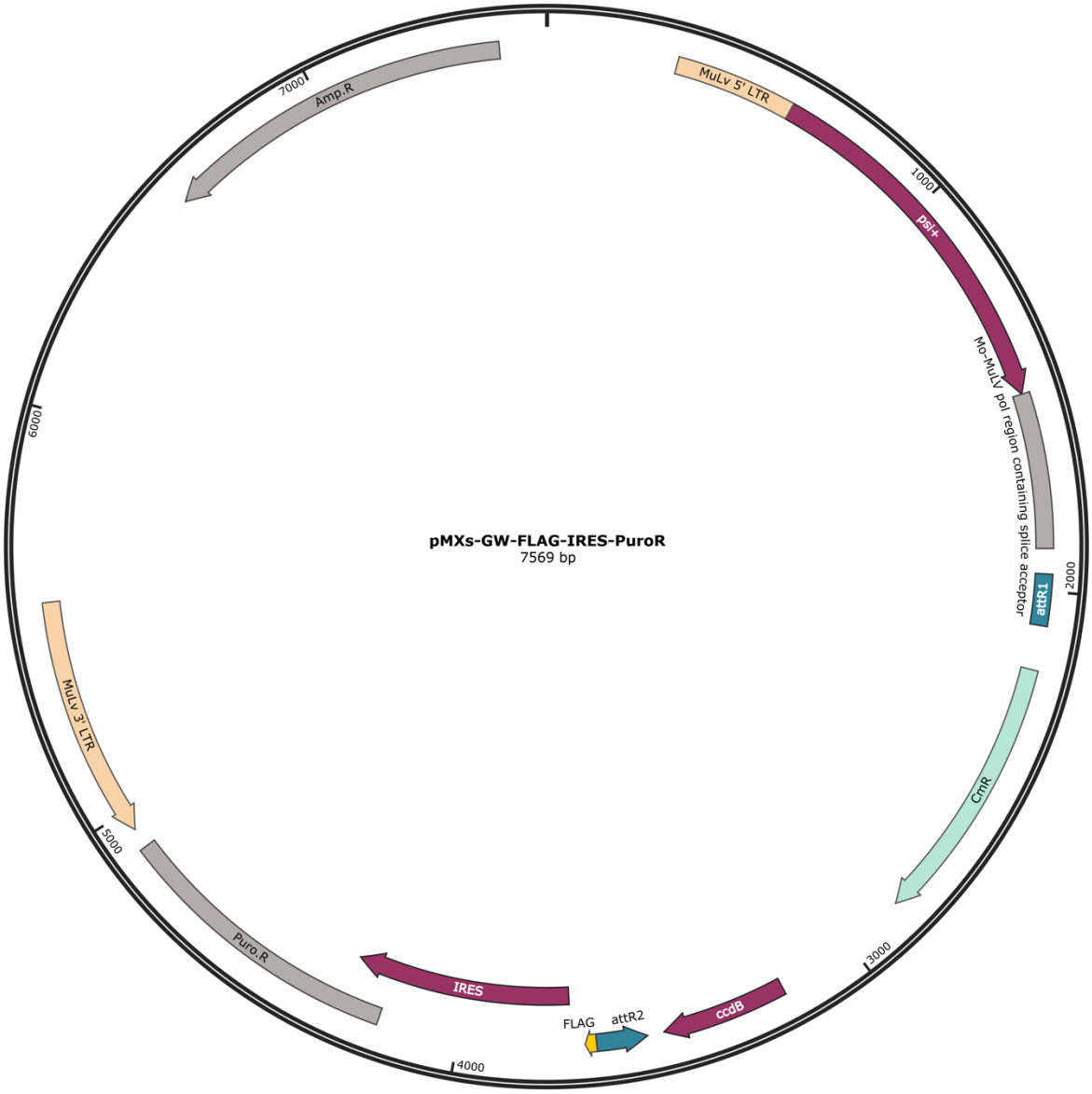

Supplementary Figure 2. Plasmid map of Gateway™-compatible pMXs-GW-FLAG-IRES-PuroR destination vector. The FLAG tag is located at the C-terminal end of the GW cassette. An IRES-PuroR cassette is located downstream of the FLAG tag. The PuroR cassette is alternatively replaced by a BsdR resistance marker when indicated. Fusion protein expression is driven by the 5' MuLv LTR.

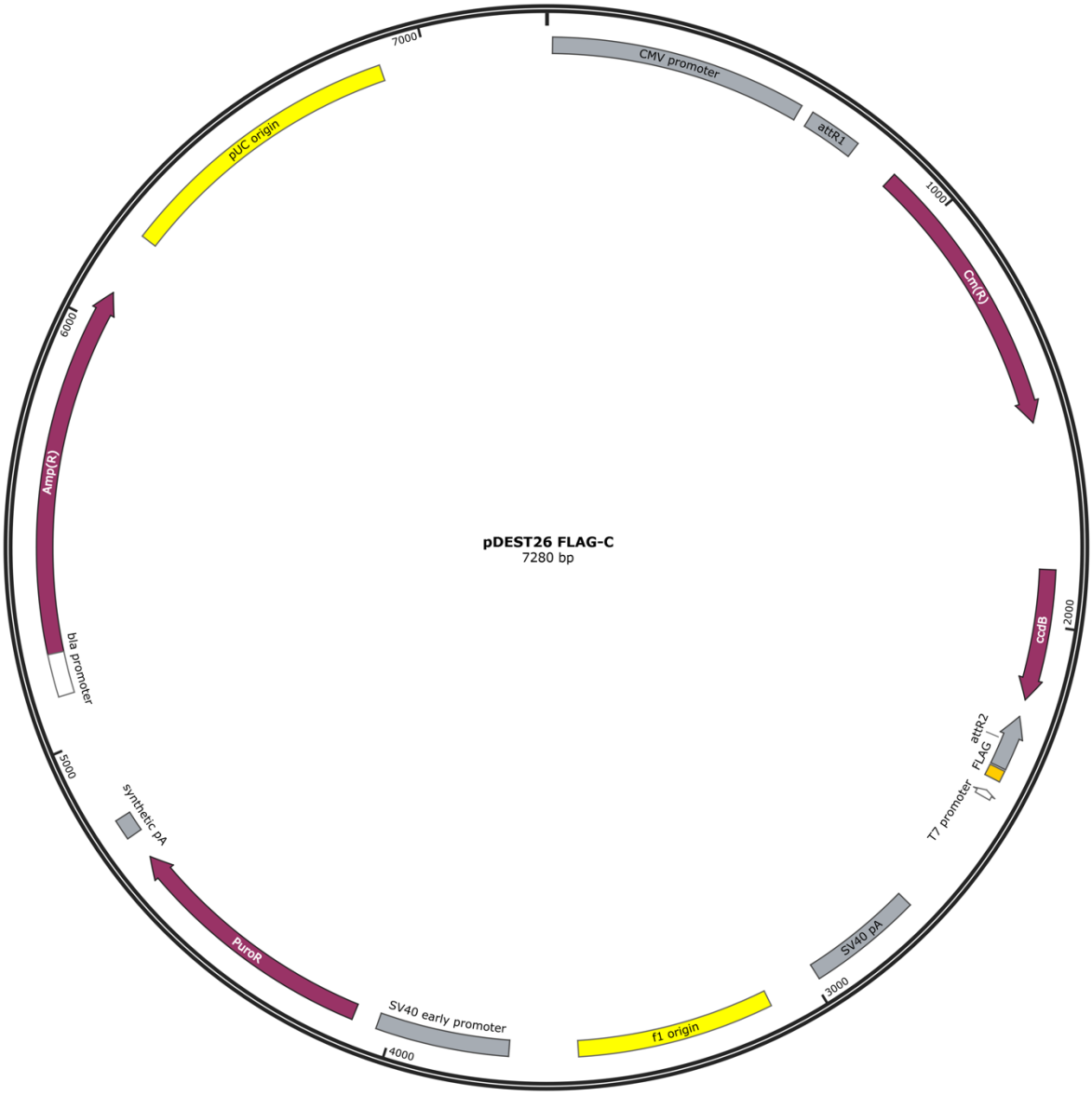

Supplementary Figure 3. Plasmid map of Gateway™-compatible pDEST26 FLAG-C destination vector. For AP-MS experiments, this vector backbone was used. The FLAG tag is again located at the C-terminal end of the GW cassette. Expression of FLAG-tagged proteins is driven by a cytomegalovirus (CMV) promoter instead of viral LTRs. A PuroR cassette driven separately by a simian virus 40 (SV40) promoter is located further downstream.

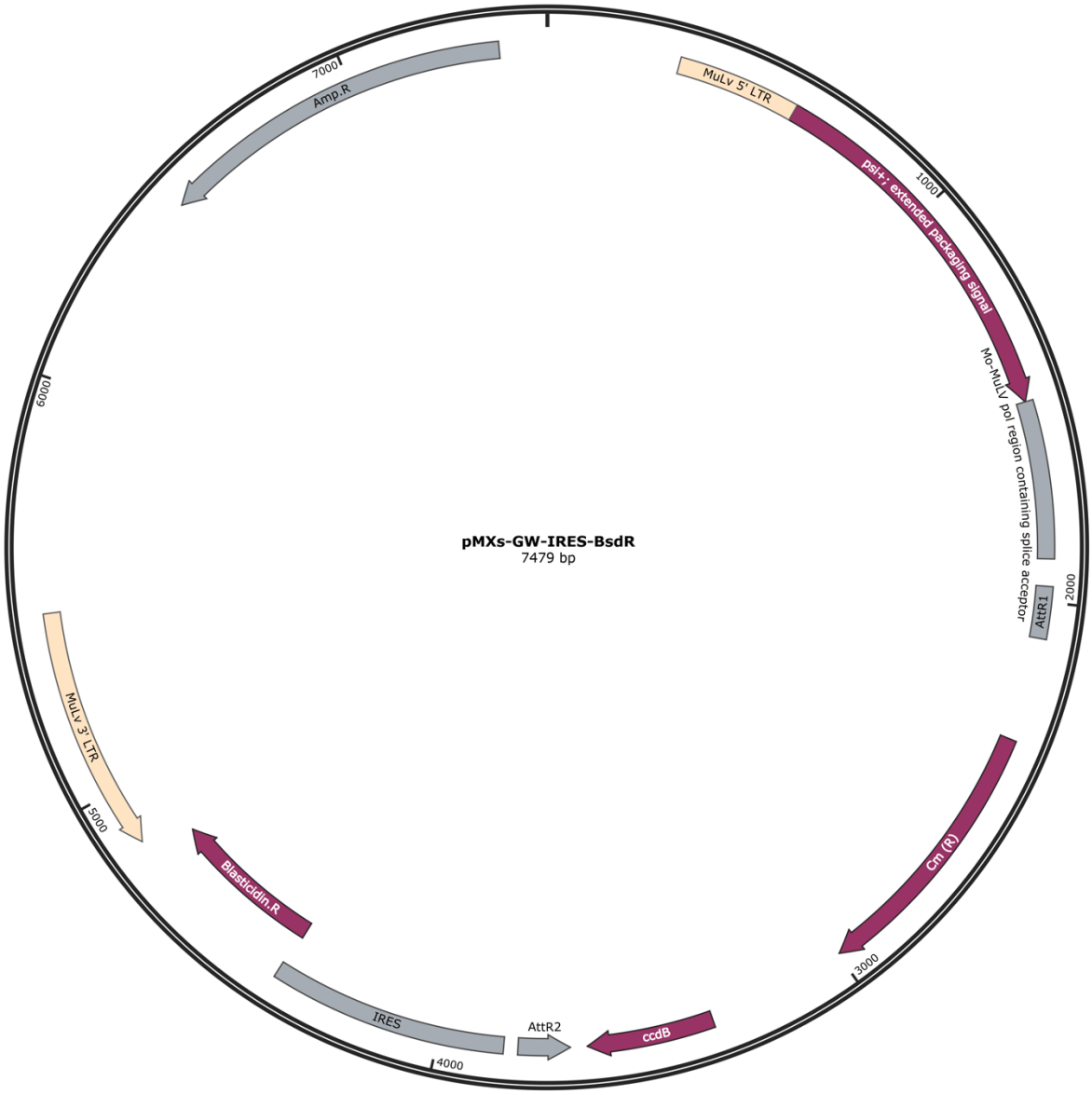

Supplementary Figure 4. Plasmid map of Gateway™-compatible pMXs-GW-IRES-BsdR destination vector. POI expression is driven by the 5' MuLv LTR. No tag is present in this vector. An IRES-BsdR cassette is located downstream of the GW cassette.

9.2 Sequencing Results

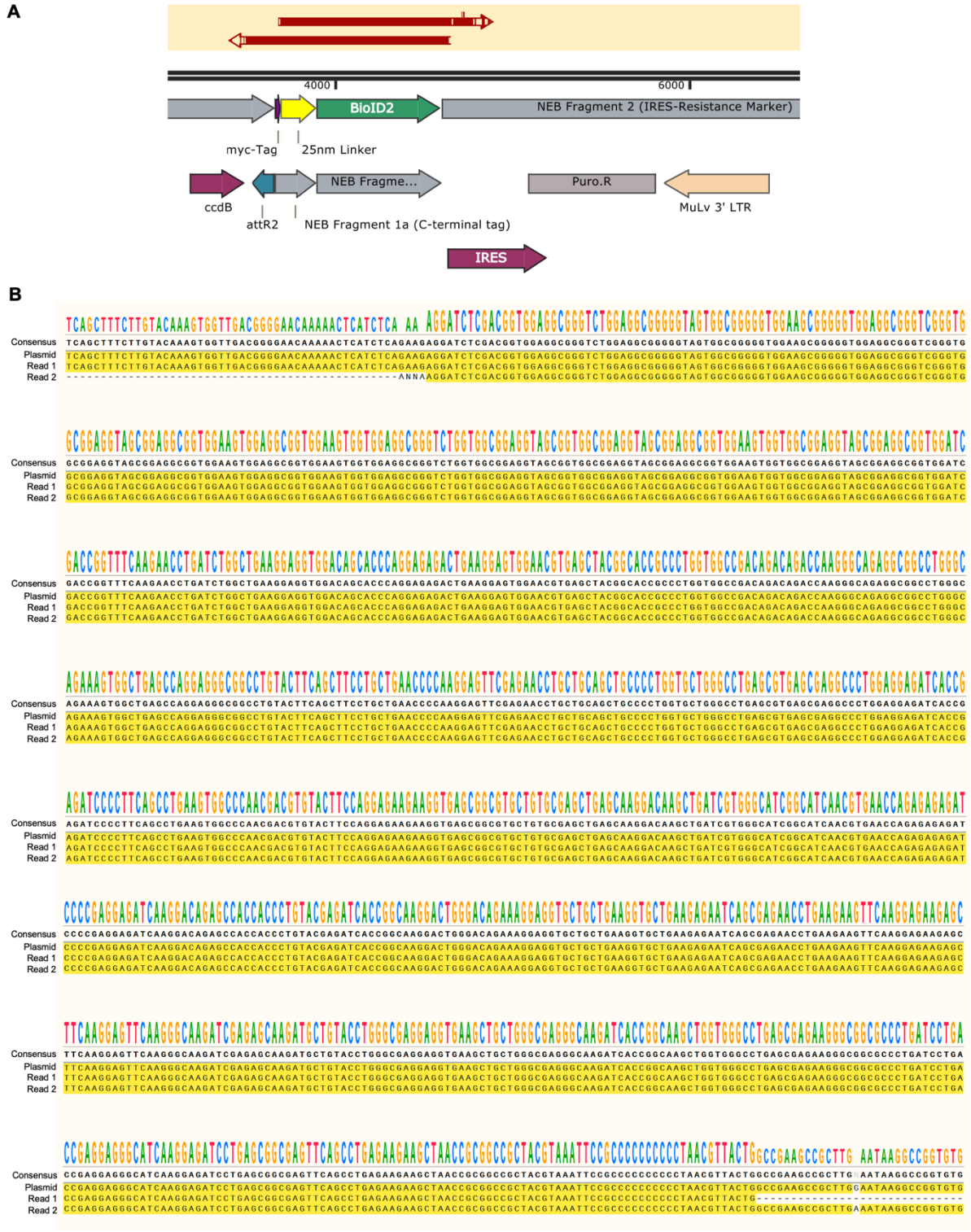

Supplementary Figure 5. Sequencing of pMXs-GW-Myc-Linker-BioID2-IRES-PuroR NEB assembly. A) Partial plasmid map showing the relative locations of the sequencing reads (red arrows). B) MUSCLE alignment of the partial plasmid sequence and the two sequencing reads.

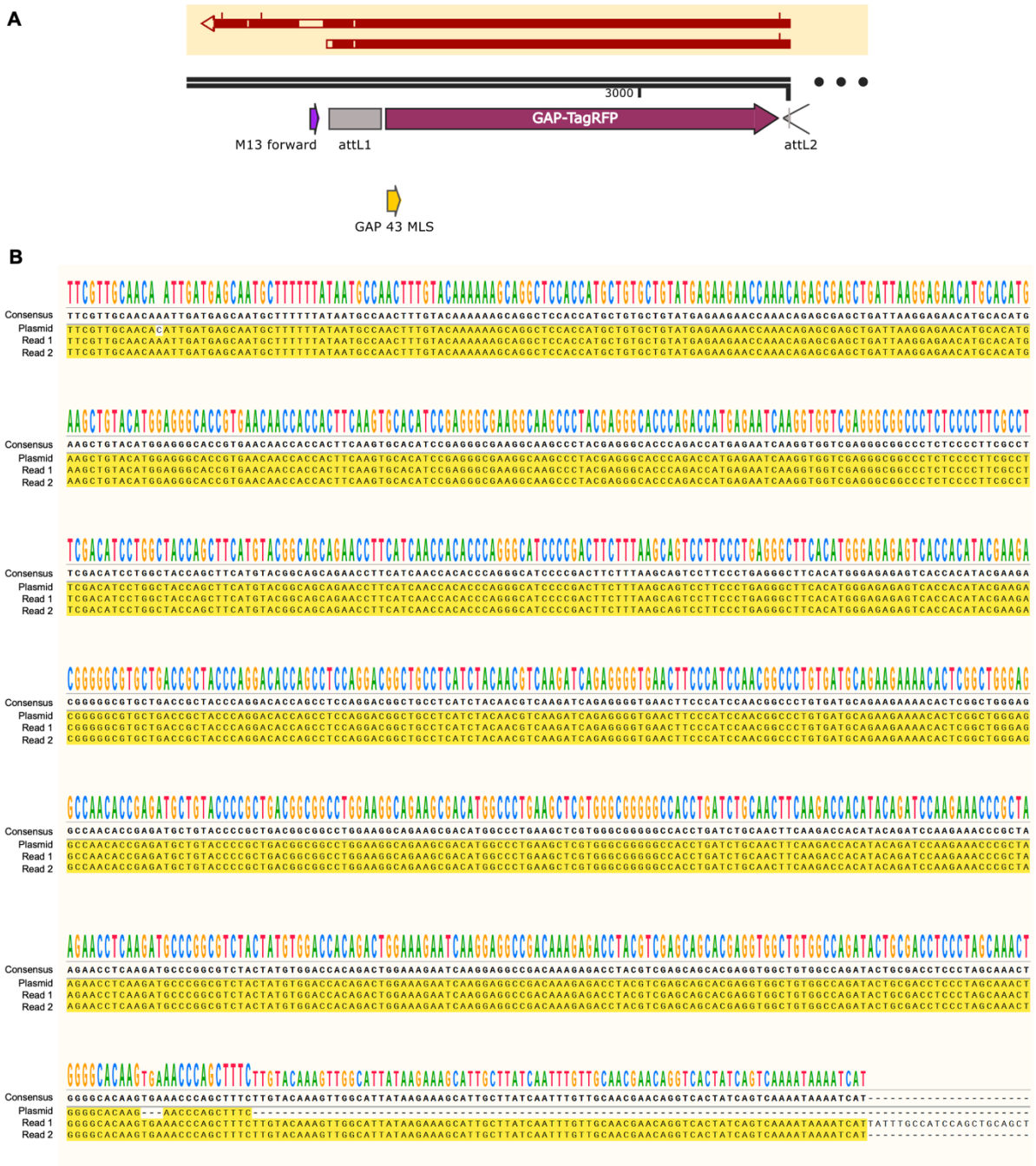

Supplementary Figure 6. Sequencing of GAP-TagRFP coding sequence after SDM-PCR of TagRFP in pDONR201. A) Partial plasmid map showing the relative locations of the sequencing reads (red arrows). B) MUSCLE alignment of the partial plasmid sequence and the two sequencing reads.

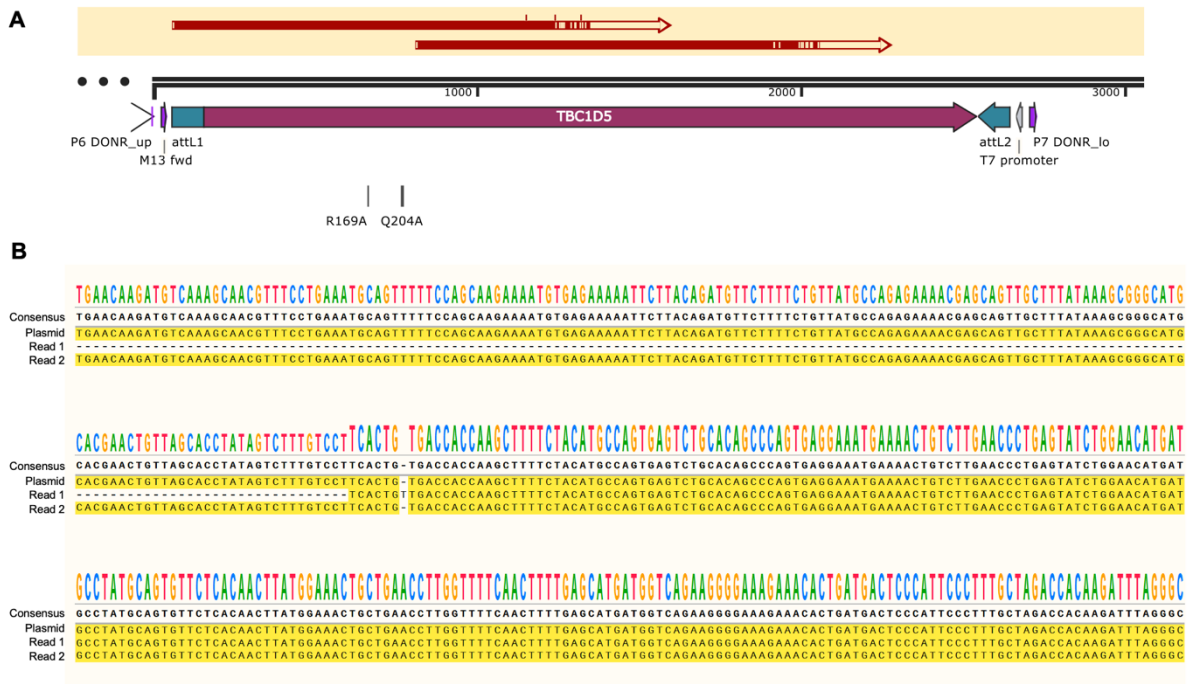

Supplementary Figure 7. Sequencing of the TBC1D5 R169A/Q204A coding sequence after SDM-PCR of TBC1D5 WT -STOP in pDONR223. A) Partial plasmid map showing the relative locations of the sequencing reads (red arrows). B) MUSCLE alignment of the partial plasmid sequence and the two sequencing reads.

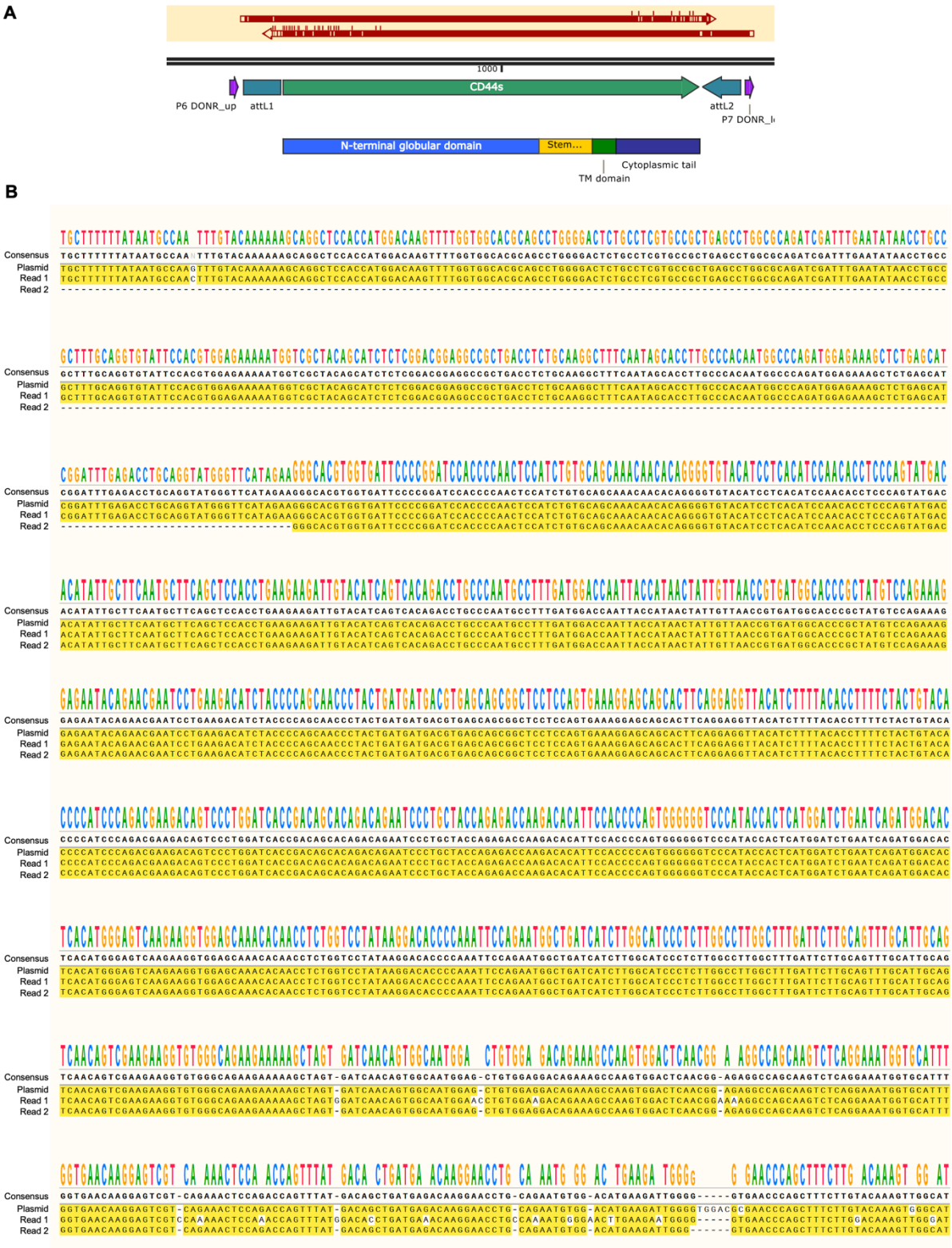

Supplementary Figure 8. Sequencing of the full-length CD44s coding sequence after BP cloning into pDONR201. A) Partial plasmid map showing the relative locations of the sequencing reads (red arrows). B) MUSCLE alignment of the partial plasmid sequence and the two sequencing reads.

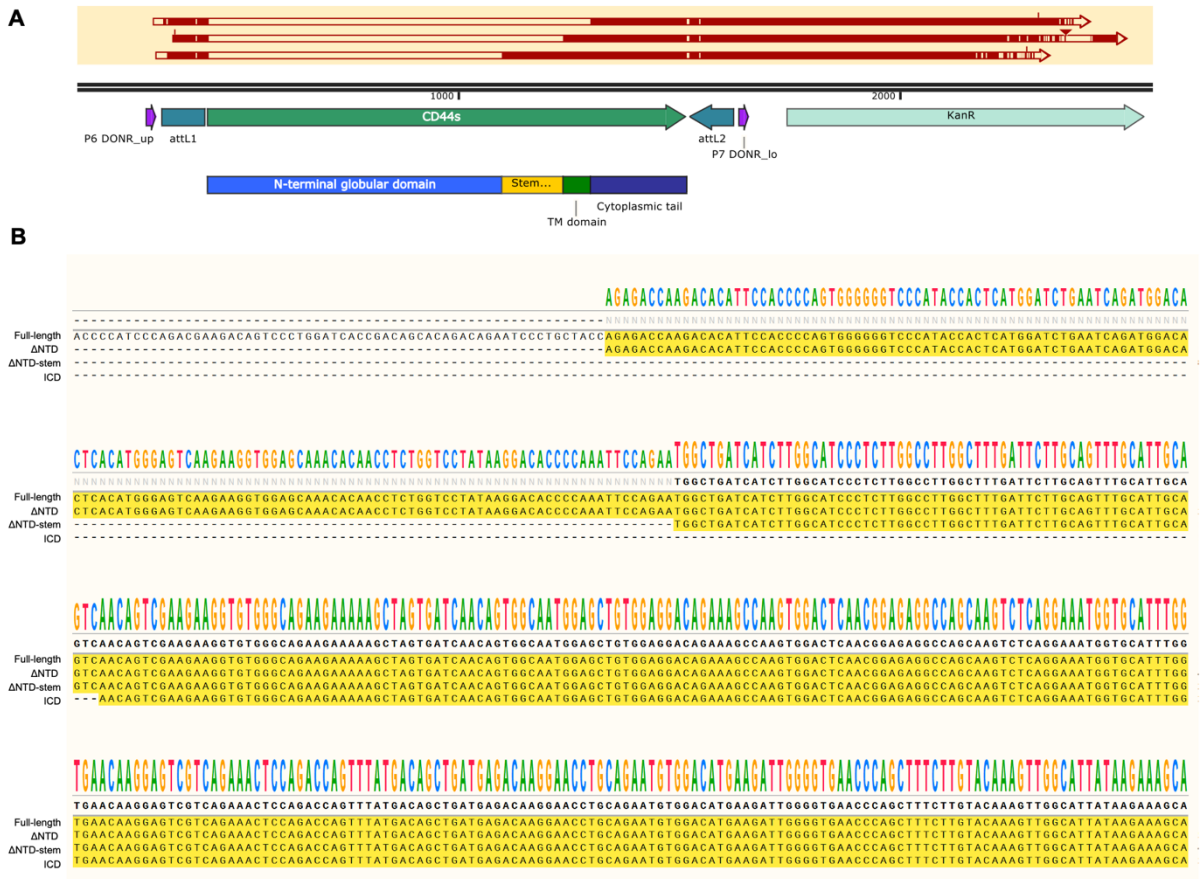

Supplementary Figure 9. Sequencing of the CD44s truncation mutants after BP cloning into pDONR201. A) Partial plasmid map showing the relative locations of the sequencing reads (red arrows). B) MUSCLE alignment of the partial plasmid sequence and the sequencing reads for each truncated mutant.

9.3 Validation of additional cellular models

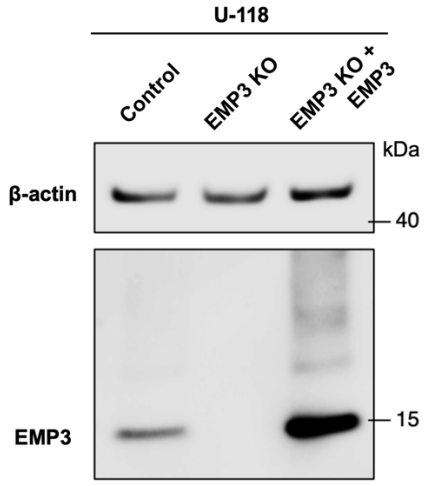

Supplementary Figure 10. Western blotting of EMP3 in U-118 control, EMP3 KO, and EMP3 KO rescue cells. To restore EMP3 expression, U-118 EMP3 KO cells were stably transfected with EMP3 in pMXs-GW-IRES-BsdR.

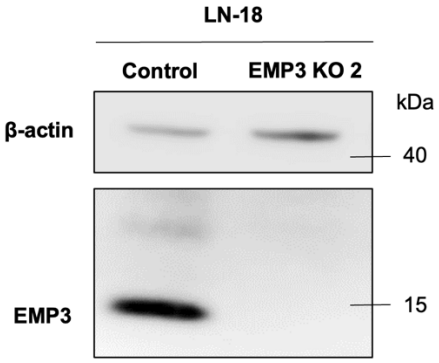

Supplementary Figure 11. Western blotting of EMP3 in LN-18 control and EMP3 KO cells targeted with an alternative guide RNA